



OIL & GAS

**THCM Coupled Model for Hydrate-Bearing Sediments: Data Analysis  
and Design of New Field Experiments  
(Marine and Permafrost Settings)**

**Final Scientific / Technical Report**

**Project / Reporting Period: October 1<sup>st</sup> 2013 to  
September 30<sup>th</sup> 2016**

**Date of Report Issuance: February 2017**

**DOE Award Number: DE-FE0013889**

**Principal Investigators / Submitting Organization**

<b>Marcelo Sánchez</b>	<b>and</b>	<b>J. Carlos Santamarina</b>
Texas A&M University		formerly at
DUNS #: 847205572		Georgia Institute of Technology
College Station, Texas		Atlanta, Georgia
979-862-6604		404-894-7605
<a href="mailto:msanchez@civil.tamu.edu">msanchez@civil.tamu.edu</a>		<a href="mailto:jcs@gatech.edu">jcs@gatech.edu</a>

Prepared for:

United States Department of Energy

National Energy Technology



U.S. DEPARTMENT OF  
**ENERGY**

**NATIONAL ENERGY  
TECHNOLOGY LABORATORY**

**Office of Fossil Energy**

DISCLAIMER: “This report was prepared as an account of work sponsored by an agency of the United States Government. Neither the United States Government nor any agency thereof, nor any of their employees, makes any warranty, express or implied, or assumes any legal liability or responsibility for the accuracy, completeness, or usefulness of any information, apparatus, product, or process disclosed, or represents that its use would not infringe privately owned rights. Reference herein to any specific commercial product, process, or service by trade name, trademark, manufacturer, or otherwise does not necessarily constitute or imply its endorsement, recommendation, or favoring by the United States Government or any agency thereof. The views and opinions of authors expressed herein do not necessarily state or reflect those of the United States Government or any agency thereof.”

# Table of Contents

<b>ABSTRACT .....</b>	<b>8</b>
<b>EXECUTIVE SUMMARY .....</b>	<b>9</b>
1. INTRODUCTION .....	11
2. THEORETICAL AND MATHEMATICAL FRAMEWORK .....	14
2.1. <i>Phases and Species – Mass densities</i> .....	14
2.2. <i>Volumetric Relations</i> .....	16
2.3. <i>Balance Equations</i> .....	16
2.4. <i>Constitutive Equations</i> .....	19
2.5. <i>Phase Boundaries - Reaction Kinetics</i> .....	21
2.6. <i>Computer code</i> .....	23
3. IT TOOL FOR HBS .....	24
4. GEOMECHANICAL MODELING.....	29
5. ANALYTICAL SOLUTIONS AND CODE VERIFICATION .....	57
6. NUMERICAL ANALYSIS – CODE VALIDATION.....	77
7. SUMMARY AND CONCLUSIONS.....	88
8. RELATED ACTIVITIES .....	91
9. REFERENCES .....	95

## Table of Figures

Figure 2-1 Hydrate bearing sediments: a) Grains, water, gas, hydrate and ice may be found forming the sediment. (b) Components can be grouped into phases and species .	14
Figure 2-2 Phase boundaries for water-gas mixtures in the pressure-temperature space. The phases in each quadrant depend on the availability of water and gas, and the PT trajectory. ....	22
Figure 3-1 Scheme showing the link between the proposed IT tool, the source of data (for <i>HBS</i> ) and the modeling. ....	25
Figure 3-2 Examples of data and formulations for mechanical properties: a) comparison of predicted strength by Santamarina and Ruppel (2008) and measured strength; and b) comparison of predicted strength by Miyazaki et al. (2012) and measured strength. ....	25
Figure 3-3 Phase boundaries: a) hydrate phase equilibrium in seawater; and b) freezing point of seawater .....	27
Figure 3-4 Mathcad based IT tool prototype. ....	27
Figure 3-5 Example of Mathcad based IT tool interfaces for parameter input/selection.	28
Figure 4-1 Main types of hydrate morphology: (a) cementation; (b) pore-filling; and (c) load-bearing. ....	30
Figure 4-2 Tests on natural and synthetic <i>HBS</i> in terms of stress-strain behavior and volumetric response a) specimens prepared at different hydrate saturation; and b) samples prepared with different hydrate morphology (Masui et al., 2005; 2008).....	31
Figure 4-3 a) Experimental results for drained triaxial tests involving hydrate dissociation (Hyodo, 2014); b) behavior of a natural <i>HBS</i> subjected to loading and dissociation under stress at oedometric conditions (Santamarina et al., 2015).....	33
Figure 4-4 a) Schematic representation of the hydrate damaged during shearing; b) rearrangement of the <i>HBS</i> structure upon dissociation.....	34
Figure 4-5 Schematic representation of a <i>HBS</i> . ....	35
Figure 4-6 Yield surfaces considered in the proposed model.....	40
Figure 4-7 Comparisons between model and experimental results for synthetic samples of <i>HBS</i> prepared at different hydrate saturations: a) stress-strain behavior; b) volumetric response. Experimental data adapted from (Hyodo, 2013).....	44
Figure 4-8 Comparisons between model and experimental results for synthetic Toyoura sand samples with different hydrates pore habits: a) stress strain behavior; b) volumetric response. Experimental data adapted from (Masui, 2005) .....	45
Figure 4-9 Model and experimental results for triaxial tests on natural samples: a) stress strain behavior; b) volumetric response. Experimental data adapted from (Yoneda et al. 2015) .....	47

Figure 4-10 Experimental and modeling results for drained triaxial tests: a) already dissociated sediment, b) dissociation induced at $\varepsilon_a=1\%$ ; and c) dissociation induced at $\varepsilon_a=5\%$ . Experimental data adapted from (Hyodo, 2014).....	49
Figure 4-11 Additional modeling information for the test in which dissociation was induced at $\varepsilon_a=5\%$ : a) extended stress-strain behavior; b) hardening variables, c) yield surfaces at the beginning of the experiment; and d) yield surfaces at an intermediate stage of shearing ( $\varepsilon_a=15.3\%$ ) and at the end of test.....	50
Figure 4-12 Effect of confinement on HBS: a) stress strain behavior; b) volumetric response.....	52
Figure 4-13 Additional modeling information for the test in Fig 4.13 at $\sigma'_c=1$ MPa: a) stress-strain behavior; b) hardening variables; c) yield surfaces at two initial stages of the experiment A&B; and c) yield surfaces at two final stages of shearing C&D. ....	53
Figure 4-14 Effect of $\chi_0$ on HBS: a) stress-strain behavior, b) volumetric response.....	54
Figure 4-15 Behavior during dissociation of natural <i>HBS</i> specimens under oedometric conditions: a) core 8P; and b) core 10P. Experimental data adapted from (Santamarina et al. 2015) .....	55
Figure 4-16 Additional modeling information for the test related to core 10P: a) vertical stresses computed by the model during loading; b) hardening variables. ....	56
Figure 5-1 Estimation of global gas on the state of hydrate gas. From Sloan and Koh (2007); Boswell and Collett (2011). Notice conventional gas reserves are still orders of magnitude less than the worst of hydrate gas estimations. ....	57
Figure 5-2 Two zones can be identified under steady state conditions when the pressure drop is kept constant and hydrate stops dissociating: an inner zone where hydrate has been depleted and an outer zone where hydrate remains stable. ....	64
Figure 5-3 General description for a half depth of reservoir confined by less permeable layers. If $k' \ll k$ then horizontal streamlines within reservoir and vertical ascended/descended flow lines into reservoir from less permeable confining layers can be assumed.....	66
Figure 5-4 Axisymmetric <i>HBS</i> reservoir confined between less permeable layers. At steady state condition, reservoir is divided in two zones of free hydrate sediments and <i>HBS</i> by an interface radius know as dissociation front ( $r^*$ ). The homogenous porous medium through the reservoir is assumed; therefore $k_{sed}=k_{HBS}=k$ and consequently $n=1$ . ....	67
Figure 5-5 Axisymmetric <i>HBS</i> reservoir confined between impermeable layer from one side and less permeable layer from another side. The homogenous porous medium through the reservoir is assumed; therefore $k_{sed}=k_{HBS}=k$ and consequently $n=1$ . ....	68
Figure 5-6 Results obtained with the analytical solution for the case of reservoir confined between two impermeable layers and numerical models for the different cases listed in Table 5.5. ....	70

Figure 5-7 Economical analysis. Profit per hydrate thickness with respect to dissociation front for selected potential locations.....	71
Figure 5-8 Dissociation front computed tends to be larger than the values from the literature but contained in a 15% error area. Note that Mt. Elbert simulations were stopped after 10800 days of production (i.e. no ultimate radius of dissociation was reached).....	72
Figure 5-9 Example of gas hydrate production from a marine environment under depressurization strategy (Summary of parameters used can be found in Table 5.8). ....	76
Figure 6-1 Test instrumentation, sample 21C-02E (modified after Yun et al., 2010).....	77
Figure 6-2 Path in the P-T plane followed during of a pressure core gathered from the Krishna-Godavari Basin (reported by Yun et al., 2009).....	78
Figure 6-3 Evolution of the main variables recorded during the experiment: a) time evolution of pressure and gas production; and b) gas production versus fluid pressure (data gathered from the Krishna-Godavari Basin, Yun et al., 2009). ....	78
Figure 6-4 Results of hydrate formation by heating a) Schematic of P-T path b) P-T path plotted in the P-T plane c) Gas produced d) Phase saturation of hydrates, water (liquid), gas and ice.....	79
Figure 6-5 Problems Schematic .....	80
Figure 6-6 Temperature comparisons .....	81
Figure 6-7 Gas pressure comparisons .....	82
Figure 6-8 Water saturation comparisons .....	83
Figure 6-9 Schematic representation as reported in Benchmark #2 .....	84
Figure 6-10 Simulators results comparisons in terms of temperature .....	85
Figure 6-11 Simulators results comparisons in terms of gas pressure.....	86
Figure 6-12 Simulators results comparisons in terms of $S_H$ .....	87

## List of Tables

Table 2-1: Specific Energy and Thermal Transport – Selected Representative Values ..	15
Table 3-1: List of Properties .....	25
Table 3-2: Mechanical properties .....	26
Table 3-3: Phase properties .....	26
Table 4-1: Test conditions for triaxial compression tests studied in Case1 .....	43
Table 4-2: Soil parameters adopted in the modeling of HBS in Case1 .....	43
Table 4-3: Soil parameters adopted in the modeling of Cases in Case2.....	45
Table 4-4: In situ conditions, soil properties, and testing conditions for tests presented in Case3.....	46
Table 4-5: Soil parameters adopted in the modeling of <i>HBS</i> specimens in Case3 .....	46
Table 4-6: Test conditions of methane hydrate dissociation tests. Case4.....	47
Table 4-7: Parameters adopted in the modeling of HBS specimens. Case4.....	48
Table 4-8: Parameters adopted in Case4 - Effect of confining pressure.....	51
Table 4-9: Parameters adopted in Section 4.5. Effect of parameters*: $\chi_0$ .....	53
Table 4-10: Parameters adopted in the modeling of HBS specimens in Section 4.6.....	54
Table 5-1: Selected reservoirs gas volume estimation.....	58
Table 5-2: Well tests summary in chronological order.....	59
Table 5-3: Summary of selected parameters used in numerical simulations.....	60
Table 5-4: Cases considered in the analysis .....	69
Table 5-5: Model parameters used in numerical simulation.....	69
Table 5-6: Profit analysis .....	72
Table 5-7: Data input for equations for selected cases .....	73
Table 5-8: Summary of parameters for the example in Figure 5.9.....	75

## Table of Acronyms and Abbreviations

BSR	:	Bottom Simulating Reflector
FE	:	Finite Element
FERC	:	Federal Energy Regulatory Commission
HBS	:	Hydrate Bearing Sediments
HISS	:	Hierarchical Single Surface
IPTC	:	Instrumental Pressure Testing Chamber
MC	:	Mohr Coulomb
MCC	:	Modified Cam Clay
NGHP	:	National Gas Hydrate Program
PT	:	Pressure Temperature
PCCT	:	Pressure Core Characterization Test
RE	:	Recoverable Energy
STP	:	Standard Temperature and Pressure
THCM	:	Thermo Hydro Chemo Mechanical

## **ABSTRACT**

Stability conditions constrain the occurrence of gas hydrates to submarine sediments and permafrost regions. The amount of technically recoverable methane trapped in gas hydrate may exceed 104tcf. Gas hydrates are a potential energy resource, can contribute to climate change, and can cause large-scale seafloor instabilities. In addition, hydrate formation can be used for CO<sub>2</sub> sequestration (also through CO<sub>2</sub>-CH<sub>4</sub> replacement), and efficient geological storage seals. The experimental study of hydrate bearing sediments has been hindered by the very low solubility of methane in water (lab testing), and inherent sampling difficulties associated with depressurization and thermal changes during core extraction. This situation has prompted more decisive developments in numerical modeling in order to advance the current understanding of hydrate bearing sediments, and to investigate/optimize production strategies and implications. The goals of this research has been to addresses the complex thermo-hydro-chemo-mechanical THCM coupled phenomena in hydrate-bearing sediments, using a truly coupled numerical model that incorporates sound and proven constitutive relations, satisfies fundamental conservation principles. Analytical solutions aimed at verifying the proposed code have been proposed as well. These tools will allow to better analyze available data and to further enhance the current understanding of hydrate bearing sediments in view of future field experiments and the development of production technology.

## EXECUTIVE SUMMARY

Gas hydrates are solid compounds made of water molecules clustered around low molecular weight gas molecules such as methane, hydrogen, and carbon dioxide. Methane hydrates form under pressure ( $P$ ) and temperature ( $T$ ) conditions that are common in sub-permafrost layers and in deep marine sediments. Hydrate concentration is gas-limited in most cases, except near high gas-flux conduits. Stability conditions constrain the occurrence of gas hydrates to submarine sediments and permafrost regions. The amount of technically recoverable methane trapped in gas hydrate may exceed 104tcf. Gas hydrates are a potential energy resource, can contribute to climate change, and can cause large-scale seafloor instabilities. In addition, hydrate formation can be used for CO<sub>2</sub> sequestration (also through CO<sub>2</sub>-CH<sub>4</sub> replacement), and efficient geological storage seals. The experimental study of hydrate bearing sediments has been hindered by the very low solubility of methane in water (lab testing), and inherent sampling difficulties associated with depressurization and thermal changes during core extraction. This situation has prompted more decisive developments in numerical modeling in order to advance the current understanding of hydrate bearing sediments, and to investigate/optimize production strategies and implications.

The goals of this research has been to addresses the complex thermo-hydro-chemo-mechanical THCM coupled phenomena in hydrate-bearing sediments, using a truly coupled numerical model that incorporates sound and proven constitutive relations, satisfies fundamental conservation principles. Analytical solutions aimed at verifying the proposed code have been proposed as well. These tools will allow to better analyze available data and to further enhance the current understanding of hydrate bearing sediments in view of future field experiments and the development of production technology. A selection of important research outcomes follows:

- THCM-hydrate: a robust fully coupled and efficient formulation for HBS incorporating the fundamental physical and chemical phenomena that control de behavior of gas hydrates bearing sediments has been developed and validated.
- THCM-hydrate: properly captures the complex interaction between water and gas, and kinetic differences between ice and hydrate formation. Therefore, it permits exploring the development of phases along the various  $P$ - $T$  trajectories that may take place in field situations.
- Results show the pronounced effect of hydrate dissociation on pore fluid pressure generation, and the consequences on effective stress and sediment response. Conversely, the model shows that changes in effective stress can cause hydrate instability.
- The proposed new geomechanical model was capable of capturing not only the main trends and features of sediment observed in the different tests, but also to reproduce very closely the experimental observations in most of the analyzed cases.
- The enhancement of sediment strength, stiffenss and dilation induced by the presence of the hydrates were well reproduced by the model.

- The ability of the proposed mechanical model to simulate the volumetric soil collapse compression observed during hydrate dissociation at constant stresses is particularly remarkable. This is a key contribution of this research in relation to the geomechanical modeling of HBS during dissociation.
- The mechanical model has also assisted to interpret how sediment and hydrates contribute to the mechanical behavior of HBS and how these contributions evolve during loading and hydrates dissociation.
- The analytical solutions show the interplay between the variables: relative sediment permeabilities  $k_{sed}/k_{hbs}$ , the leakage in the aquifer  $k'/k_{sed}$ , relative pressure dissociation  $(h^* - h_w)/(h_{far} - h^*)$  and a geometrical ratio  $H b/r_w^2$ .
- At steady-state conditions, the pressure distribution in radial flow is inversely proportional to the logarithm of the radial distance to the well. Therefore there is a physical limit to the zone around a well that can experience pressure-driven dissociation.
- The results reflect the complexity of gas recovery from deep sediments included limited affected zone, large changes in effective stress and associated reductions in permeability.
- THCM-hydrate simulation results compare favorably with published results with well-defined boundary conditions; this corroborates the validity of the implementation.
- THCM-hydrate relevance: resource recovery, environmental implications, seafloor instability

## 1. INTRODUCTION

Gas hydrates are solid compounds made of water molecules clustered around low molecular weight gas molecules such as methane, hydrogen, and carbon dioxide. Methane hydrates form under pressure ( $P$ ) and temperature ( $T$ ) conditions that are common in sub-permafrost layers and in deep marine sediments, and their distribution is typically correlated with the presence of oil reservoirs and thermogenic gas. Hydrate concentration is gas-limited in most cases, except near high gas-flux conduits.

Hydrate bearing sediments (*HBS*) play a critical role on the evolution of various natural processes and the performance of engineered systems. Hydrate dissociation can cause borehole instability, blowouts, foundation failures, and trigger large-scale submarine slope failures (Kayen & Lee, 1991; Jamaluddin et al., 1991; Briaud and Chaouch, 1997; Chatti et al., 2005). The escape of methane into the atmosphere would exacerbate greenhouse effects and contribute to global warming (Dickens et al., 1997). Methane hydrates can become a valuable energy resource as large reserves are expected worldwide (e.g. Sloan, 1998; Soga et al., 2006; Rutqvist and Moridis, 2007). Furthermore, carbon sequestration in the form of  $\text{CO}_2$  hydrate is an attractive alternative to reduce the concentration of  $\text{CO}_2$  in the atmosphere.

The experimental study of hydrate bearing sediments has been hindered by the very low solubility of methane in water (lab testing), and inherent sampling difficulties associated with depressurization and thermal changes during core extraction. This situation has prompted more decisive developments in numerical modeling in order to advance the current understanding of hydrate bearing sediments, and to investigate/optimize production strategies and implications.

Numerical modeling is equally challenged by the complex behavior of hydrate bearing sediments. Hydrate dissociation (triggered by either increase in temperature, decrease in fluid pressure or changes in pore fluid chemistry) is accompanied by large volume expansion, for example, a 2.6-to-1 volume expansion takes place during methane hydrate dissociation at a constant pressure of  $P=10$  MPa. Such a pronounced expansion of the pore fluid within sediments will cause either large fluid flux in free draining conditions, or high fluid pressure if the rate of dissociation is faster than the rate of fluid pressure dissipation (possibly causing fluid-driven fractures, Shin and Santamarina 2010). In general, the excess pore fluid pressure will depend on the initial volume fraction of the phases, the rate of dissociation (often controlled by the rate of heat transport) relative to the rate of mass transport, and sediment compliance. In turn, changes in fluid pressure will alter the effective stress, hence the stiffness, strength and dilatancy of the sediment. Therefore, hydrates stability conditions combine with sediment behavior to produce a strong Thermo-Hydro-Chemo-Mechanical THCM coupled response in hydrate bearing sediments.

Methane production from gas hydrate accumulations in permafrost possess additional challenges and opportunities. Complex stress paths in the  $P$ - $T$  space with two phase boundaries (i.e. ice-liquid and gas-hydrate phase lines) are anticipated during gas production, including secondary ice and hydrate formation; clearly ice phase must be explicitly incorporated in the analysis as it affects mechanical stability, fluid migration, and thermal properties.

Truly coupled thermo-hydro-chemo-mechanical numerical approaches rather than sequential explicit computational schemes (i.e., they resolve the hydrate state separate from the sediment state at every time step) is recommendable for the robust analysis of hydrate bearing sediments. Sequential schemes often restrict computations to one-way coupled analysis where one can investigate, for example, the effects that changes in pressure and temperature have on the sediment mechanical response but does not account for the effect of granular strains on multiphase flow behavior. Furthermore, sequential schemes are generally less efficient because they require the use mapping algorithms to transfer the information between the codes used to solve the different physics. The robust monolithic approach in implicit truly-coupled methods leads to computational efficiency and improved rate of convergence in the solution of the coupled nonlinear problem.

Geomechanics is a key component in the numerical modeling of engineering problems involving *HBS*. Several types of mechanical constitutive models for hydrate bearing sediment have been proposed in the last few years. For example, Miyazaki et al. (2012) suggested a nonlinear elastic model for hydrate bearing sands based on the Duncan-Chang model (Duncan et al., 1970). The extension of the Mohr–Coulomb (MC) model to deal with hydrates is generally carried out by incorporating a dependency of the cohesion with the hydrate concentration (Klar et al., 2010; Rutqvist et al., 2007; Pinkert et al., 2014). As it is well-known, MC type models cannot capture plastic deformations before failure and are unable to simulate positive (compressive) plastic deformations. A model based on the Modified Cam-Clay (MCC) framework was proposed by Sultan and Garziglia (2011). Uchida et al. (2012; 2016) proposed a model based on the MCC and its validation was performed using published experiments conducted at constant hydrate saturation. Jeen-Shang et al. (2015) developed a critical state model based on the ‘spatial mobilized plane’ framework and sub-loading concepts. The discrete element method has also been used to simulate the mechanical behavior of *HBS* (e.g. Jiang et al., 2014; Jiang et al., 2015; Liu et al., 2014; Shen et al., 2016a; Shen and Jiang, 2016; Shen et al., 2016b; Yu et al., 2016). Section 4 provides more details about previous geomechanical modeling efforts. All the mechanical models discussed above have been used to simulate tests performed at constant hydrate saturation.

The geomechanical modeling of *HBS* has been a critical component of this research. An advanced new elasto-plastic model based on the stress partition concept (Carol et al., 2001; Fernandez et al., 2001; Pinyol et al., 2007; Vaunat et al., 2003) and the Hierarchical Single Surface (HISS) framework (Desai et al., 1986; 1989; 2000) was selected to provide a general and adaptable geomechanical model for hydrate bearing sediments. Recently published experimental data based on synthetic and natural specimens involving different  $S_h$  and hydrates morphology was adopted to validate the proposed approach. The model application and validation do not limit to cases in which  $S_h$  is maintained constant during the tests (as in previous works), but also include experiments in which dissociation is induced under constant stress. Particular attention is paid to evaluate the behavior of *HBS* during dissociation under different stress levels and tests conditions (i.e., triaxial and oedometric), as well as experiments involving both: reconstituted and natural specimens. The model also allows examining the individual contribution of sediments and hydrates to the mechanical behavior during loading and dissociation, aspect that was not studied before with an elastoplastic model for *HBS*.

The scope of the conducted study has been related to the development of a formal and robust numerical framework able to capture  $P&T$  paths and ensuing phase changes during production in either marine and permafrost settings analysis of available data from laboratory tests and field experiments. A geomechanical model and analytical solutions have been also proposed. The main following activities have been conducted:

- in-depth review of the properties associated with gas hydrates sediments, with proper recognition of hydrate morphology in different sediments;
- update of a thermo-hydro-chemo-mechanical THCM-hydrate formulation and code for hydrate bearing sediments to incorporate augmented constitutive models;
- development of bounding close-form analytical solutions that highlight the interplay between governing parameters in the context of gas production, and to corroborate the numerical code with these close-form end-member situations (i.e., close form solutions will inherently involve simplifying assumptions such as adiabatic, isochoric, isothermal, no mass transport, etc.);
- proposal of an advanced geomechanical model able to simulate the HBS during loading and dissociation;
- to use the enhanced code (in combination with close-form solutions) to optimize future field production studies in marine and permafrost sediments, taking into consideration various production strategies and addressing the most pertinent questions that have emerged from past field experiences

In the following sections a brief description of the main components of the conducted research is summarized.

## 2. THEORETICAL AND MATHEMATICAL FRAMEWORK

The dominant THCM phenomena that take place in hydrate-bearing sediments include:

- heat transport through conduction, liquid and gas phase advection,
- heat of formation-dissociation,
- water flux as liquid phase,
- methane flux in gas phase and as dissolved methane diffusion in liquid phase,
- heat of ice formation/thaw,
- fluid transport of chemical species,
- mechanical behavior: effective stress and hydrate-concentration dependent sediment behavior.

To include these main processes (as well as other interacting ones) balance equations, constitutive equations, equilibrium restrictions, and kinetic reactions are considered in the mathematical formulation. This set of coupled phenomena is analyzed next, following the CODE\_BRIGHT framework and numerical platform developed by Olivella et al. (1994).

### 2.1. Phases and Species – Mass densities

*HBS* consist of a granular skeleton where pores are filled with gas, hydrate, water or ice (Figure 2.1a). Three main species mineral, water, and methane are found in five phases: solid mineral particles, liquid, gas, hydrates and ice are considered. To simulate production strategies based on chemical stimulation, the presence of solutes in the liquid phase is also included. The ice phase is modeled because water-to-ice transformation may take place during fast depressurization. Observations related to phase composition and mass densities are discussed next. Figure 2.1b summarizes phases and their compositions; their mass densities are listed in Table 2.1.

*Solid and Ice.* These two phases are considered single species the solid phase is made of the mineral that forms the grains, and ice is made of pure water.

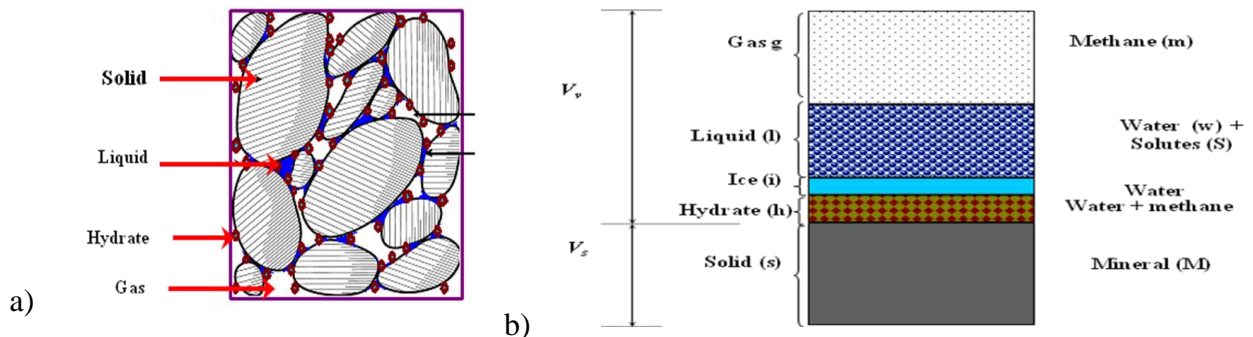


**Figure 2-1** Hydrate bearing sediments: a) Grains, water, gas, hydrate and ice may be found forming the sediment. (b) Components can be grouped into phases and species

**Table 2-1: Specific Energy and Thermal Transport – Selected Representative Values**

Species and Phases	Specific Energy		Transport
	Expression	specific heat - latent heat	thermal conduct.
<i>water - vapour</i>	$e_g^w = L_{evap} + c_{wv} (T - T_o)$	$L_{evap} = 2257 \text{ J.g}^{-1}$ $c_{wv} = 2.1 \text{ J.g}^{-1}\text{K}^{-1}$	$0.01 \text{ W m}^{-1}\text{K}^{-1}$
<i>water - liquid</i>	$e_w = c_{wl} (T - T_o)$	$c_{wl} = 4.2 \text{ J.g}^{-1}\text{K}^{-1}$	$0.58 \text{ W m}^{-1}\text{K}^{-1}$
<i>water - ice</i>	$e_{ice} = L_{fuse} + c_{wice} (T - T_o)$	$L_{fuse} = 334 \text{ J.g}^{-1}$ $c_{wice} = 2.1 \text{ J.g}^{-1}\text{K}^{-1}$	$2.1 \text{ W m}^{-1}\text{K}^{-1}$
<i>methane gas</i>	$e_m = c_m (T - T_o)$	$c_m = 1.9 \text{ J.g}^{-1}\text{K}^{-1}$ V=const $c_m = 2.5 \text{ J.g}^{-1}\text{K}^{-1}$ P=const	$0.01 \text{ W m}^{-1}\text{K}^{-1}$
<i>hydrate</i> <sup>(1)</sup>	$e_h = L_{diss} + c_h (T - T_o)$	$L_{diss} = 339 \text{ J.g}^{-1}$ $c_h = 2.1 \text{ J.g}^{-1}\text{K}^{-1}$	$0.5 \text{ W m}^{-1}\text{K}^{-1}$
<i>mineral</i>	$e_s = c_s (T - T_o)$	$c_s = 0.7 \text{ J.g}^{-1}\text{K}^{-1}$ quartz $c_s = 0.8 \text{ J.g}^{-1}\text{K}^{-1}$ calcite	$8 \text{ W m}^{-1}\text{K}^{-1}$ quartz $3 \text{ W m}^{-1}\text{K}^{-1}$ calcite

Source: CRC handbook and other general databases. (1) Waite, [http://woodshole.er.usgs.gov/operations/hi\\_fi/index.html](http://woodshole.er.usgs.gov/operations/hi_fi/index.html); Handa (1986).

Note: the sign of the latent heat is adopted to capture endothermic-exothermic effects during phase transformation.

*Hydrate.* This phase is made of water and methane, and is assumed to be of constant density (Table 2.1). The mass fraction of water in hydrate  $\alpha = m_w/m_h$  depends on the hydration number  $\chi$  for methane hydrates  $\text{CH}_4\chi\text{H}_2\text{O}$ ; from the atomic masses,  $\alpha = \chi/(0.89 + \chi)$ . In the case of Structure-I,  $\chi = 5.75$  and  $\alpha = 0.866$ . Hydrates found in nature often involve higher hydration numbers (e.g., Handa 1988).

*Liquid.* The liquid phase is made of water and dissolved gas. In the absence of hydrates, the solubility of methane in water [ $\text{mol/m}^3$ ] increases with pressure and decreases with temperature and salt concentration. The opposite is true in the presence of hydrates: the solubility of  $\text{CH}_4$  in water increases with increasing temperature and decreases with increasing pressure (Sun and Duan, 2007). In both cases, the solubility of methane in water is very low; e.g., at  $P_t = 10 \text{ MPa}$  and  $T = 280^\circ\text{K}$ , the mass fraction of methane in water is  $m_m/m_w \sim 1.4 \times 10^{-3}$ . While the contribution of methane dissolution in water to mass transport can be disregarded for gas production studies, we keep the formulation in the code -based on Henry's law- in view of potential related studies such as hydrate formation from dissolved phase. The mass density of the liquid  $\rho_\ell$  depends on temperature  $T$  [ $^\circ\text{K}$ ] and pressure  $P_t$  [ $\text{MPa}$ ]. The asymptotic solution for small volumetric changes is:

$$\rho_\ell = \rho_{\ell o} \left( 1 + \frac{P_\ell}{B_\ell} \right) \left[ 1 - \beta_{T_\ell} \left( \frac{T - 277^\circ\text{K}}{5.6} \right)^2 \right] \quad 272^\circ\text{K} < T < 300^\circ\text{K} \quad (2.1)$$

where  $\rho_{\ell 0}=0.9998 \text{ g/m}^3$  is the mass density of water at atmospheric pressure and at  $T=277^\circ\text{K}$ ,  $B_{\ell}=2000 \text{ MPa}$  is the bulk stiffness of water, and  $\beta_{T\ell}=0.0002^\circ\text{K}^{-1}$  is the thermal expansion coefficient. This equation properly captures the thermal expansion water experiences below and above  $T=277^\circ\text{K}$ . The formulation proposed herein is capable of considering cryogenic suction effects and the presence of unfrozen water at freezing temperature. However, hereafter (for the sake of simplicity) it is assumed that all the liquid water is transformed into ice at freezing temperature.

*Gas.* It is considered that the gas phase consists of pure methane gas. The mass density of the gas phase is pressure  $P_g$  [MPa] and temperature  $T$  [ $^\circ\text{K}$ ] dependent and it can be estimated using the ideal gas law. Experimental data in Younglove and Ely (1987) is used to modify the ideal gas law for methane gas in the range of interest (fitted range:  $270^\circ\text{K}<T<290^\circ\text{K}$  and  $0.1\text{MPa}<P_g<40\text{MPa}$ ):

$$\rho_g = \frac{M_m P_g}{R T} \left[ 1176 + 12.7 \frac{P_g}{1\text{MPa}} - 0.45 \left( \frac{P_g}{1\text{MPa}} \right)^2 \right] \quad (2.2)$$

where the gas constant  $R=8.314 \text{ J}/(\text{mol}^\circ\text{K})$  and the molecular mass of methane  $M_m=16.042 \text{ g/mol}$  (example:  $\rho_g=86 \text{ g/m}^3$  at  $T=280^\circ\text{K}$  and  $P_g=10\text{MPa}$ ).

## 2.2. Volumetric Relations

The total volume  $V_{\text{total}}$  is the sum of the partial volume of each  $\beta$ -phase  $V_\beta$ , where the sub-index  $\beta$  is one of  $[s, \ell, g, h, i]$  for solid, liquid, gas, hydrate or ice phases,  $V_{\text{total}} = \sum V_\beta$ . Assuming that the solid mineral is a non-reactive phase, the total porosity is defined as the ratio of the volume of voids  $V_v=1-V_s$  to the total volume  $V_{\text{total}}$ ,

$$\phi = \frac{V_v}{V_{\text{total}}} = \frac{V_g + V_\ell + V_h + V_i}{V_{\text{total}}} \quad (2.3)$$

The volume of voids  $V_v$  is occupied by the liquid, gas, hydrate and ice phases; the associated volume fractions are  $S_\beta=V_\beta/V_v$ , the following volumetric restriction applies

$$S_\ell + S_g + S_h + S_i = 1 \quad (2.4)$$

## 2.3. Balance Equations

The macroscopic balance of either mass or energy relates the rate of change per unit volume to the flux in-and-out of the volume, and takes into consideration external inputs as well. Mass balance equations are written for the three species: water  $w$ , methane  $m$ , and for the mineral that makes the particles (no letter is required, it coincides with the solid). The mass flux in balance equations includes advective transport by the fluid and the movement of the sediment relative to a fixed reference frame. The proposed framework can also accommodate non-advective diffusive transport of species in the phases (i.e.  $w$  in  $g$ , and  $m$  in  $l$ ).

*Mass Balance: Water.* The mass of water per unit volume of the porous medium combines the mass of water in the liquid, hydrate and ice phases. The water flux associated to the liquid, hydrate and ice phases with respect to a fixed reference system combines Darcian flow with respect to the solid phase  $\mathbf{q}_\ell$  [m/s] and the motion of the whole sediment with velocity  $\mathbf{v}$  [m/s] relative to the fixed reference system. Then, the water mass balance can be expressed as:

$$\frac{\partial}{\partial t} \underbrace{[(\rho_\ell S_\ell + \alpha \rho_h S_h + \rho_i S_i) \phi]}_{\text{mass water per unit volume}} + \nabla \cdot \left[ \underbrace{\rho_\ell \mathbf{q}_\ell}_{\text{w in liquid}} + \underbrace{\rho_\ell S_\ell \phi \mathbf{v}}_{\text{w in hydrate}} + \underbrace{\alpha \rho_h S_h \phi \mathbf{v}}_{\text{w in hydrate}} + \underbrace{\rho_i S_i \phi \mathbf{v}}_{\text{w in ice}} \right] = f^w \quad (2.5)$$

where  $\rho$  [g/m<sup>3</sup>] represents the mass density of phases and  $\alpha$  is the mass fraction of water in hydrate. The external water mass supply per unit volume of the medium  $f^w$  [g/(m<sup>3</sup>s)] is typically  $f^w=0$ ; however, the general form of the equation is needed to model processes such as water injection at higher temperature as part of the production strategy. The first term includes the water mass exchange during hydrate and formation/dissociation. Note that the hydrate and ice phases are assumed to move with the solid particles.

*Mass Balance: Methane.* The total mass of methane per unit volume of the hydrate bearing sediment is computed by adding the mass of methane per unit volume of the gas and hydrate phases taking into consideration the volume fractions  $S_g$  and  $S_h$ , the mass fraction of methane in hydrate  $(1-\alpha)$ , and the porosity of the porous medium  $\phi$ . As in the case of water balance, the flux of methane in each phase combines advective terms relative to the porous matrix and the motion of the porous medium with velocity  $\mathbf{v}$  [m/s] relative to the fixed reference system

$$\frac{\partial}{\partial t} \underbrace{[\rho_g S_g + (1-\alpha) \rho_h S_h] \phi}_{\text{mass of methane per unit volume}} + \nabla \cdot \left[ \underbrace{\rho_g \mathbf{q}_g}_{\text{m in gas}} + \underbrace{\rho_g S_g \phi \mathbf{v}}_{\text{m in gas}} + \underbrace{(1-\alpha) \rho_h S_h \phi \mathbf{v}}_{\text{m in hydrate}} \right] = f^m \quad (2.6)$$

In this case,  $f^m$  [g/(m<sup>3</sup>s)] is an external supply of methane, expressed in terms of mass of methane per unit volume of the porous medium. Typically,  $f^m=0$ ; however, the general expression may be used to capture conditions such as methane input along a pre-existing fault. The first term takes into consideration the methane mass exchange between the hydrate phase and the gas phase during hydrate formation-dissociation.

*Mass Balance: Mineral.* The mineral specie is only found in the solid particles. The mass balance equation follows:

$$\frac{\partial}{\partial t} \underbrace{[\rho_s (1-\phi)]}_{\text{mass mineral per unit volume}} + \nabla \cdot \underbrace{[\rho_s (1-\phi) \mathbf{v}]}_{\text{m in solid}} = 0 \quad (2.7)$$

where  $\rho_s$  [g/m<sup>3</sup>] is the mass density of the mineral that makes the solid particles.

*Mass Balance: Solutes.* The total solute mass balance per each chemical species dissolved in the liquid phase can be expressed as:

$$\frac{\partial}{\partial t} \underbrace{(C_s S_\ell \rho_\ell \phi)}_{\text{mass s per unit volume}} + \nabla \cdot \left[ \underbrace{\mathbf{D} \rho_\ell \nabla C_s}_{\text{non advective flux of s}} + \underbrace{C_s \rho_\ell \mathbf{q}_\ell}_{\text{s in liquid}} + \underbrace{C_s \rho_1 S_1 \phi \mathbf{v}}_{\text{s in liquid}} \right] = f^s \quad (2.8)$$

where  $C_s$  is concentration of the solute ‘s’ expressed in mass of solute per mass of water [kg/kg] and  $\mathbf{D}$  hydrodynamic dispersion tensor that includes both molecular diffusion and mechanical dispersion (Olivella et al., 1994, 1996).  $f^s$  is a sink source of solute. One balance equation is necessary per each species in the liquid phase. One chemical species is sufficient for the aims of this work. A more complex reactive transport model is available when necessary (more details in Guimarães et al., 2007).

Other species such as salts, gases and fluids such as  $\text{CO}_2$  can be included as needed. While salt is expected to play a secondary role in dissociation and production studies, it is often a tracer of ongoing dissolution due to “freshening”.

*Energy Balance.* The energy balance equation is expressed in terms of internal energy per unit volume [ $\text{J}/\text{m}^3$ ], presuming that all phases are at the same temperature and in equilibrium. In the absence of fluxes, the total energy per unit volume of the medium is:

$$\frac{E}{V_{\text{total}}} = e_s \rho_s (1 - \phi) + (e_\ell \rho_\ell S_\ell + e_g \rho_g S_g + e_h \rho_h S_h + e_i \rho_i S_i) \phi \quad (2.9)$$

where  $e$  [ $\text{J}/\text{g}$ ] represents the specific internal energy per unit mass of each phase. These values are computed using the specific heat of the phases  $c$  [ $\text{J}/(\text{g}\cdot\text{K})$ ] and the local temperature  $T$  relative to a reference temperature  $T_o=273^\circ\text{K}$  (see Table 2). The selected reference temperature does not affect the calculation: the system is presumed to start at equilibrium, and energy balance is tracked in terms of “energy changes” from the initial condition.

Energy consumption or liberation associated to hydrate formation/dissociation and ice formation/fusion are taken into consideration using the corresponding latent heats or changes in enthalpy  $L$  [ $\text{J}/\text{g}$ ], as summarized in Table 2.1. Hence, the formulation inherently captures energy changes during endothermic or exothermic processes through specific internal energies and the corresponding changes in volume fractions  $S_\ell$ ,  $S_g$ ,  $S_h$  and  $S_i$ .

The energy flux combines (1) conduction through the hydrate bearing sediment  $\mathbf{i}_c$  [ $\text{W}/\text{m}^2$ ], (2) transport by fluid mass advection relative to the mineral skeleton, and (3) transport by the motion of the whole sediment with respect to the fixed reference system. The specific internal energies per unit mass for each species in each phase are seldom known (e.g. methane-in-hydrate). Therefore, the formulation is simplified by working at the level of each phase; furthermore, we also disregard the energy flux associated to the diffusive transport of water or methane in either the liquid or the gas phases. Then, the energy balance equation taking into consideration transport through the phases is:

$$\begin{aligned} f^E = & \frac{\partial}{\partial t} \left\{ \overbrace{[e_s \rho_s (1 - \phi)] + (e_\ell \rho_\ell S_\ell + e_g \rho_g S_g + e_h \rho_h S_h + e_i \rho_i S_i) \phi}^{\text{energy per unit volume of the hydrate bearing sediment}} \right\} + \\ & + \nabla \cdot \mathbf{i}_c + \\ & + \nabla \cdot [ \underbrace{e_\ell \rho_\ell (\mathbf{q}_\ell + S_\ell \phi \mathbf{v})}_{\text{transport in } \ell} + \underbrace{e_g \rho_g (\mathbf{q}_g + S_g \phi \mathbf{v})}_{\text{transport in } g} + \underbrace{e_h \rho_h S_h \phi \mathbf{v}}_{\text{transport in } h} + \underbrace{e_i \rho_i S_i \phi \mathbf{v}}_{\text{transport in } i} + \underbrace{e_s \rho_s (1 - \phi) \mathbf{v}}_{\text{transport in } s} ] \end{aligned} \quad (2.10)$$

The energy supply per unit volume of hydrate bearing sediment  $f^E$  [ $\text{W}/\text{m}^3$ ] can be used to simulate thermal stimulation of the reservoir.

*Momentum Balance (equilibrium).* In the absence of inertial forces (i.e. quasi-static problems) the balance of momentum for the porous medium is the equilibrium equation

$$\nabla \cdot \boldsymbol{\sigma}_t + \mathbf{b} = 0 \quad (2.11)$$

where  $\boldsymbol{\sigma}_t$  [N/m<sup>2</sup>] is the total stress tensor and  $\mathbf{b}$  [N/m<sup>3</sup>] the vector of body forces. The constitutive equations for the hydrate bearing sediment permit rewriting the equilibrium equation in terms of the solid velocities, fluid pressures and temperatures.

#### 2.4. Constitutive Equations

The governing equations are finally written in terms of the unknowns when constitutive equations that relate unknowns to dependent variables are substituted in the balance equations. Note that constitutive equations capture the coupling among the various phenomena considered in the formulation. Given the complexity of the problem, simple yet robust constitutive laws are selected for this simulation.

*Conductive heat flow.* The linear Fourier's law is assumed between the heat flow  $\mathbf{i}_c$  [W/m<sup>2</sup>] and thermal gradient. For three dimensional flow conditions and isotropic thermal conductivity,

$$\mathbf{i}_c = -\lambda_{\text{hbs}} \nabla T \quad (2.12)$$

where  $\lambda_{\text{hbs}}$  [W/(m.K)] is the thermal conductivity of the hydrate bearing sediment. A non-linear volume average model is selected to track the evolution of  $\lambda_{\text{hbs}}$ ,

$$\lambda_{\text{hbs}} = \left[ (1-\phi)\lambda_s^\beta + \phi \left( S_h \lambda_h^\beta + S_i \lambda_i^\beta + S_g \lambda_g^\beta + S_\ell \lambda_\ell^\beta \right) \right]^{1/\beta} \quad (2.13)$$

The parallel model corresponds to  $\beta=1$  and the series model to  $\beta=-1$ . Experimental data gathered for dry, water saturated and hydrate filled kaolin and sand plot closer to the series model in all cases (Yun et al 2007, Cortes et al., 2009). An adequate prediction for all values and conditions is obtained with  $\beta \approx -0.2$ .

*Advective Fluid Flow.* The advective flux of the liquid and the gas phases  $q_\ell$  and  $q_g$  [m/s] are computed using the generalized Darcy's law (Gens and Olivella, 2001):

$$\mathbf{q}_\alpha = -\mathbf{K}_\alpha (\nabla P_\alpha - \rho_\alpha \mathbf{g}) \quad \alpha = \ell, g \quad (2.14)$$

where  $P_\alpha$  [N/m<sup>2</sup>] is the phase pressure, and the vector  $\mathbf{g}$  is the scalar gravity  $g=9.8$  m/s<sup>2</sup> times the vector  $[0,0,1]^T$ .

The tensor  $\mathbf{K}_\alpha$  [m<sup>4</sup>/(N.s)] captures the medium permeability for the  $\alpha$ -phase in 3-D flow; if the medium is isotropic,  $\mathbf{K}_\alpha$  is the scalar permeability  $K_\alpha$  times the identity matrix. The permeability  $\mathbf{K}_\alpha$  depends on the intrinsic permeability  $\mathbf{k}$  [m<sup>2</sup>] of the medium, the dynamic viscosity of the  $\alpha$ -phase  $\mu_\alpha$  [N.s/m<sup>2</sup>] and the relative permeability  $k_{r\alpha}$  [ ]:

$$\mathbf{K}_\alpha = \mathbf{k} \frac{k_{r\alpha}}{\mu_\alpha} \quad \alpha = \ell, g \quad (2.15)$$

The viscosity of the liquid  $\mu_\ell$  phase varies with temperature T [°K] (i.e. Olivella, 1995):

$$\mu_\ell [\text{Pa.s}] = 2.1 \cdot 10^{-6} \exp\left(\frac{1808.5 \text{ }^\circ\text{K}}{T}\right) \quad (2.16)$$

While the viscosity of gases is often assumed independent of pressure, experimental data in the wide pressure range of interest shows otherwise. Published data in Younglove and Ely (1987) are fitted to develop a pressure and temperature dependent expression for the viscosity of methane gas (fitted range:  $270^\circ\text{K} < T < 290^\circ\text{K}$  and  $0.1\text{MPa} < P_g < 40\text{MPa}$ ):

$$\mu_g [\text{Pa.s}] = 10.3 \cdot 10^{-6} \left[ 1 + 0.053 \frac{P_g}{\text{MPa}} \left( \frac{280 \text{ }^\circ\text{K}}{T} \right)^3 \right] \quad (2.17)$$

The intrinsic permeability of the hydrate-bearing medium k with hydrate saturation  $S_h$  and porosity  $\phi$  is estimated from the intrinsic permeability in the medium without hydrates  $k_0$  determined at porosity  $\phi_0$  (Minagawa et al., 2008):

$$k = k_0 \frac{\phi^3}{(1-\phi)^2} \frac{(1-\phi_0)^2}{\phi_0^3} (1-S_h - S_i)^n \quad (2.18)$$

While the trend may higher than linear in the factor  $(1-S_h-S_i)$ , i.e., the value of k remains low until the fluid percolates through the system, a linear trend is assumed in the current version. The relative permeabilities for liquid  $k_{rl}$  and gas  $k_{rg}$  increase as the degree of saturation of each phase increases with respect to the mobile phase saturation  $S_\ell + S_g$ . A single parameter power function properly reproduces experimental data

$$k_{rl} = \left( \frac{S_\ell}{S_\ell + S_g} \right)^a = (S_\ell^*)^a \quad (2.18)$$

$$k_{rg} = \left( 1 - \frac{S_\ell}{S_\ell + S_g} \right)^b = (1 - S_\ell^*)^b \quad (2.19)$$

where  $S_\ell^* = S_\ell / (S_\ell + S_g)$  is the effective liquid saturation in the hydrate bearing sediment. Exponents  $a$ ,  $b$  are typically 3-4 (see Gupta et al, 2006; Minagawa et al, 2008). The relative permeability of a phase vanishes when the phase stops percolating (in the absence of other coupling phenomena); percolation thresholds vary around  $S_g \sim 0.3$  and  $S_\ell \sim 0.3$  for gas and liquid flow. While the power function does not stop flow at percolation thresholds, relative permeabilities become very small and do not contribute to transport phenomena relevant to production processes.

The interfacial tension between liquid and gas sustains the difference between the liquid and gas pressures  $P_\ell$  and  $P_g$ . Let's define the capillary pressure  $P_c = P_g - P_\ell$ . In a porous network, the capillary pressure and the effective liquid saturation  $S_\ell^*$  are related (van Genuchten, 1978):

$$S_{\ell}^* = \frac{S_{\ell}}{S_{\ell} + S_g} = \left[ 1 + \left( \frac{P_c}{P_o} \right)^{\frac{1}{1-\lambda}} \right]^{-\lambda} \quad (2.20)$$

The model parameters  $P_o$  (can be taken as the air entry value) and  $\lambda$  (typically  $0.05 < \lambda < 0.4$ ) relate to the porosity structure of the hydrate bearing sediment: finer grains and denser sediments imply higher  $P_o$  and the lower  $\lambda$  values.

*Effective Porosity.* The effective porosity is calculated based on the volume of void occupied by liquid and gas phase:

$$\phi_{\text{eff}} = \frac{V_{\text{tot}} - V_s - V_h - V_i}{V_{\text{tot}}} = \phi_o (1 - S_h - S_i) \quad (2.22)$$

where  $\phi_o$  is the granular porosity  $(V_{\text{tot}} - V_s) / V_{\text{tot}}$ .

*Constitutive Model for Mechanical Response.* The implemented robust constitutive modeling which represents the realistic mechanical behavior of HBS is described in Section 4.

## 2.5. Phase Boundaries - Reaction Kinetics

Pressure and temperature defined the phase boundary for methane hydrate and ice. The selected expression for the phase boundary of methane hydrate follows the format in Sloan and Koh (2008), but it is adjusted to satisfy values computed using the *HWHYD software* [2001]:

$$P_{\text{eq-mh}} [\text{kPa}] = e^{\left( 40.234 - \frac{8860}{T_{\text{eq}} [^{\circ}\text{K}]} \right)} \quad \text{methane hydrate} \quad (2.23)$$

The phase boundary of the gas hydrate mixture is also influenced by the salinity of water. Based on Kamath and Godbole (1987) studies, a linear relationship between the temperature of disassociation and the salinity weight concentration for a given pressure was assumed. We account for the effect of salinity on hydrate phase boundary correcting (2.23) as follows:

$$P_{\text{eq-mh}} [\text{kPa}] = e^{\left( 40.234 - \frac{8860}{T_{\text{eq}} - \alpha_s I_s} \right)} \quad (2.24)$$

where,  $\alpha_s$  is the slope of the temperature-salinity curve (assumed as 0.55) and  $I_s$  is the salinity weight concentration.

The phase boundary for the ice-water transition exhibits low sensitivity to pressure. For the most common  $I_h$  ice phase, the linear fit for the pressure range between 0 MPa and 20 MPa is (based on the equation provided by Wagner and Kretzschmar (2008):

$$P_{\text{eq-ice}} [\text{MPa}] = 13.0 (273.16 - T [^{\circ}\text{K}]) \quad \text{Ice} \quad (0 \leq P \leq 20 \text{ MPa}) \quad (2.25)$$

Four regions emerge for gas-water systems when the hydrate stability and the ice-water boundaries are superimposed on the pressure-temperature PT-space, as shown in Figure

2.2. The presence of free gas, water, ice and hydrate in each quadrant depends on the relative mass of water and gas, and the PT trajectory. Note that the ice+gas condition  $I+G$  in the c-quadrant is assumed to remain  $I+G$  upon pressurization into the d-quadrant because of limited solid-gas interaction in the absence of beneficial energy conditions: the enthalpy for ice-to-hydrate transformation is  $H = -48.49$  kJ/mol, i.e., an endothermic process. The simulation of these transformation demands careful attention during code development; examples are presented later in this report.

Either water or free gas may be in contact with the hydrate phase at any given location. Therefore, the model compares the equilibrium pressure  $P_{eq-mh}$  or  $P_{eq-I}$  against a volume average pressure  $P^*$

$$P^* = \frac{S_g}{S_g + S_w} P_g + \frac{S_\ell}{S_g + S_\ell} P_\ell = (1 - S_\ell^*) P_g + S_\ell^* P_\ell \quad (2.26)$$

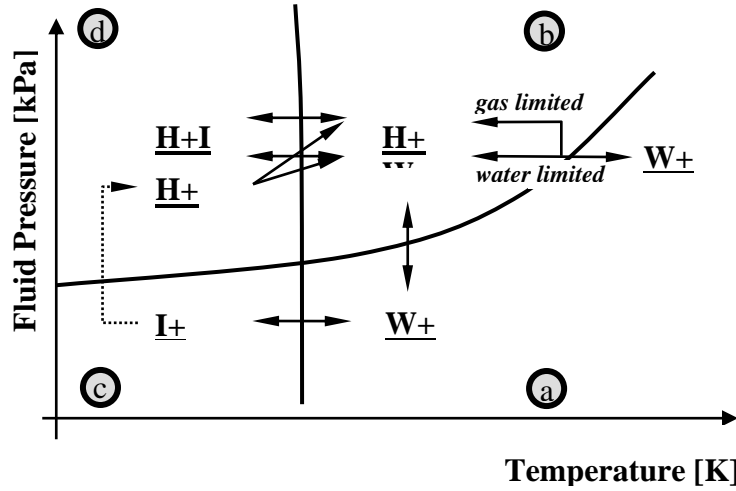


**Figure 2-2** Phase boundaries for water-gas mixtures in the pressure-temperature space. The phases in each quadrant depend on the availability of water and gas, and the PT trajectory.

Local equilibrium conditions are attained much faster than the duration of the global process in most THCM problems; we assume local equilibrium at all times, but consider kinetics-controlled formation and dissociation for both hydrate and ice. Gas hydrate dissociation/formation is generally modeled including explicitly the time in the formulation (e.g. Rutqvist and Moridis (2007), Kimoto et al 2007 and Garg et al. 2008). We propose a totally different approach, inspired in time independent kinetic models, as for example, Saturation-Index based models to simulate precipitation/dissolution phenomena in porous media (e.g. Lasaga, 1998). It is assumed that the rate of formation or dissociation is driven by the distance  $\delta$  to the corresponding equilibrium phase boundary

$$\delta = \sqrt{\left[ \delta_T (T - T_{eq}) \right]^2 + \left[ \delta_P (P_{fl} - P_{eq}) \right]^2} \quad \text{both methane hydrate and ice} \quad (2.27)$$

where  $\delta_T$  [ $^{\circ}K^{-1}$ ] and  $\delta_P$  [ $MPa^{-1}$ ] are scaling parameters; default values are  $\delta_T=1/^{\circ}K$  and  $\delta_P=0.1/MPa$ . The change in hydrate or ice volume fraction applied in a given time step is

a fraction  $\beta$  of the potential change  $\Delta S_h$  or  $\Delta S_i$ . The reduction factor  $0 \leq \beta \leq 1.0$  is a function of the distance to the phase boundary:

$$\beta = 1 - q^\delta \quad (2.28)$$

so, the updated hydrate or ice volume fraction at time interval  $j+1$  outside the stability field is

$$S^{j+1} = S^j + \beta \Delta S \quad \text{for either ice or hydrate} \quad (2.29)$$

This flexible formulation allows to capture different rates of reaction (without invoking specific surface as in models based on results by Kim et al. 1987), relative to mass flux and drainage conditions. The preselected parameter 'q' establishes the rate of change (default value  $q=0.5$ ). Drained conditions can be simulated by selecting high q-values so that acceptably low excess pore fluid generation is predicted throughout the medium (dissociation stops when  $q=1$  and the rate of dissociation becomes  $\Delta S/\Delta t=0$ ).

## 2.6. Computer code

The mathematical formulation presented above has been implemented in the finite element computer program CODE\_BRIGHT, (Olivella et al. 1996), a code designed to analyze numerically coupled THCM problems in porous media. It supports multi-phase, fully coupled thermo-hydro-chemo-mechanical sediment response. We adapt and expand it to represent all species and phases encountered in HBS. Details related to the code can be found elsewhere (e.g. Olivella et al., 1996), only the main aspects are summarized as follows: (1) The state variables are: solid velocity,  $\mathbf{u}$  (one, two or three spatial directions); liquid pressure  $P_l$ , gas pressure  $P_g$ , temperature  $T$  and chemical species concentration. (2) Small strains and small strain rates are assumed for solid deformation. (3) Thermal equilibrium between phases in a given element is assumed. (4) We consider the kinetics in hydrate formation/dissociation as a function of the driving temperature and fluid pressure deviations from the phase boundary, considering the mass fraction of methane in hydrate  $S_h$  as the associated variable. (5) All constitutive equations are modified and new equations are added to properly accommodate for the behavior of hydrate bearing sediments and all phases involved.

### 3. IT TOOL FOR HBS

A database compiling the main published data related to hydrate bearing sediments was developed using the Math-cad software. This IT tool compiles the main constitutive equations proposed for the thermo, hydraulic and mechanical problems; including their dependences on temperature, fluids pressures, stresses and water chemistry. The database also incorporates the phase laws and phase boundaries (including mixed gases) associated with *HBS*. The main model parameters and their typical range of variation are key components of the database as well.

The IT tool plays a central role in analysis involving *HBS*. As shown in Figure 3.1, the IT tool collects the experimental information gathered from different sources, including in-situ investigation, data from Pressure Core Characterization Tools (*PCCTs*) and experimental information obtained in the laboratory from disturbed samples. As shown in the scheme below, the IT tool is then used to feed the models with appropriate constitutive equations, phase laws and parameters needed in the numerical/analytic simulations. The proposed IT tool is the nexus between the existing information and current knowledge about *HBS* and the numerical/analytic models. In summary, this is a key tool in *HBS* analysis because:

- Serve as a repository for constitutive equations, phase laws and parameters for *HBS*.
- Provide best estimation of properties given limited input
- Guide the back-analysis of test data
- Provide robust correlations
- Assist the validation of available models
- Provide consistent set of parameters for *THCM* simulators

The IT tool will be updated and upgraded as new experimental information and insight on *HBS* behavior become available. This task is shared/complements other projects.

Table 3.1 presents the list of properties contemplated in the IT tool and Table 3.2 shows (as an example) some of the constitutive laws contemplated for the mechanical problem. Likewise, constitutive equations for the thermal and hydraulic problems have been incorporated in the database.

Figures 3.2a and 3.2b presents examples of comparisons between experimental data and results from proposed constitutive equations for mechanical properties. Figure 3.2a is related to predicted strength by Santamarina and Ruppel (2008) and measured strength; while Figure 3.2b is associated with the predicted strength by Miyazaki et al. (2012) and measured strength

Table 3.3 shows some typical phase properties incorporated in the database. Figures 3.3a and 3.3b present the functions for hydrate phase equilibrium in seawater and freezing point of seawater respectively.

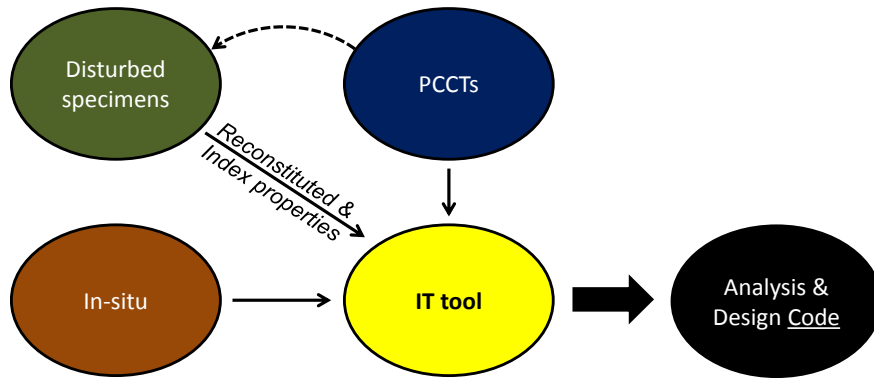


**Figure 3-1** Scheme showing the link between the proposed IT tool, the source of data (for *HBS*) and the modeling.

**Table 3-1:** List of Properties

	Properties
<b>Phase Boundaries</b>	Hydrate phase
	Gas mixtures
	Liquid chemistry
<b>Mechanical</b>	Strength
	Stiffness
	Wave velocities
<b>Hydraulic</b>	Soil water characteristic curve
	Hydraulic conductivity
	Permeability of HBS
	Relative permeability
<b>Thermal</b>	Thermal conductivity
	Heat capacity

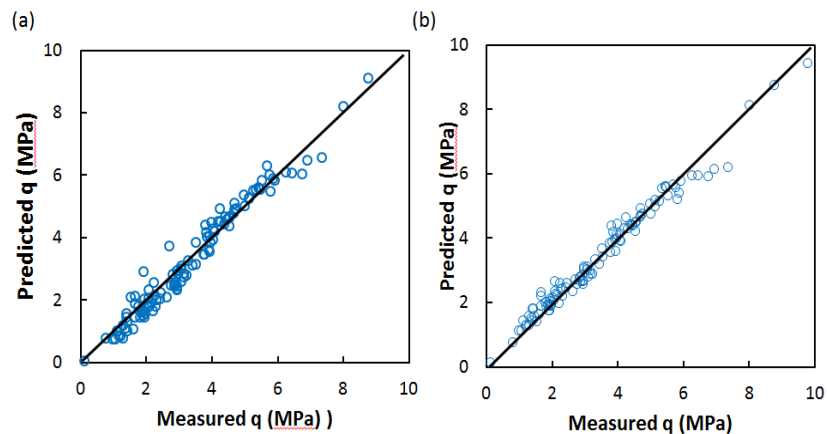


**Figure 3-2** Examples of data and formulations for mechanical properties: a) comparison of predicted strength by Santamarina and Ruppel (2008) and measured strength; and b) comparison of predicted strength by Miyazaki et al. (2012) and measured strength.

**Table 3-2: Mechanical properties**

Properties	Formulation	Reference
Strength	$q = \frac{\sin \phi'}{1 - \sin \phi'} \sigma_3' + \frac{\cos \phi'}{1 - \sin \phi'} c' + \alpha S^\beta$	Santamarina and Ruppel (2008)
	$q = a\sigma_3' + bq_h \left(\frac{S_h}{n}\right)^2$	Miyazaki et al. (2012)
Stiffness	$E_{50} = a \left(\frac{\sigma_3'}{1kPa}\right)^b + cE_{50} S_h^d$	Jung et al. (2012)
S-wave velocity	$V_s = \sqrt{\left(\frac{V_h S_h^2}{n}\right)^2 + \left[\alpha \left(\frac{\sigma_v' + \sigma_h'}{2kPa}\right)^{\beta-2}\right]}$	Santamarina and Ruppel (2008)
	Effective medium model	Helgend et al. (1999), Ecker et al. (1998)
P-wave velocity	$V_p^2 = V_s^2 \left[ \frac{4}{3} + \frac{2(1+v_{sk})}{3(1-2v_{sk})} \right] + \frac{1}{\rho_{hbs}} \left[ \frac{n(1-S_h)}{B_w} + \frac{nS_h}{B_h} + \frac{1-n}{B_m} \right]$	Santamarina and Ruppel (2008)
	Effective medium model	Helgend et al. (1999), Ecker et al. (1998)

**Table 3-3: Phase properties**

Properties	Formulation	Reference
Hydrate phase equilibrium	$P [MPa] = 1MPa \times e^{\frac{a+b}{T/K}}$	Sloan and Koh (2008)
	Equation considering effect of salinity	Tishchenko et al. (2005)
Gas density Liquid density	Van der Waals Equation of State	Beyer (2005)
	Peng-Robinson Equation of State	Peng and Robinson (1976)
	Duan's Equation of State	Duan et al. (1992)
Gas viscosity	$\mu_g [Pa \cdot s] = 1.03 \times 10^{-5} [Pa \cdot s] \left[ 1 + 0.053 \frac{P}{MPa} \left( \frac{280K}{T} \right)^3 \right]$	Younglove and Ely (1987)
Liquid viscosity	$\mu_w [Pa \cdot s] = 2.1 \times 10^{-6} [Pa \cdot s] e^{\frac{1808.5K}{T}}$	Sanchez and Santamarina
Freezing point of seawater	$T_f = -0.0575S(\%) + 1.710523 \times 10^{-3} S(\%)^{3/2} - 2.154996 \times 10^{-4} S(\%)^2 - 0.0753P$	Fofonoff and Millard (1983)

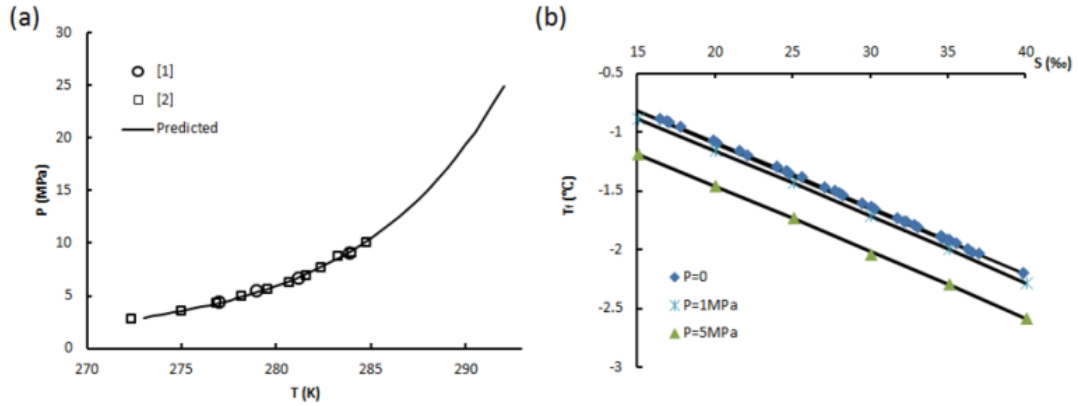


**Figure 3-3** Phase boundaries: a) hydrate phase equilibrium in seawater; and b) freezing point of seawater. The user interface allows a readable introduction for each property; including: “Descriptions”, “Definitions and parameters”, “Functions/ scripts”, and “Calculations/examples”. Figure 3.4 shows a Mathcad based IT tool prototype.

<b>PHASE BOUNDARIES</b>
Descriptions _____
Definitions and parameters _____
functions/scripts _____
Calculations/examples _____
<b>SMALL STRAIN PROPERTIES</b>
Description _____
Definitions and parameters _____
Functions/scripts _____
Calculations/examples _____
<b>LARGE STRAIN PROPERTIES</b>
Description _____
Definitions and parameters _____
Functions/scripts _____
Calculations/examples _____
<b>HYDRAULIC PROPERTIES</b>
Descriptions _____
Definitions/parameters _____
Functions/scripts _____
Calculations/examples _____
<b>THERMAL PROPERTIES</b>

**Figure 3-4** Mathcad based IT tool prototype.

Input, feature, and reference of functions were introduced in “Descriptions”, while parameters in functions were defined in “Definitions and parameters”, scripts can be found in “Functions/scripts”, and a simple example of application of functions can be found in “Calculations/examples”.

Model predictions can be made by providing input and choosing proper parameters. Also recommended parameters are listed in the “Parameters to choose” section. Figures 3.5 show examples of the Mathcad based IT tool interfaces for parameter input/selection.

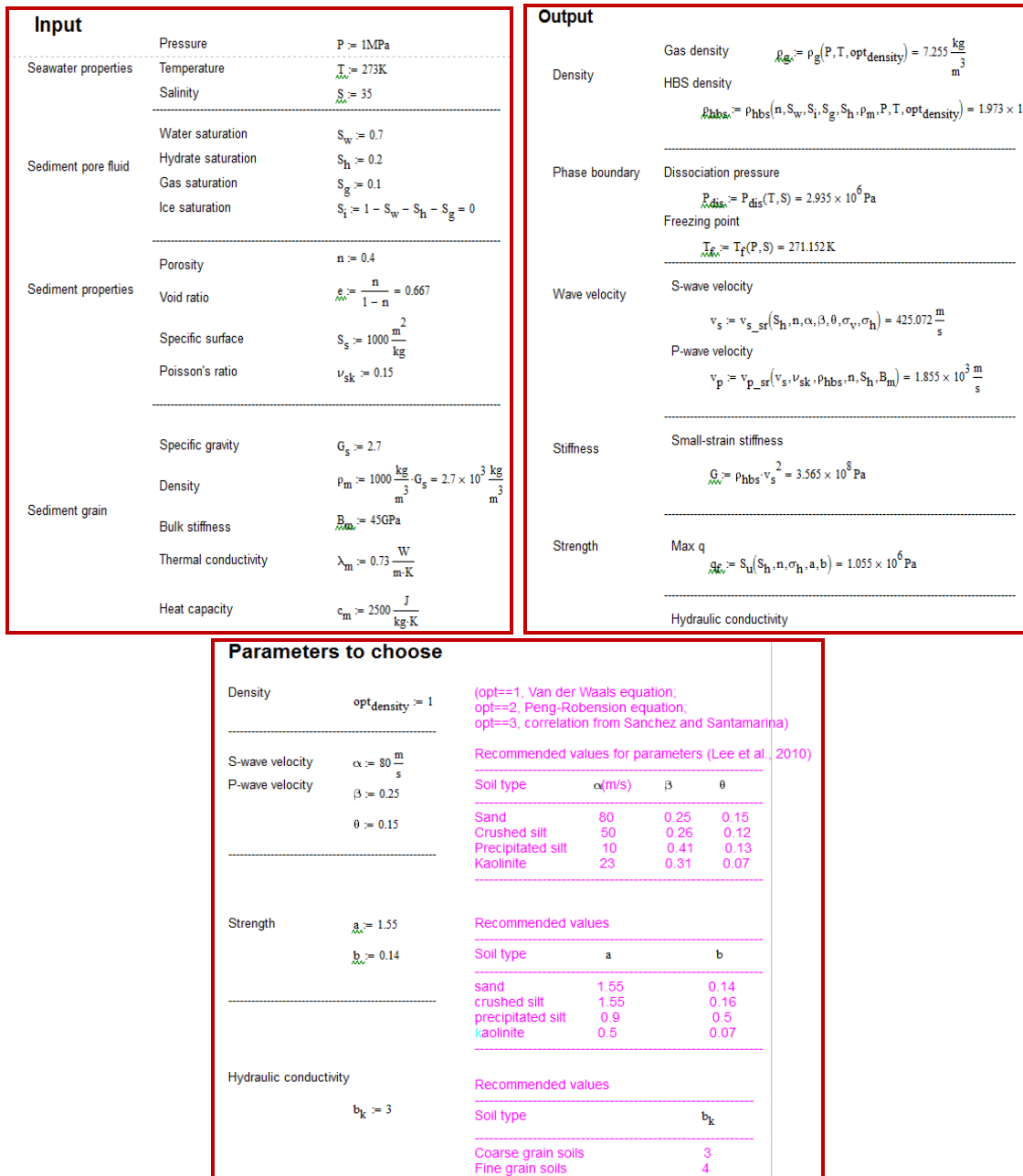


Figure 3-5 Example of Mathcad based IT tool interfaces for parameter input/selection.

#### 4. GEOMECHANICAL MODELING

Geomechanics is a key component in the numerical modeling of engineering problems involving *HBS*. Several types of mechanical constitutive models for hydrate bearing sediment have been proposed in the last few years. (Miyazaki et al., 2012; Kimoto et al., 2007; Klar et al., 2010; Rutqvist and Moridis, 2007; Pinkert and Grozic, 2014; Pinkert et al., 2015; Lin et al., 2015; Gai and Sánchez, 2017; Sultan and Garziglia, 2011; Uchida et al., 2012; Uchida et al., 2016; Gai and Sanchez, 2016; Gai, 2016; Jiang et al., 2014; Jiang et al., 2015; Liu et al., 2014; Shen et al., 2016a; Shen et al., 2016b; Yu et al., 2016; Shen and Jiang, 2016, Sanchez et al., 2017). Only a few of them are discussed below. For example, Miyazaki et al. (2012) suggested a nonlinear elastic model for hydrate bearing sands based on the Duncan-Chang model (Duncan et al., 1970). The Mohr–Coulomb (*MC*) model has been adopted by several researchers to describe the behavior of *HBS*. For instance, Rutqvist and Moridis (2007) simulated the geomechanical changes during gas production from *HBS* undergoing depressurization-induced dissociation using a modified *MC* model. Klar et al. (2010) proposed a single-phase elastic–perfectly plastic *MC* model for hydrate soils based on the concept of effective stress that incorporates an enhanced dilation mechanism. Pinkert (2014) and Grozic (2015) proposed a model based on a non-linear elastic model (dependent on  $S_h$ ) and the on *MC* failure criterion. The extension of *MC* type models to deal with hydrates is generally carried out by incorporating a dependency of the cohesion with the hydrate concentration (Klar et al., 2010; Rutqvist and Moridis, 2007; Pinkert et al., 2014). However, Pinkert (2016) showed that by using the Rowe’s stress-dilatancy theory (Rowe, 1962) it was possible to model the behavior of hydrates without the need of enhancing the cohesion with the increase of  $S_h$ . As it is well-known, *MC* type models cannot capture plastic deformations before failure and are unable to simulate positive (compressive) plastic deformations.

The model based on the Modified Cam-Clay (*MCC*) framework proposed by Sultan and Garziglia (2011) was validated against the experimental data reported by Masui et al. (2005; 2008). The global performance of the model was satisfactory, however, it was unable to capture the softening behavior observed in these experiments. The critical state model for *HBS* proposed by Uchida et al. (2012; 2016) is based on the *MCC* model and its validation was performed using published experiments conducted at constant hydrate saturation. Jeen-Shang et al. (2015) developed a critical state model based on the ‘spatial mobilized plane’ and sub-loading concepts. Kimoto et al. (2007) proposed an elasto–viscoplastic model to analyze ground deformations induced by hydrate dissociation. The discrete element method has also been used to simulate the mechanical behavior of *HBS* (e.g. Jiang et al., 2014; Jiang et al., 2015; Liu et al., 2014; Shen et al., 2016a; Shen and Jiang, 2016; Shen et al., 2016b; Yu et al., 2016). All the mechanical models discussed above have been used to simulate tests performed at constant hydrate saturation.

In this project a new elasto-plastic model based on the stress partition concept (Carol et al., 2001; Fernandez et al., 2001; Pinyol et al., 2007; Vaunat et al., 2003) and the Hierarchical Single Surface (*HISS*) framework (Desai et al., 1986; 1989; 2000) was developed to provide a general and adaptable geomechanical model for hydrate bearing sediments. Recently published experimental data based on synthetic and natural specimens involving different  $S_h$  and hydrates morphology was adopted to validate the proposed approach. The model application and validation do not limit to cases in which

$S_h$  is maintained constant during the tests (as in previous works), but also include experiments in which dissociation is induced under constant stress. Particular attention is paid to evaluate the behavior of *HBS* during dissociation under different stress levels and tests conditions (i.e., triaxial and oedometric), as well as experiments involving both: reconstituted and natural specimens. The model also allows examining the individual contribution of sediments and hydrates to the mechanical behavior during loading and dissociation, aspect that was not studied before with an elastoplastic model for *HBS*.

This project also aims to study the behavior of hydrates bearing sediments in permafrost stings. In this context the effect of subzero temperatures in the mechanical behavior of soils was investigated.

In the following section the mechanical behavior of *HBS* is briefly discussed to provide some background information about the key features of this material. An advanced model for *HBS* is proposed to deal with problems involving hydrate dissociation. The effect of cryogenic suction on the mechanical response of soil is also discussed.

#### 4.1. Mechanical Behavior of HBS - Experimental evidences

*Loading tests at constant hydrate saturation.* Triaxial tests at constant hydrate saturation have provided very useful information to understand the influence of hydrate saturation and morphology on the mechanical behavior of *HBS*. The presence of hydrates strongly affects key mechanical properties of soils. Gas hydrate increases the shear strength of the sediment (Miyazaki et al., 2011; Masui et al., 2008) Hydrates specimens exhibit a softening behavior (after the peak stress) and more dilation than free hydrate samples (Miyazaki et al., 2011; Masui et al., 2008). The sediment stiffness and strength generally increase with the increase in hydrate saturation (Miyazaki et al., 2011; Masui et al., 2008). It has also been observed that the stiffness of *HBS* degrades during shearing (Hyodo et al., 2014; Hyodo et al., 2005; Hyodo et al., 2013; Li et al., 2011; Masui et al., 2005; Miyazaki et al., 2010; Yun et al., 2007; Zhang et al., 2012).

Hydrates are generally present in sediments in three main morphology types (Soga et al., 2006; Waite et al., 2009): a) cementation (Fig. 4.1a); b) pore-filling (Fig. 4.1b); and c) load-bearing (Fig. 4.1c).

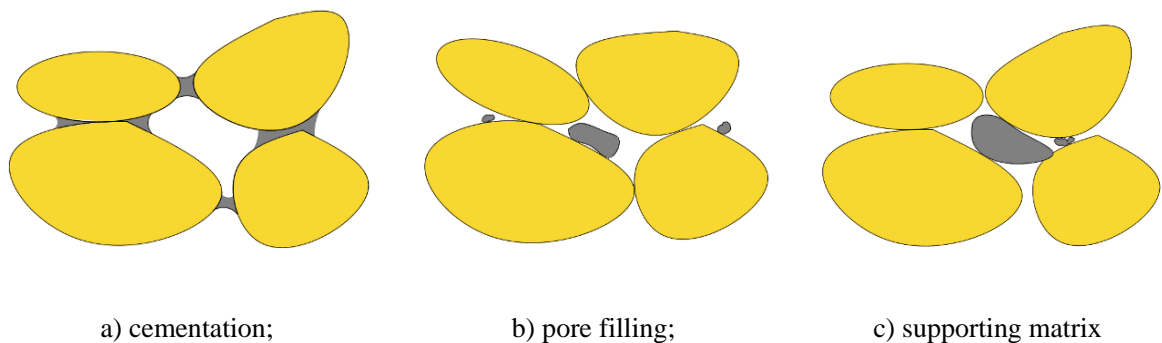


**Figure 4-1** Main types of hydrate morphology: (a) cementation; (b) pore-filling; and (c) load-bearing.

Hydrates formed in the cementation mode are typically found at the contact between particles. A recent microstructural investigation (Chaouachi et al., 2015, that does not involve any mechanical test), speculates about the actual cementation effects provided by the hydrates. However a large number of studies support that hydrates formed in the cementing mode do provide bonding between soil particles (Aman et al., 2013; Clayton et al.; 2010, Jiang et al., 2014; Jiang et al., 2015; Lin et al., 2015; Liu et al., 2014; Masui et al., 2005; Pinkert, 2016; Priest et al., 2009; Shen et al., 2016a; Shen and Jiang, 2016; Shen et al., 2016b; Uchida et al., 2012; Uchida et al., 2016; Waite et al., 2009; Yu et al., 2016). Even a small hydrate saturation can significantly contribute to increase the sediment stiffness and strength in this morphology type (Dvorkin and Uden, 2004). As for hydrate morphology type (b), the hydrates nucleate on soil grains boundaries and grow freely into the pore space, without bridging two or more particles together. This type of hydrates also impacts on the mechanical properties of the sediments. When hydrate saturation is above 25%, this morphology turns into the load-bearing type (c) (Berge et al., 1999; Yun et al., 2005; 2006) Sediment permeability and water storage capacity are significantly affected by the presence of hydrates in the load-bearing form (Helgerud et al., 1999). This mode is generally found in fine-grained soils and a typical example is the Mallik 5L-38 sediment (Dai et al., 2004).

Figure 4.2a presents typical results showing the effect of  $S_h$  on stress-strain behavior and strain-volumetric response of natural methane hydrate samples under triaxial conditions (Masui et al., 2008). While figure 4.2b shows the tests conducted by Masui et al. (2005) to study the influence of hydrate morphology on the geomechanical response of hydrate bearing sediments. The sample without hydrates (i.e. pure sediment) exhibited lower stiffness, strength, and dilatancy. The presence of hydrates increases these mechanical properties. The maximum values corresponds to the cementing mode (i.e. type ‘a’, above).

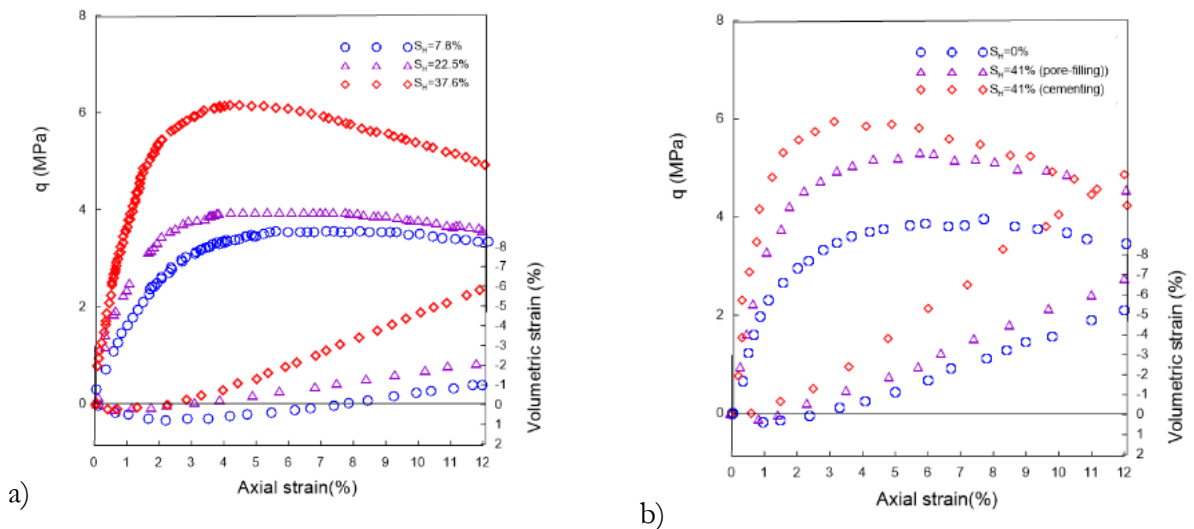


**Figure 4-2** Tests on natural and synthetic HBS in terms of stress-strain behavior and volumetric response a) specimens prepared at different hydrate saturation; and b) samples prepared with different hydrate morphology (Masui et al., 2005; 2008).

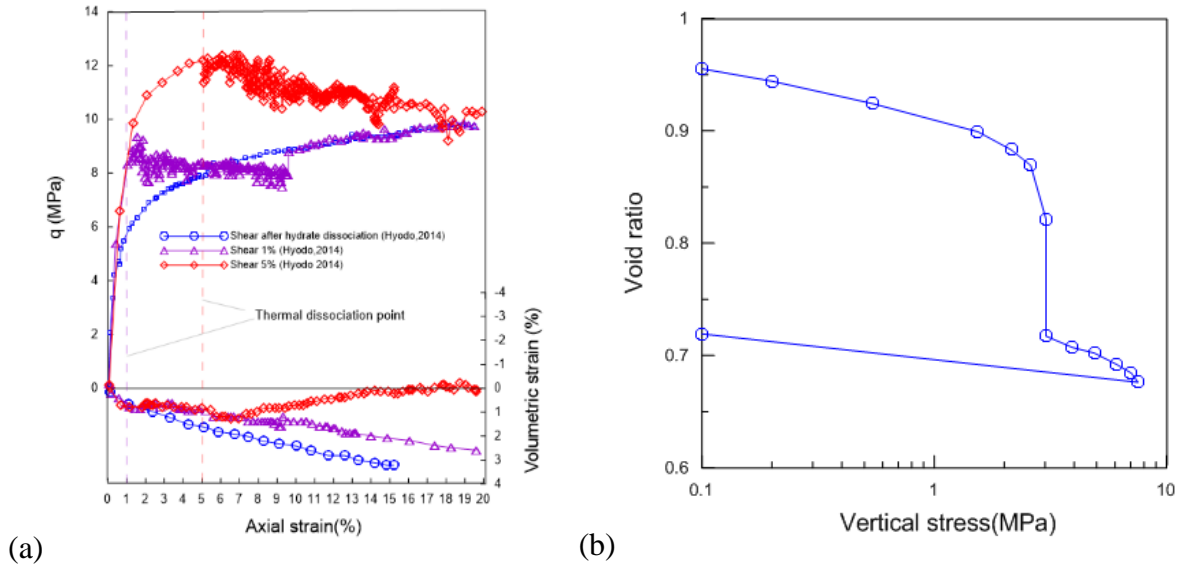
## 4.2. Hydrate dissociation tests under load

Two types of tests involving hydrate dissociation conducted under triaxial and oedometric loading conditions are briefly discussed in this section. Hyodo et al. (2014) adopted a temperature-controlled high pressure triaxial apparatus to mimic the formation and dissociation of methane hydrate in the deep seabed. This device was used to conduct a series of triaxial compression tests on synthetic *HBS* samples under various stress conditions. Toyoura sand was chosen as the host material with a similar porosity (i.e., ~40%), and with  $S_h$  ranging from ~37% to ~53%. Firstly, water and sand were mixed to form the specimen at the target density. The sample was placed in a freezer to keep it stand and then in a triaxial cell, at the target pressure and room temperature. Once the specimen was thawed, methane was injected into the specimen, while keeping the cell pressure and temperature condition inside the hydrate stability zone.

Three experiments were selected in this work for the numerical simulations (see Section 4.4), namely: two triaxial tests at which hydrate dissociation was induced at two different initial axial strains (i.e.,  $\varepsilon_a=1\%$ , and  $\varepsilon_a=5\%$ ), and a third one in which the sample was subjected to shearing after the hydrates dissociated completely. These tests were conducted under isotropically consolidated specimens at an effective confining stress  $\sigma'_c=5$  MPa under drained conditions. Figure 4.3a presents the main experimental results. In one of the hydrate dissociation tests, the specimen was firstly sheared up to  $q\approx 8.4$  MPa (i.e., at  $\varepsilon_a=1\%$ ), then hydrate dissociation was induced at constant stress conditions, and once hydrate dissociation was completed, but the shearing continued up to  $\varepsilon_a=20\%$ . A similar procedure was followed for the other test, but the maximum deviatoric load in this cases was  $q\approx 12$  MPa (i.e., at  $\varepsilon_a=5\%$ ).

The responses observed under these tests conditions are quite different. In the first test, the deviatoric stress after hydrate dissociation was smaller than the shear strength of the dissociated sediment, therefore a tendency to harden was observed in the subsequent shearing. However, in the second sample (i.e., dissociation induced at  $\varepsilon_a=5\%$ ) the deviatoric stress was higher than the strength of the dissociated sample. In consequence, a stress-softening behavior was observed during the hydrate dissociation stage, with a tendency of the deviatoric stress to decrease until reaching the maximum deviatoric stress observed in the already dissociated sample. More details about these tests and the associated modeling are presented later on when modeling these tests.

Another set of experiments modeled in this study corresponds to the tests reported by Santamarina et al. (2015). Two natural core samples were extracted from the Nankai Trough, offshore Japan, using the Pressure Core Characterization Tools (*PCCT*) (Santamarina et al., 2012). The tested cores were predominantly sandy- and clayey-silts, but also contained some silty-sands. Hydrate saturation ranged from ~15% to ~74%, with significant concentrations in the silty-sands samples. The *PCCT* was able to maintain the *HBS* cores stable at field conditions. After retrieval, the cores were loaded under oedometric conditions and at some point, hydrate dissociation was induced under constant effective stress conditions. The mechanical behavior of the *HBS* specimens before, during and after dissociation was recorded.



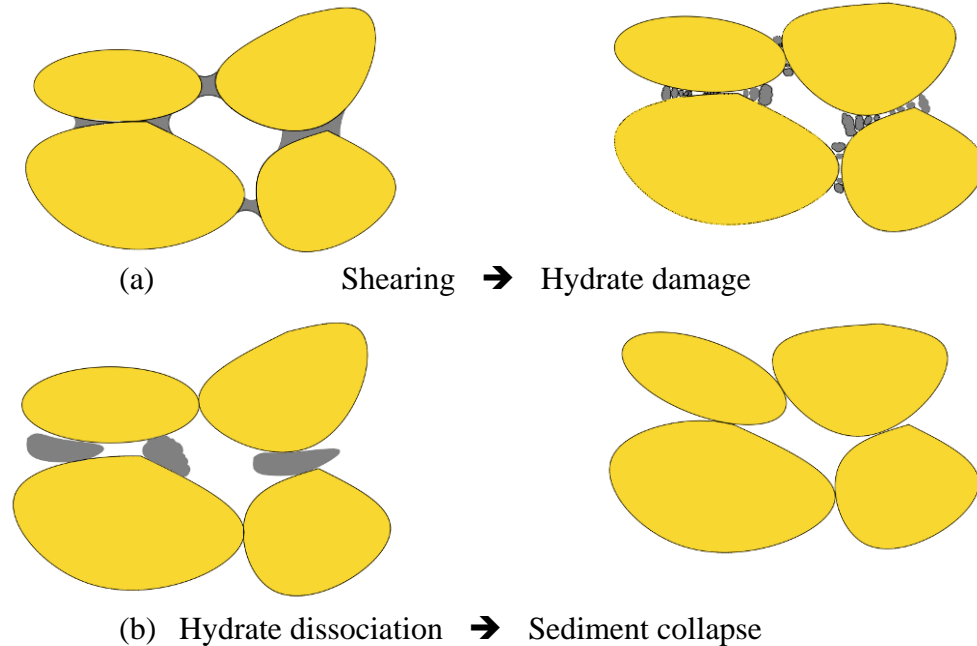
**Figure 4-3** a) Experimental results for drained triaxial tests involving hydrate dissociation (Hyodo, 2014); b) behavior of a natural HBS subjected to loading and dissociation under stress at oedometric conditions (Santamarina et al., 2015).

Figure 4.3b shows the results of a typical test in the ‘effective stress chamber’ (i.e., the sample coded as ‘core-10P’, with an initial  $S_h \sim 74\%$ ). Prior to hydrate dissociation, the specimen was loaded up to an applied effective vertical stress  $\sigma'_v = 3$  MPa, then hydrate dissociation was induced via depressurization, maintaining the effective stress constant. Once the hydrates were fully dissociated, the specimen was loaded up to  $\sigma'_v = 9$  MPa, and it was unloaded afterwards. A significant volumetric collapse-compression deformation was observed during dissociation under load. This test and another one with lower hydrate dissociation (i.e.,  $S_h \sim 18\%$ ) are modeled and discussed later on when modeling these tests

### 4.3. Discussion

The mechanical behavior of *HBS* is highly complex because its response not only depends on the amount of hydrate, but also on the type of pore habit (i.e., cementing, pore-filling, or load-bearing s). It was observed that the behavior of *HBS* during hydrate dissociation (and after it) depends on stress level, as shown in more detail in later on when modeling these tests. It has also been suggested that hydrate bonding effects can be damaged during shearing (Lin et al., 2015; Uchida et al., 2012; Uchida et al., 2016).

The progressive stiffness degradation in tests involving *HBS* is generally very evident. Figure 4.4a illustrates the phenomenon of hydrate damage during shearing. Hydrate dissociation is also accompanied by profound changes in the sediment structure. Figure 4.4b shows schematically the expected changes in the soil structure that lead to the collapse compression deformations observed during dissociation under normally consolidated conditions (e.g., Fig. 4.3b). In summary, the mechanical response of *HBS* is highly non-linear, controlled by multiple inelastic phenomena that depends on hydrate saturation, sediment structure, and stress level. In the following section, two advanced elastoplastic models for *HBS* is presented in detail.



**Figure 4-4** a) Schematic representation of the hydrate damaged during shearing; b) rearrangement of the *HBS* structure upon dissociation.

#### 4.4. Advanced geomechanical model

In this section a new elasto-plastic model based on the stress partition concept (Carol et al., 2001, Fernandez and Santamarina, 2001, Pinyol et al., 2007, Vaunat and Gens, 2003) and the Hierarchical Single Surface (*HISS*) framework (e.g., Gai and Sánchez, 2016, Sánchez) was selected to provide a general and adaptable geomechanical model for hydrate bearing sediments. Recently published experimental data based on synthetic and natural specimens involving different  $S_h$  and hydrates morphology was adopted to validate the proposed approach. The model application and validation do not limit to cases in which  $S_h$  is maintained constant during the tests (as in previous works), but also include experiments in which dissociation is induced under constant stress. Particular attention is paid to evaluate the behavior of *HBS* during dissociation under different stress levels and tests conditions (i.e., triaxial and oedometric), as well as experiments involving both: reconstituted and natural specimens. The model also allows examining the individual contribution of sediments and hydrates to the mechanical behavior during loading and dissociation, aspect that was not studied before with an elastoplastic model for *HBS*.

##### 4.4.1. Model description

The stress-partition concept proposed by Pinyol et al. (2007) for clayed cementing materials is adapted in this work for describing the behavior of *HBS*. The main reason behind the selection of this model is that it is extremely well suited to deal with materials that have two main constituents (i.e. ‘hydrates’ and ‘sediments’ in this case), feature that is not considered in previous models for *HBS*. The model allows to explicitly define specific constitutive models and evolutions laws for each one of those two compounds with the corresponding variables. The modeling of the hydrates can be well represented

by a damage model that is able to account for the material degradation induced by loading and hydrate dissociation. As for the sediment skeleton, a model based on critical state soil mechanics concepts is adopted, which is an appropriate approach for describing the elastoplastic behavior of the soils. The particular constitutive equations adopted hereafter are based on a modification of the *HISS* elasto-plastic model (Desai, 1989; 2000). The proposed framework also incorporates sub-loading and dilation enhancement concepts.

Therefore, the proposed model takes in account two basic aspects related to the presence of hydrates in soils: i) it considers that hydrates contribute (together with the soil skeleton) to the mechanical stability of the sediment, the stress partition concept is used to compute this contribution; and ii) it contemplates that the presence of hydrates alters the mechanical behavior of sediments (e.g., providing hardening and dilation enhancement effects), inelastic mechanisms are incorporated into a critical state model for the sediment to account for these effects.

The main model components and its mathematical formulation are detailed below, introducing firstly some basic relationships, detailing afterwards the specific constitutive models for the hydrates and sediment, and developing finally the global stress-strain equations.

#### 4.4.2. Basic relationships

The stress-partition concept (Pinyol et al., 2007) was adopted to develop the basic relationships. The total volume of the sample ( $V$ ) can be computed as:

$$V = V_s + V_h + V_f \quad (4.1)$$

where  $V_s$  is the volume of sediment skeleton,  $V_h$  is the volume of hydrate,  $V_f$  is the volume occupied by the fluid in the pore space (Figure 4.5).

Assuming that the soil grains are incompressible, the total volumetric strain can be defined as:

$$\varepsilon^v = -\frac{\Delta V_f}{V} - \frac{\Delta V_h}{V} \quad (4.2)$$

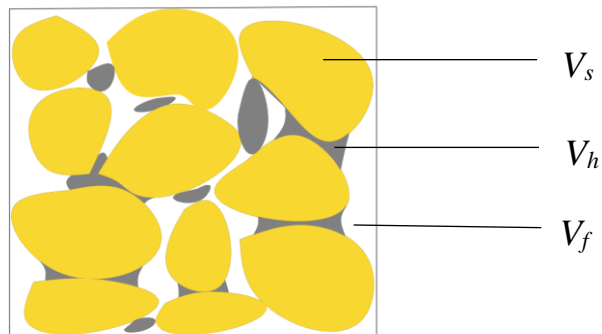


**Figure 4-5** Schematic representation of a *HBS*.

where the superscript  $v$  indicates volumetric strains. The volumetric strain of methane hydrate is computed as:

$$\varepsilon_h^v = -\frac{\Delta V_h}{V_h} \quad (4.3)$$

The deformation of hydrate can be defined locally through the following relationship:

$$-\frac{\Delta V_h}{V} = -\frac{\Delta V_h}{V_h} \frac{V_h}{V} = \varepsilon_h^v C_h \quad (4.4)$$

where  $C_h$  is the volumetric concentration of methane hydrate; which in turns is equal to the porosity ( $\phi$ ) times the hydrate saturation (i.e.,  $C_h = \phi S_h$ ). From equations (4.2) and (4.4), the total volumetric strain accounting for both the sediment skeleton (i.e., subscript  $ss$ ) and the hydrates deformations can be calculated as:

$$\varepsilon^v = \varepsilon_{ss}^v + C_h \varepsilon_h^v \quad (4.4)$$

In a similar fashion, the deviatoric strains can be computed as:

$$\varepsilon^q = \varepsilon_{ss}^q + C_h \varepsilon_h^q \quad (4.5)$$

The relationships that link hydrates and soil skeleton strains are proposed following an approach similar to (Pinyol, 2007):

$$\varepsilon_h^v = \chi \varepsilon_{ss}^v \quad (4.6)$$

$$\varepsilon_h^q = \chi \varepsilon_{ss}^q \quad (4.7)$$

where  $\chi$  is the strain partition variable that evolves during loading. The evolution law for this variable is presented in Section 3.3. From these equations, it can be anticipated that when the sediment skeleton deforms, the local hydrate strain reduces if  $\chi$  decreases. Combining equations above leads to:

$$\varepsilon_h^v = \frac{\chi}{1 + C_h \chi} \varepsilon^v \quad (4.8)$$

$$\varepsilon_h^q = \frac{\chi}{1 + C_h \chi} \varepsilon^q \quad (4.9)$$

Equations (4.26) and (4.27) can also be written as a vector:

$$\mathbf{\varepsilon}_h = \frac{\chi}{1 + C_h \chi} \mathbf{\varepsilon} \quad (4.10)$$

In the following sections the specific constitutive models for the hydrate and sediment skeleton are discussed.

#### 4.4.3. Constitutive model for the methane hydrate

The damage theory is an appropriate framework to describe the degradation process of geomaterials subjected to loading (Kachanov et al., 1987). Isotropic scalar damage models track the degradation behavior of materials via damage variables. Loading degradation occurs when the stress state arrives to a predefined threshold. As mentioned above, previous studies suggested that hydrate can be damaged during shearing (Lin et al., 2015; Uchida et al., 2012; 2016). It is also assumed here that the material degradation takes place during hydrate dissociation. When the stresses are below a pre-established threshold, a linear elastic response of the material is assumed via the following relationships:

$$\boldsymbol{\sigma}_h = \mathbf{D}_{h0} \boldsymbol{\varepsilon}_h \quad (4.11)$$

where  $\boldsymbol{\sigma}_h$  corresponds to the stresses taken by the hydrate and  $\mathbf{D}_{h0}$  is the methane hydrate elastic constitutive matrix of the intact material, as follows:

$$\mathbf{D}_{h0} = \begin{bmatrix} K_{h0} + \frac{4}{3}G_{h0} & K_{h0} - \frac{2}{3}G_{h0} & K_{h0} - \frac{2}{3}G_{h0} & 0 & 0 & 0 \\ & K_{h0} + \frac{4}{3}G_{h0} & K_{h0} - \frac{2}{3}G_{h0} & 0 & 0 & 0 \\ & & K_{h0} + \frac{4}{3}G_{h0} & 0 & 0 & 0 \\ & & & \text{Symetric} & & \\ & & & & G_{h0} & 0 \\ & & & & & G_{h0} \\ & & & & & & G_{h0} \end{bmatrix} \quad (4.12)$$

where  $K_{h0}$  and  $G_{h0}$  are the bulk and shear moduli, of the intact hydrate, respectively. A logarithmic isotropic damage variable ( $L: +\infty > L \geq 0$ ) is introduced to account for the damage induce by loading (Fernandez et al., 2001). The following expressions can be adopted for damaged states:

$$\boldsymbol{\sigma}_h = e^{-L} \mathbf{D}_{h0} \boldsymbol{\varepsilon}_h = \mathbf{D}_h \boldsymbol{\varepsilon}_h \quad (4.13)$$

where  $\mathbf{D}_h$  is the methane hydrate constitutive matrix.

It is assumed that the material damage and the subsequent changes in  $L$  can be related to the variation in the energy (per unit of volume) stored in the hydrates (Carol et al. 2001). This energy can be defined as the elastic secant energy that would be recovered upon unloading; which, e.g. for triaxial conditions, can be written as:

$$u_h = \frac{1}{2} (p_h \varepsilon_h^v + q_h \varepsilon_h^q) \quad (4.14)$$

The hydrate damage locus is defined by a threshold value ' $r_0$ ' of the secant elastic energy that can be represented by an ellipse in the ' $p_h$ - $q_h$ ' space. The hydrate stiffness remains constant when the stresses are inside that ellipse. Loading damage takes place when the changes in the stress state is such that the secant elastic energy reaches  $r_0$ .

During damage, the associated variable  $L$  increases, inducing a reduction of the material stiffness. The damage evolution is determined by (Pinyol, 2007)

$$r_{(L)} = r_0 e^{\eta L} = u_h \quad (4.15)$$

The damage rate is controlled by  $r_l$ . The consistency condition is adopted for defining the evolution law for  $L$ . The following evolution law for the partition variable is adopted:

$$\chi = \chi_0 e^{\frac{L}{2}} \quad (4.16)$$

where  $\chi_0$  is an initial reference value assumed for the partition variable.

#### 4.4.4. Constitutive model for the sediment skeleton

The constitutive model for the soil skeleton is based on a modified *HISS* framework. The constitutive equation incorporates sub-loading concepts, as well as hardening and dilation enhancement mechanisms associated with the presence of hydrates in the sediments. The modified *HISS* model involves a single and continuous yield surface that can adopt different shapes depending on the selected parameters (Desai et al. 1986; 1989; 2000). The *HISS* yield surface ( $F$ ) is given by:

$$F = \frac{a}{M^2} q_{ss}^2 - 9\gamma \left[ (p'_{ss})^2 - (p'_{ss})^n p_c^{2-n} \right] \quad (4.17)$$

where  $a$  and  $\gamma$  are model constants;  $n$  is the parameter related to the transition from compressive to dilative behavior;  $p'_{ss}$  and  $q_{ss}$  are the mean effective and deviatoric stresses, respectively, both associated with the sediment skeleton;  $M$  is the slope of critical line in the  $q_{ss}$ - $p'_{ss}$  space; and  $p_c$  is the effective pre-consolidation pressure.

The mean effective stress ( $p'_{ss}$ ) and the elastic volumetric strains are related through the stress-dependent elastic sediment bulk modulus  $K'_{ss}$ :

$$K'_{ss} = \frac{v}{\kappa} p'_{ss} \quad (4.18)$$

where  $v$  is the specific volume; and  $\kappa$  is the slope of the unloading/reloading curve in the void ratio ( $e$ ) versus  $\log(p'_{ss})$  space. The sediment-skeleton shear modulus ( $G_{ss}$ ) relates the deviatoric elastic strains with the deviatoric stresses.

An isotropic strain hardening behavior in terms of the plastic volumetric deformation ( $\varepsilon^{vp}$ ) is adopted:

$$\frac{dp_c}{p_c} = \frac{v}{\lambda - \kappa} d\varepsilon^{vp} \quad (4.19)$$

where  $\lambda$  is the slope of the normal compression line in the  $e$ - $\log(p'_{ss})$  plane. It has assumed that the yield surface  $F$  and the plastic potential  $G$  coincide (i.e. associated plasticity). A non-associated flow rule can be easily incorporated if necessary.

$$d\boldsymbol{\varepsilon}^p = \Lambda \frac{\partial G}{\partial \boldsymbol{\sigma}'_{ss}} = \Lambda \frac{\partial F}{\partial \boldsymbol{\sigma}'_{ss}} \quad (4.20)$$

where  $\Lambda$  is the plastic multiplier and  $\boldsymbol{\sigma}'_{ss}$  is the effective Cauchy's stress tensor.

The isotropic expansion of the yield surface is controlled by the hardening parameter ' $p_d$ '. Based on (Uchida, 2012), the influence of hydrates in this law is considered as:

$$p_d = \alpha (\chi C_h)^\beta \quad (4.21)$$

where  $\alpha$  and  $\beta$  are constants that describe the degree of hydrate contribution to the hardening law. In all the analyses conducted in this work, a good agreement with the experimental data was obtained when  $\beta=1$ , therefore this parameter could be excluded from the formulation, however it was kept to provide more flexibility to model in case is necessary. Also, previous works adopted a similar expression for  $p_d$ . Note that the presence of hydrate is also accounted when modeling the soil skeleton because of the profound impact of hydrates on sediment matrix behavior. Equation (4.21) considers that once the hydrates fully dissociate, the behavior of the pure soil skeleton is recovered. The partition parameter  $\chi$  accounts for the effect of hydrate degradation on the preconsolidation pressure and it also provides a link between the damage law for the hydrates and the critical state model for the solid skeleton. The yield function (YF) incorporating the strength enhancement associated with the presence of methane hydrate can be expressed as:

$$F_b = \frac{a}{M^2} q_{ss}^2 - 9\gamma \left[ \left( p'_{ss} \right)^2 - \left( p'_{ss} \right)^n (p_c + p_d)^{2-n} \right] \quad (4.22)$$

where  $F_b$  corresponds to an external (limit) surface, called hereafter boundary yield surface. This surface coincide with  $F$  when the effect of hydrates on the sediment matrix vanishes because of hydrate dissociation or damage.

To account for inelastic deformations that may occur inside the bounding yield-surface sub-loading concepts are incorporated into the model formulation. This technique also smooths the transition between elastic and plastic states. Sub-loading concepts were used before with success to model the behavior of *HBS* (Lin et al., 2015; Uchida et al., 2012; 2016). The sub-loading yield surface and the yield surface  $F$ , are geometrically similar. The sub-loading surface passes through the present stress state and it evolves during yielding. More details about sub-loading concepts can be found elsewhere (e.g., Hashiguchi et al., 1977). The modified sub-loading yield surface ( $F_s$ ) incorporating  $p_d$  can be written as:

$$F_s = \frac{a}{M^2} q_{ss}^2 - 9\gamma \left\{ \left( p'_{ss} \right)^2 - \left( p'_{ss} \right)^n \left[ R(p_c + p_d) \right]^{2-n} \right\} \quad (4.23)$$

where  $R$  is the sub-loading surface ratio. As suggested by Hashiguchi et al.(1977), it is assumed that  $0 < R \leq 1$ . The changes in  $R$  are defined through the following evolution law (Uchida et al. 2012; 2016):

$$dR = -\eta \ln R |d\boldsymbol{\varepsilon}^p| \quad (4.24)$$

where  $|d\varepsilon^p|$  is the norm of the incremental plastic strain vector and  $\eta$  is a sub-loading parameter that controls the plastic deformations inside  $F_b$ . The term between brackets in Eq. (4.41) is called effective hardening parameter (i.e.,  $H=R(p_c+pd)$ ). The three yield surfaces considered in this model are presented schematically in Figure 4.13.

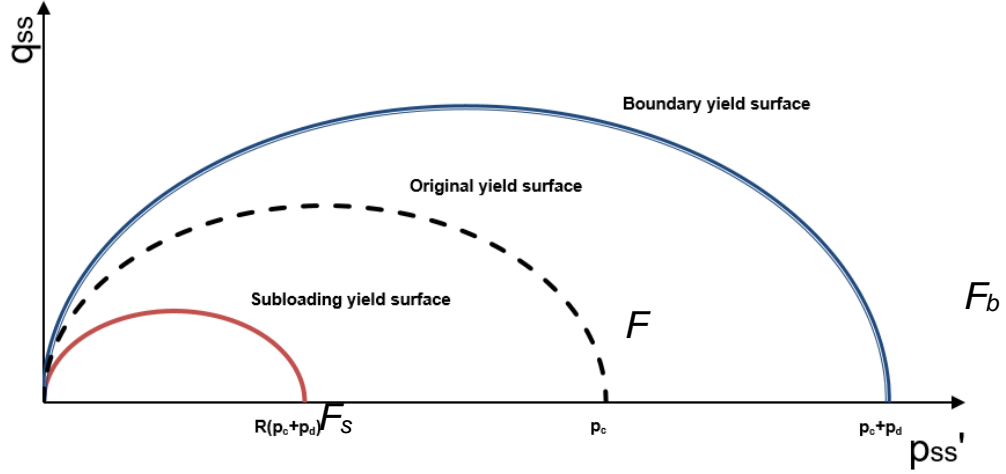


**Figure 4-6** Yield surfaces considered in the proposed model.

The consistency condition is enforced to ensure that the stress state remains on the (sub-loading) yield surface during yielding:

$$dF_s = \frac{\partial F_s}{\partial \sigma'_{ss}} d\sigma'_{ss} + \frac{\partial F_s}{\partial p_c} dp_c + \frac{\partial F_s}{\partial p_d} dp_d + \frac{\partial F_s}{\partial R} dR \quad (4.25)$$

After substituting the flow rule into the consistency condition (4.25), the plastic multiplier can be obtained as:

$$\Lambda = \frac{\left( \frac{\partial F_s}{\partial \sigma'_{ss}} \right)^T d\sigma'_{ss} + \frac{\partial F_s}{\partial p_d} \alpha \beta \chi (C_h)^{\beta-1} dC_h}{\frac{\partial F_s}{\partial p_c} \left( \frac{v}{\lambda - k} \right) p_c \frac{\partial F_s}{\partial p'_{ss}} + \frac{\partial F_s}{\partial R} (-\eta) \ln R \left| \frac{\partial F_s}{\partial \sigma'_{ss}} \right|} \quad (4.26)$$

The constitutive relationship for the sediment skeleton is obtained following the procedure suggested in (Pinyol, 2007).

$$d\sigma'_{ss} = \mathbf{D}_{ss} d\varepsilon + \mathbf{d}_{C_h} dC_h \quad (4.27)$$

where:

$$\mathbf{D}_{ss} = \left[ \begin{array}{c} \mathbf{D}_{ss}^e \frac{\partial F_s}{\partial \sigma'_{ss}} \left( \frac{\partial F_s}{\partial \sigma'_{ss}} \right)^T \mathbf{D}_{ss}^e \\ \left( \frac{\partial F_s}{\partial \sigma'_{ss}} \right)^T \mathbf{D}^e \frac{\partial F_s}{\partial \sigma'_{ss}} + \frac{\partial F_s}{\partial p_c} \left( \frac{v}{\lambda - k} \right) p_c \frac{\partial F_s}{\partial p'_{ss}} + \frac{\partial F_s}{\partial R} (-\eta) \ln R \left| \frac{\partial F_s}{\partial \sigma'_{ss}} \right| \end{array} \right] \quad (4.28)$$

$$\mathbf{d}_{C_h} = \left[ \begin{array}{c} \frac{\partial F_s}{\partial p_d} \alpha \beta \chi (C_h)^{\beta-1} \frac{\partial F_s}{\partial \boldsymbol{\sigma}'_{ss}} \\ \frac{\partial F_s}{\partial p_c} \left( \frac{v}{\lambda - k} \right) p_c \frac{\partial F_s}{\partial p'_{ss}} + \frac{\partial F_s}{\partial R} (-\eta) \ln R \left| \frac{\partial F_s}{\partial \boldsymbol{\sigma}'_{ss}} \right| \end{array} \right] \quad (4.29)$$

where  $\mathbf{D}^e_{ss}$  is the sediment skeleton elastic constitutive matrix, with a structure similar to Eq. (4.12) but  $K'_{ss}$  (i.e., Eq. (4.28)) and  $G_{ss}$  are used instead of  $K_{h0}$  and  $G_{h0}$ , respectively. Equation (4.27) shows the effect of hydrates on effective stress; which in turns affects the mechanical behavior of *HBS*. This equation also shows that the effect of hydrates vanishes once they dissociate and the true response of the sediment matrix is recovered.

#### 4.4.5. Final stress-strain relationships

To obtain the expressions relating the external effective stress  $\boldsymbol{\sigma}'$  with the two stress components, the principle of virtual work is advocated, which for triaxial conditions can be written as (Pinyol et al. 2007):

$$p' d\varepsilon^v + q d\varepsilon^q = p'_{ss} d\varepsilon^v + q_{ss} d\varepsilon^q + p_h C_h d\varepsilon_h^v + q_h C_h d\varepsilon_h^q \quad (4.30)$$

The following equation is obtained after replacing equations (4.8) and (4.9) into equation (4.30):

$$p' d\varepsilon^v + q d\varepsilon^q = p'_{ss} d\varepsilon^v + q_{ss} d\varepsilon^q + p_h C_h \frac{\chi}{1 + C_h \chi} d\varepsilon^v + q_h C_h \frac{\chi}{1 + C_h \chi} d\varepsilon^q \quad (4.31)$$

Considering that the equation above is valid for any external strain:

$$p' = p'_{ss} + \frac{C_h \chi}{1 + C_h \chi} p_h \quad (4.32)$$

$$q = q_{ss} + \frac{C_h \chi}{1 + C_h \chi} q_h \quad (4.33)$$

For a given  $C_h$  the redistribution of external stress between hydrates and soil skeleton is given by  $\chi$ . When  $\chi$  decreases (i.e., when degradation is taking place), the mechanical contribution associated with the hydrates is progressively transferred to the sediment matrix. A similar phenomenon takes place during dissociation, and once the hydrates fully dissociate, the external stresses are equal to the soil skeleton ones (i.e., as expected, there is no contribution from the hydrates).

Considering equations above, the external (global) effective stress can be expressed as follows.

$$d\boldsymbol{\sigma}' = d\boldsymbol{\sigma}'_{ss} + \frac{C_h \chi}{1 + C_h \chi} d\boldsymbol{\sigma}_h \quad (4.34)$$

Finally,  $d\boldsymbol{\sigma}'$  becomes:

$$d\boldsymbol{\sigma}' = \left[ \mathbf{D}_{ss} + \left( \frac{\chi}{1+C_h\chi} \right)^2 \mathbf{D}_h \right] d\boldsymbol{\varepsilon} + \left[ \mathbf{d}_{C_h} + \boldsymbol{\sigma}_h \left( \frac{\chi}{1+C_h\chi} - C_h \left( \frac{\chi}{1+C_h\chi} \right)^2 \right) \right] dC_h \quad (4.35)$$

The constitutive equations described above provide the relationships between the external stresses in terms of hydrate and soil matrix stresses. Eq. (4.34) in particular expresses the changes in external effective stresses, when changes in total strains and hydrate concentration take place. Note that  $C_h$  is acting as a ‘pseudo-strain’ (i.e. Eq. 4.53), in the sense that changes in hydrate concentration also induce changes in effective stress.

#### 4.4.6. Model Application

The performance of the model presented above was compared against available (recently published) experimental data involving a variety of conditions, from tests at constant  $S_h$ , to experiments involving hydrate dissociation at constant stresses.

The same parameters for the hydrate were assumed in all the cases analyzed in the following sections. For example,  $K_h$ ,  $G_h$  can be considered as material constants for hydrates; which can be obtained from the literature (e.g. Miranda and Matsuoka, 2008). As for the model related to the sediment skeleton, an ellipse (as in the *MCC* model) was adopted initially in all the cases. However, when the response of the suggested approach based on the *MCCM* yield surface was not satisfactory, its shape was slightly modified to improve the model performance. More details about the determination of the model parameters are provided below in each one of the analyzed cases. It is also worth mentioning that the main aim of the modeling was not to exactly reproduce the experimental behavior, but to check whether or not the suggested approach was able to capture the main features of *HBS* behavior observed in these experiments.

The equations presented above can be integrated numerically as suggested in Pinyol et al. (2007). The stress integration method proposed by Sloan et al. (1987) was adapted for the specific characteristics of this model (Gai and Sánchez 2017). All the analyses presented in this study correspond to the ‘point integration level’ type. For the modeling of the tests loaded at constant hydrate concentration (i.e. cases below in Case 1 to 3 and 5),  $dC_h$  was kept constant, changes in  $d\boldsymbol{\varepsilon}$  were introduced by steps and  $d\boldsymbol{\sigma}'$  was updated correspondingly (see Eq. (4.35)). While for those cases in which hydrate dissociation was induced at constant effective stress (i.e. cases below in Case 4 and 6),  $d\boldsymbol{\sigma}'$  was hold constant,  $dC_h$  was changed by steps and Equation (4.35) was solved in terms of  $d\boldsymbol{\varepsilon}$ . All the experiments analyzed in this research were conducted under drained conditions.

*Case1. Effect of hydrate saturation on HBS behavior.* Hyodo et al. (2013) reported triaxial compression tests on synthetic *HBS* samples conducted at four constant hydrate saturations (i.e.  $S_h=0$ ; 24.2; 35.1; and 53.1%). All the samples were prepared at a similar porosity (i.e.,  $\phi \sim 40\%$ ). The effective confining pressure for all the tests was 5 MPa. The samples were isotopically consolidated first and then subjected to shearing. The main test conditions related to this experimental study are listed in Table 4.1.

**Table 4-1:** Test conditions for triaxial compression tests studied in Case1

Effective confining pressure (MPa)	Porosity (%)	$S_h$ (%)
5	39.4	0
	39.6	24.2
	39.2	35.1
	40.1	53.1

The model parameters were determined using back-analysis based on two tests, the one involving sediments without hydrates (i.e.,  $S_h=0$ ) and the test related to the highest hydrate saturation (i.e.,  $S_h\sim 53.1\%$ ). Then, this model (without modifying the parameters adopted before) was used to predict the behavior of the samples with  $S_h\sim 24.2\%$  and  $S_h\sim 35.1\%$ . Table 4.2 lists the parameters adopted in the numerical simulations. Figures 4.6&b show the comparisons between experimental and model results for the different hydrate saturations in terms of deviatoric stress and volumetric strains versus axial strains. The specimen corresponding to hydrate saturation equal to 53.1% presents a (slight) stress-softening (post-peak) behavior and a dilatant response; while all the other samples exhibits a predominant compression behavior. The relatively high confining pressure at which these tests were performed (i.e.,  $\sigma'_c=5$  MPa) could be one reason for the predominant hardening behavior with positive volumetric strains observed in the experiments. In all the tests the initial stiffness and shear strength increase with  $S_h$ . The model was able to match very satisfactorily the stress-strain curves for all the experiments under study, i.e. the ones used for calibration and also the others two prediction tests. The agreement between tests and models results in terms of volumetric behavior is also excellent (Fig. 4.7b).

**Table 4-2:** Soil parameters adopted in the modeling of HBS in Case1

Properties	Test $S_h=0$	Test $S_h=24.2\%$	Test $S_h=35.1\%$	Test $S_h=53.1\%$
$M$	1.30	1.30	1.30	1.30
$\lambda$	0.16	0.16	0.16	0.16
$\kappa$	0.004	0.004	0.004	0.004
$p_c$ (MPa)	10.0	10.0	10.0	10.0
$a$	3	3	3	3
$n$	1	1	1	1
$\gamma$	-1/9	-1/9	-1/9	-1/9
$C_h$ (initial)	0	0.096	0.138	0.213
$\alpha$	-	32	32	32
$\beta$	-	1.0	1.0	1.0
$r_l$	-	4.1	4.1	4.1
$r_o$	-	1e-5	1e-5	1e-5
$\eta$	42	42	42	42
$\chi_0$	-	1	1	1
$K_h$ (MPa)	-	9600	9600	9600
$G_h$ (MPa)	-	4300	4300	4300

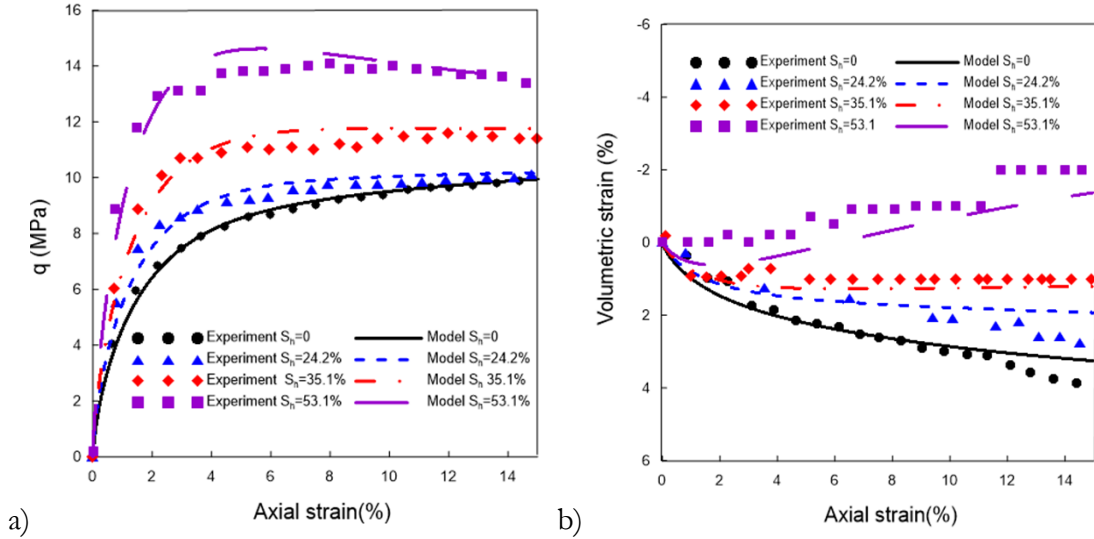


**Figure 4-7** Comparisons between model and experimental results for synthetic samples of *HBS* prepared at different hydrate saturations: a) stress-strain behavior; b) volumetric response. Experimental data adapted from (Hyodo, 2013).

*Case2. Effect of hydrate morphology on HBS behavior.* Triaxial compression tests based on synthetic methane hydrate samples were performed by Masui (2005). Some specimens were prepared using the ice-seed method that generally produces gas hydrates with dominant pore-filling pore-habit (Masui et al. 2005). For other samples, the partial water saturation method was adopted, which generally leads to *HBS* where the cementing morphology type is dominant. Toyoura sand was adopted for all the tests. These specimens were tested in a triaxial device capable of reproducing fluid pressures equivalent to conditions of around 800 meters under sea level. The tests were conducted at a  $\sigma'_c=1.0$  MPa. No hydrate dissociation was induced during the experiments. The three experiments presented in Figure 4.2b carried out by Masui et al. (2005) were selected to study the capability of the model to reproduce the effect of hydrate morphology on the mechanical behavior of *HBS*. The main parameters adopted for the numerical analysis are listed in Table 4.3. Masui et al. (2008) reported porosity values between 37.7% and 42.4%. The hydrate saturation was very similar in both tests (i.e.,  $S_h \sim 0.41$ ).

Figure 4.15 shows the comparisons between experimental results and model outputs in terms of stress-strain and volumetric behaviors. The model was able to capture very satisfactorily the different features of *HBS* behavior (i.e. increase of stiffness, strength and dilation in the samples with hydrates) observed in these tests involving different hydrate morphologies and pure sediment. The model was able to satisfactorily capture the more marked mechanical effect that the cementing form has on *HBS* behavior when compared against the pore-filling morphology type. One issue to note is that the model under-estimate the sediment dilatancy and softening for the cementing case. Note that the same *HISS* model parameters were adopted for the sediment in the three cases since they do not depend on the hydrates pore-habit. As discussed before, it was assumed that the initial strain-partition parameter  $\chi_o$  (i.e., Eq. (4.34)) depends on hydrate morphology. The value of the cementing sample was adopted higher (i.e.,  $\chi_o=1.5$ ) than the pore-filling one (i.e.,  $\chi_o=1.0$ )

**Table 4-3:** Soil parameters adopted in the modeling of Cases in Case2

Properties	Pure sand	Pore-filling	Cementing
$M$	1.17	1.17	1.17
$\lambda$	0.18	0.18	0.18
$\kappa$	0.006	0.006	0.006
$p_c$ (MPa)	12	12	12
$a$	3	3	3
$n$	1.02	1.02	1.02
$\gamma$	-1/9	-1/9	-1/9
$C_h$ (initial)	0	0.16	0.16
$\alpha$	-	35	70
$\beta$	-	1.0	1.0
$r_1$	-	1.1	1.05
$r_0$	-	7e-5	1e-4
$\eta$	15	15	15
$\chi_0$	0	1.0	1.5
$K_h$ (MPa)	-	9600	9600
$G_h$ (Mpa)	-	4300	4300

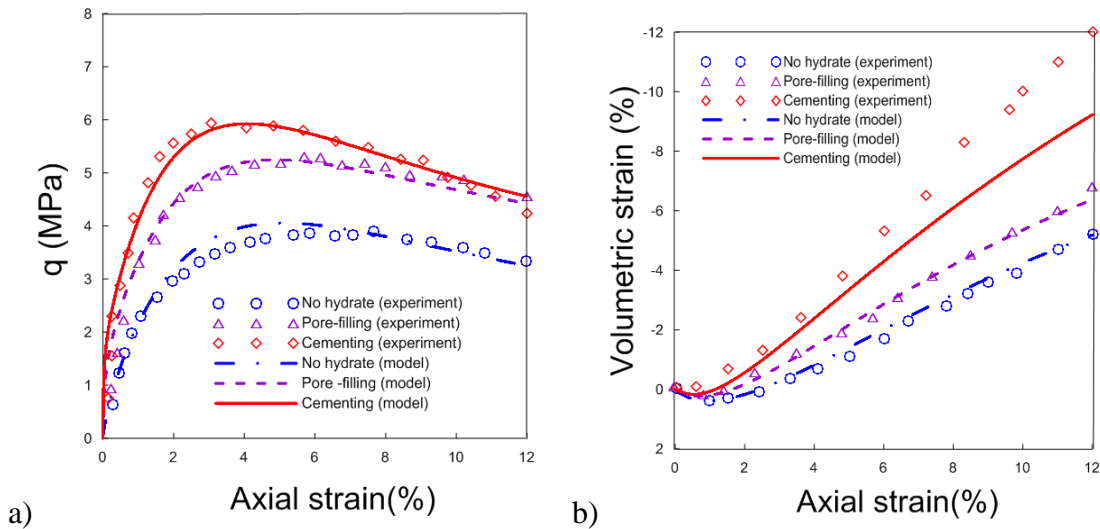


**Figure 4-8** Comparisons between model and experimental results for synthetic Toyoura sand samples with different hydrates pore habits: a) stress strain behavior; b) volumetric response. Experimental data adapted from (Masui, 2005)

*Case3. Modeling the behavior of natural HBS samples.* Synthetic methane hydrate specimens were modeled in the two previous Cases, in this one, experiments involving natural hydrate samples conducted by Yoneda et al. (2015) are studied. Core samples were retrieved from the Eastern Nankai Trough by means of the pressure core analysis and transfer system. The natural sediments were maintained very close to the in-situ condition (Santamarina et al. 2012). Table 4.4 lists the main soil properties and other information associated with these experiments. Specimens identified as core#7 and core#9, with  $S_h \sim 38\%$  and  $S_h \sim 79\%$ , respectively, were tested under triaxial drained conditions.

As explained in Yoneda et al. (2015), the manipulation of core#9 and core#7 induced changes in the material. Core#7 was treated using liquid nitrogen ( $LN_2$ ) core method,

while core#9 was treated using CH<sub>4</sub> purge LN<sub>2</sub> core method. In these two methods, the specimens were exposed to the atmospheric pressure, which might induce hydrate dissociation. Yoneda et al. (2015) suggested that the plausible in-situ hydrate saturation for core#7 could be between 65% and 90%, but because of the sample handling, the hydrate saturation decreased up to ~38% (i.e. at test condition). Furthermore, some damage of the core was observed in the *CT* images which means that the soil structure was affected by the handling method. As for core#9, the in-situ hydrate saturation was between 70% and 95%. It was also estimated that the hydrate saturation at test condition was around 79%. Furthermore, no damage was observed in this specimen which implies that when core#9 was tested at conditions similar to the field ones. Based on the comments above these two cores correspond to different materials and therefore slightly different parameters were assumed in the simulation of these two cases. However, the same critical state parameters were assumed for both cases because they are not related to the hydrate morphology. Table 4.5 lists the adopted parameters.

**Table 4-4:** In situ conditions, soil properties, and testing conditions for tests presented in Case3

Test name	Host type	Overburden (m)	$\sigma'_3$ (MPa)	Water content (%)	$\phi$ (%)	$S_h$ (%)
#7	Silty sand	279.3	1.5	26.4	44.1	38
#9	Silty sand	294.2	1.6	22.7	39.4	79

Figure 4.9 presents the experimental and numerical results for the stress-strain behavior and volumetric response of the natural *HBS* core samples discussed above. Core#9 exhibits a very noticeable peak strength, with a significant enhancement in stiffness and dilatancy, which can be associated with the higher hydrate saturation of this sample respect to core#7. As shown in Figure 4.9, the model provides enough flexibility to satisfactorily reproduce the mechanical behavior of two natural samples from Nankai Trough. The performance of the model is very satisfactory but for some slight deviations in terms of volumetric strain.

**Table 4-5:** Soil parameters adopted in the modeling of *HBS* specimens in Case3

Properties	Core 7	Core 9
$M$	1.26	1.26
$\lambda$	0.16	0.16
$\kappa$	0.014	0.014
$p_c$ (MPa)	12	12
$a$	3	3
$n$	0.98	0.98
$\gamma$	-0.14	-0.14
$C_h$ (initial)	0.1675	0.311
$\alpha$	6	21
$\beta$	1	1
$r_l$	1.1	1.3
$r_o$	1e-5	1.25e-4
$\eta$	3	48
$\chi_0$	1	1
$K_h$ (MPa)	9600	9600
$G_h$ (MPa)	4300	4300

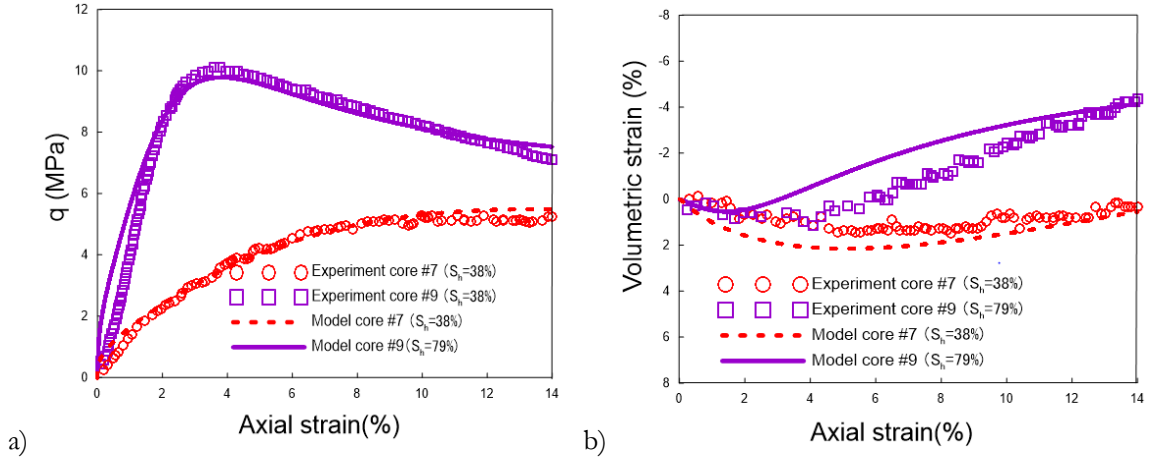


**Figure 4-9** Model and experimental results for triaxial tests on natural samples: a) stress strain behavior; b) volumetric response. Experimental data adapted from (Yoneda et al. 2015)

*Case4. Effect of hydrate dissociation on HBS behavior under triaxial conditions.* The tests conducted by Hyodo et al. (2014) were selected to study the effect of hydrate dissociation under triaxial conditions. The main information about the samples and tests details were introduced before. Table 4.6 lists the main tests conditions related to these experiments.

**Table 4-6:** Test conditions of methane hydrate dissociation tests. Case4.

Consolidation condition	$\sigma'_c$ (MPa)	$S_h$ (%)	Porosity (%)	Test N°	Remarks
Isotropic	5	48.7	40.4	1	Dissociation→Shear
Isotropic	5	47.4	39.9	2	Shear1%→Dissociation→Shear
Isotropic	5	47.9	39.8	3	Shear5%→Dissociation→Shear

These tests provide very useful information about the effect of hydrate dissociation at two stages of shearing. When the dissociation was induced at  $\varepsilon_a=1\%$ , the stress conditions were quite far from the failure of the dissociated sediment (i.e., the deviatoric stress of this sample at  $\varepsilon_a=1\%$  was 8.4 MPa, while the strength at failure of the already dissociated sample was around 10 MPa). However, when the hydrate dissociation started at  $\varepsilon_a=5\%$  the deviatoric stress (i.e.  $q \approx 12$  MPa) was higher than the strength of the dissociated sediment and it was difficult to maintain the constant stress condition during dissociation. The sample failed and the deviatoric stress reduced tending to the strength of the dissociated sample (i.e.,  $q \approx 10$  MPa). These were quite complex experiments that have been simulated following the reported test protocols (Hyodo et al., 2014).

The modeling of these experiments was approached as follows: i) first the test related to the already dissociated sediment was simulated (using typical reported parameters for this type of material, i.e. sand); then, ii) the test related to the dissociation at  $\varepsilon_a=1\%$  was studied (and used to adjust the model parameters for the *HBS* case); and finally, iii) the test involving hydrate dissociation at an initial  $\varepsilon_a=5\%$  was simulated to validate the proposed model under these particular conditions. Table 4.7 lists the main parameters selected for the modeling. Figures 4.10 present the comparisons between experiment and model results for the three cases discussed above.

As for the already dissociated sample (Fig. 4.10a), quite good agreements were obtained in terms of deviatoric stress and volumetric behavior. In particular, the model manages to replicate well the maximum stress, but slightly under-predicts the maximum volumetric strain. Figure 4.10b presents the experimental and numerical results related to the sample at which dissociation was induced at  $\varepsilon_a=1\%$ . In addition to the external deviatoric stresses (i.e., the one to be compared against the experimental observations), the mechanical contributions of the hydrate and sediment skeleton are computed by the model and included in this figure as well.

**Table 4-7:** Parameters adopted in the modeling of HBS specimens. Case4.

Properties	Shear after dissociation	Dissociation induced at $\varepsilon_a=1\%$	Dissociation induced at $\varepsilon_a=5\%$
$M$	1.17	1.17	1.17
$\lambda$	0.12	0.12	0.12
$\kappa$	0.002	0.002	0.002
$p_c$ (MPa)	11.5	11.5	11.5
$a$	3	3	3
$n$	1	1	1
$\gamma$	-1/9	-1/9	-1/9
$C_h$ (initial)	0	0.195	0.195
$\alpha$	-	16	16
$\beta$	-	1.0	1.0
$r_l$	-	2.9	2.9
$r_o$	-	1e-5	1e-5
$\eta$	-	35	35
$\chi_0$	-	3	3
$K_h$ (MPa)	9600	9600	9600
$G_h$ (MPa)	4300	4300	4300

Initially, both hydrate and sediment contributed progressively to the mechanical stability of the specimen. Afterwards, during hydrate dissociation, the mechanical contribution arising from the hydrate was progressively decreasing and transferred to the soil skeleton, leading to an increase in the sediment stress during this step at constant global stress. The external stress is solely supported by the soil skeleton at the end of the dissociation process. Shearing continued after full dissociation and the deviatoric stress increased until reaching the strength of the already dissociated sediment.

The model captures very satisfactorily the main trends observed in these experiments, particularly: the degradation in stiffness during the initial loading stage, the (average) deviatoric stress during dissociation, and the maximum final deviatoric stress after dissociation. However, the experimental deviatoric stress at  $\varepsilon_a=1\%$  is slightly higher than the one computed by the model, and the axial strains observed during dissociation are larger than the simulated ones. Note that in any case, the  $\varepsilon^v$  during dissociation are well reproduced by the model. The model slightly under-predicts  $\varepsilon^v$  at advanced stages of the experiment (i.e.,  $\varepsilon_a>12\%$ ). At that final stages of shearing, the three yield surfaces considered in this model coincided in one, and the stress state is on the summit of that ellipse. Therefore, according to the model, there are not changes in plastic volumetric strains (i.e.,  $d\varepsilon^{vp}=0$ ) and  $\varepsilon^{vp}$  remains almost constant. In this way the model simulates the material failure (i.e., continuous deformations at constant deviatoric stress).

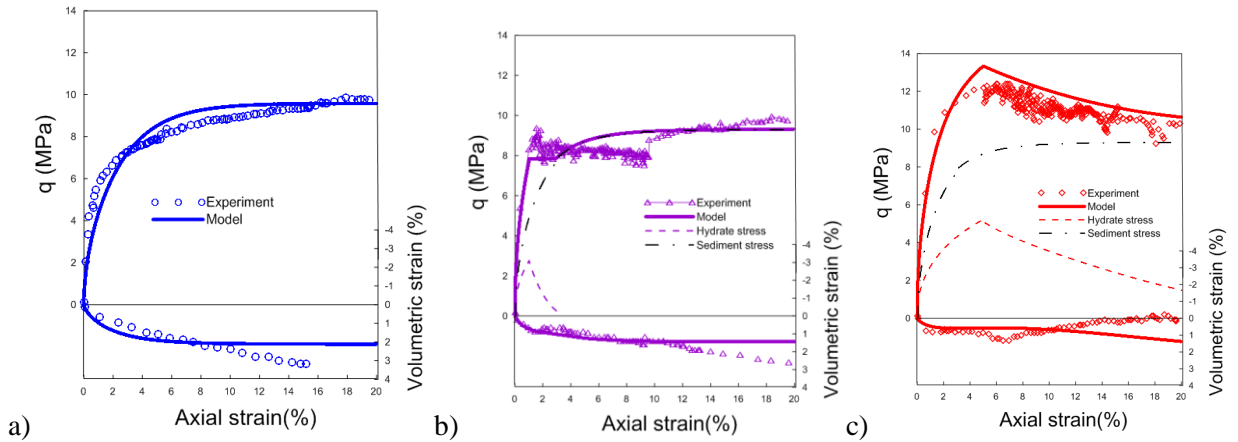


**Figure 4-10** Experimental and modeling results for drained triaxial tests: a) already dissociated sediment, b) dissociation induced at  $\varepsilon_a=1\%$ ; and c) dissociation induced at  $\varepsilon_a=5\%$ . Experimental data adapted from (Hyodo, 2014)

Once the model parameters were calibrated using the two previous cases, the ability of the constitutive equation to predict the *HBS* behavior under dissociation was checked against the third test. Fig. 4.10c presents the comparisons between the experimental results and the model predictions for the case in which the hydrate was dissociated at  $\varepsilon_a=5\%$ . The model results are also very satisfactory in this case, the main tendencies observed in this experiment are well captured by the model. However, the peak deviatoric stress is slightly over-predicted by the model. There are also some differences between the model predictions and the reported experimental data in terms of volumetric behavior. Surprisingly, it was observed that there was not volume change at the end of this test, because an apparent dilation during dissociation compensate the initial positive volumetric strains. This final dilation in the experimental result seems strange, the tendency during dissociation at high stresses under drained conditions should be to contract, because the sediment structure tend to a more compact state as the hydrates disappear. The positive  $\varepsilon^v$  predicted by the model during dissociation are related to the volumetric compression plastic strains induced by the collapse of the sediment structure during hydrate dissociation (as shown in Fig. 4.3.b, and illustrated in Fig. 4.4.b). This structure-collapse behavior is explained in more detail in Case6.

Hyodo et al. (2014) experienced some difficulties to maintain the deviatoric stress constant during dissociation in this test. Because of the progressive degradation of the *HBS* structure during hydrate dissociation, it was impossible to hold the (high) deviatoric stress applied just before dissociation (i.e., at  $\varepsilon_a=5\%$ ). The mechanical contribution from the hydrate (dash line) was gradually transferred to the sediment skeleton during dissociation, and the global deviatoric stress decreased progressively until reaching the maximum strength associated with the already dissociated sediment. At the end of shearing phase, the model predicts that hydrates still contribute to the mechanical behavior of the sample, this result is supported with the reported experimental data indicating that not all the hydrates dissociated at the final axial strain (i.e.,  $\varepsilon_a=20\%$ ).

Figure 4.11 shows additional information about this modeling. Figure 4.11a presents the  $q$ - $\varepsilon_a$  plot extended until full dissociation. During dissociation the bearing capacity of the hydrates decreased and the stress were gradually transferred to the sediment. The model

predicts that at advanced stages of shearing and hydrate dissociation all the external stresses are supported by the sediment skeleton only. The effective hardening parameter ( $H=R(p_c+p_d)$ ) always increased (Fig. 4.19b). This implies that  $F_s$  kept expanding during the whole test. The variable  $R$  always increased during the simulation as well (Fig. 4.11b). The increase in  $H$  (i.e. hardening of the sediment skeleton) observed at advanced stages of the experiment was induced by the volumetric-collapse-compression strains discussed above; which compensated the decrease of  $p_d$  during hydrate dissociation. Figure 4.11c presents the three initial yield surfaces (i.e.,  $F$ ,  $F_s$ , and  $F_b$ ) considered in this model at the start of the test. Figure 4.11d presents these three yield surfaces at two different stages: i) at  $\varepsilon_a=15.3\%$ , (when the sub-loading yield surface reached the boundary one,  $F$  is still inside  $F_b=F_s$ , because  $p_d$  did not vanish totally at this stage); and ii) at the end of the test, when the three yield surfaces coincided in one.

The proposed model has not only reproduced and predicted satisfactorily the behavior observed in the experiments, but it has also provided an explanation to the main features and trends of  $HBS$  behavior observed during the tests. In the tests, the hydrate dissociation was induced by heating (Hyodo, 2014).

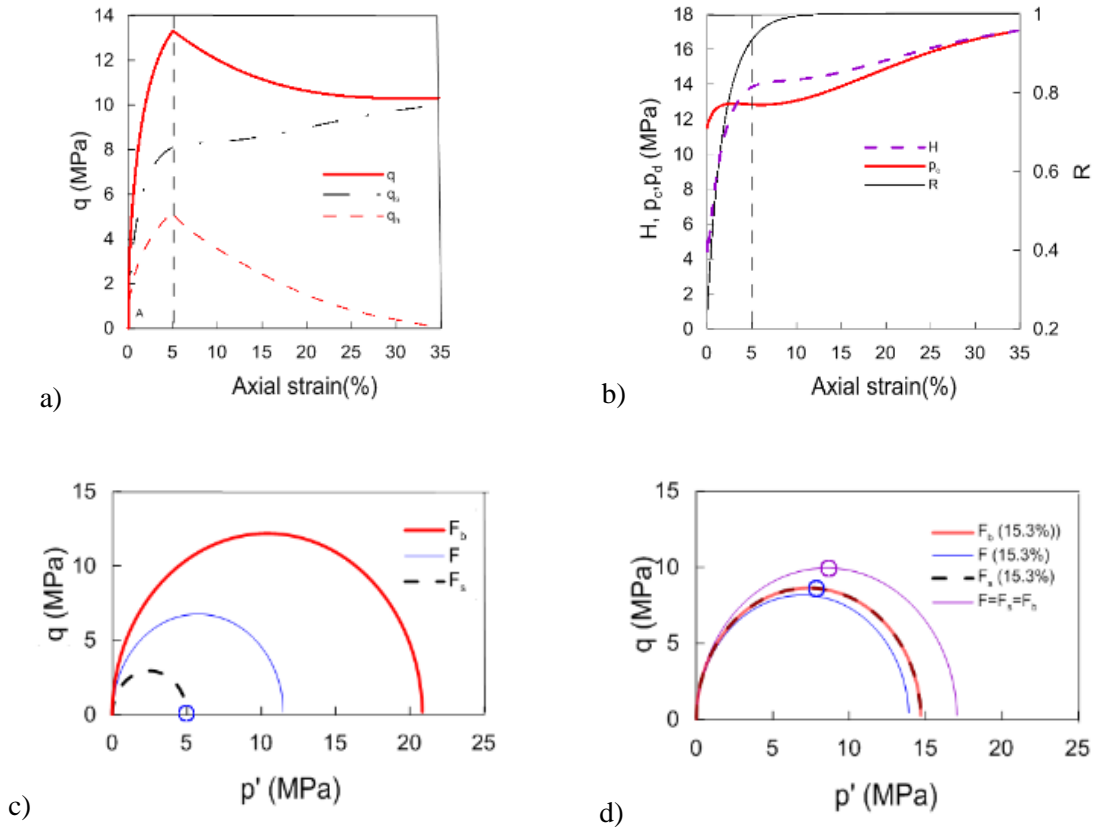


**Figure 4-11** Additional modeling information for the test in which dissociation was induced at  $\varepsilon_a=5\%$ : a) extended stress-strain behavior; b) hardening variables, c) yield surfaces at the beginning of the experiment; and d) yield surfaces at an intermediate stage of shearing ( $\varepsilon_a=15.3\%$ ) and at the end of test.

Thermal effects were not modeled in this analysis. This seems a reasonable assumption as the main focus here was on the influence of hydrates dissociation on material behavior. It also seems that temperature may have a small influence on the overall mechanical behavior of the specimen in this type of experiment. A more sophisticated analysis can certainly be done in the future incorporating thermal effects. The inclusion of temperature could also help to reproduce these experiments more closely.

*Case5. Effect of confining pressure and  $\chi_0$  on HBS response.* Once the ability of the model to reproduce the main tendencies observed in the experiments was checked, it could be of interest to see how other factors (not modeled in the cases before) have an influence on the behavior of *HBS*. It can also be relevant to explore further about how the different parameters and inelastic mechanisms proposed in this model work to simulate the main features of *HBS* behavior.

The first analysis in this section is relate to the effect of confinement on *HBS* behavior. The study is based on the *HBS* specimen presented in Case4. Tests at two additional cell pressures were simulated (i.e.,  $\sigma'_c=1$  MPa and  $\sigma'_c=3$  MPa) and dissociation was not induced in this modeling (i.e., shearing at constant  $S_h=48\%$ ). Table 4.8 lists the adopted model parameters. Figures 4.12a&b show that the confinement plays a critical role in the behavior *HBS*, as  $\sigma'_c$  decreases the peak strength decreases, the dilatancy increases and also the softening is more marked.

The plots in Figure 4.13 show more details about how the main variables of the model evolve for the test at  $\sigma'_c=1$  MPa. The hardening or softening behavior of the sediment is controlled by the effective hardening parameter  $H$ , which depends on  $R$ ,  $p_c$  and  $p_d$  through  $H=R(p_c+p_d)$ . It is assumed that the plastic deformations of the soil skeleton take place from the beginning of yielding.

This is in line with previous works in this area. (e.g., (Lin et al., 2015; Uchida et al., 2012; Uchida et al., 2016). Under this assumption, the model predicts plastic positive volumetric strains at the start of the test (i.e., between ‘A’ and ‘B’, Fig. 4.13a&b), because the stress state lies on the ‘wet side’ of  $F_s$  (Fig. 4.13c), therefore  $p_c$  increases

**Table 4-8:** Parameters adopted in Case4 - Effect of confining pressure

Properties	$\sigma'_3=1$ (MPa)	$\sigma'_3=3$ (MPa)	$\sigma'_3=5$ (MPa)
$M$	1.17	1.17	1.17
$\lambda$	0.12	0.12	0.12
$\kappa$	0.002	0.002	0.002
$p_c$ (MPa)	11.5	11.5	11.5
$a$	3	3	3
$n$	1	1	1
$\gamma$	-1/9	-1/9	-1/9
$C_h$ (initial)	0.195	0.195	0.195
$\alpha$	16	16	16
$\beta$	1.0	1.0	1.0
$r_l$	2.9	2.9	2.9
$r_o$	1e-5	1e-5	1e-5
$\eta$	35	35	35
$\chi_0$	3	3	3
$K_h$ (MPa)	9600	9600	9600
$G_h$ (MPa)	4300	4300	4300

After point ‘B’,  $p_c$  decreases because the stress state is on the ‘dry side’ of  $F_s$ . The sub-loading parameter  $R$  increases during the whole test (as it depends on the module of the total plastic strain). The hardening enhancement provides by the hydrates ( $p_d$ ) decreases through the tests due to progressive damage of the hydrates, up to reaching a fairly constant value. After the peak value ‘C’, the softening of the soil skeleton controls the global behavior of the HBS and the deviatoric stress tends to decrease substantially. The dilatant behavior of the skeleton also controls the global volumetric response. Figures 4.13c&d present the yield surfaces associated with this model at different stages.

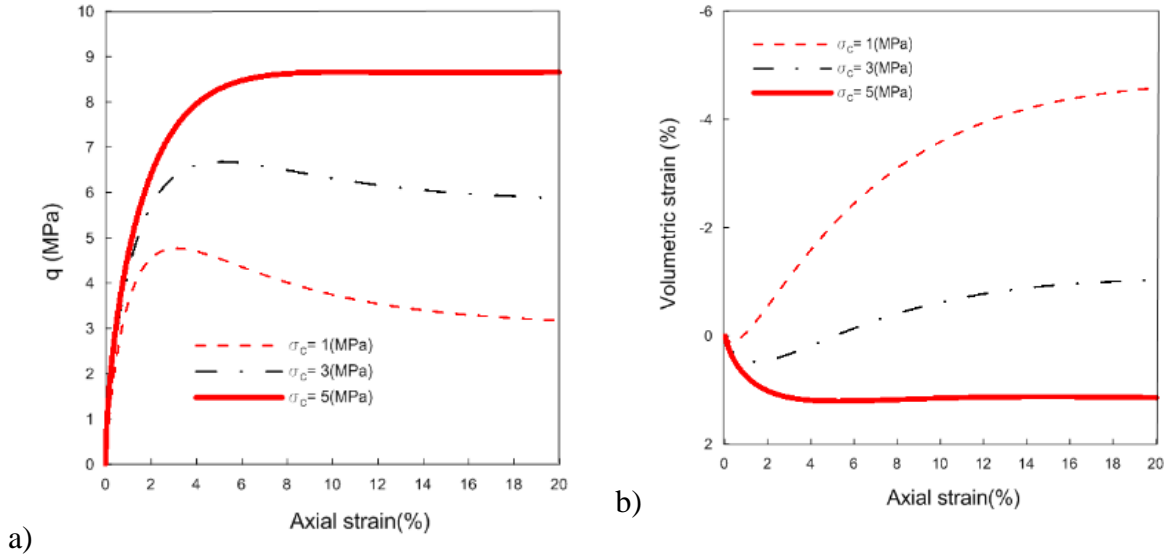


**Figure 4-12** Effect of confinement on HBS: a) stress strain behavior; b) volumetric response.

Finally, a study related to the effect of the partition parameter  $\chi_0$  on the model response is conducted. This factor controls the amount of the applied stress that is supported by the hydrate. The analysis discussed before with  $\sigma'_c=1$  MPa and  $\chi_0=3$  was adopted as the base case, and two additional analyses were performed with  $\chi_0=2$  and  $\chi_0=1$ . The reduction of this factor is related to a decrease of the bearing contribution of the hydrate and also with a reduction of the peak deviatoric strength (Fig. 4.14a). The volumetric behavior of the *HBS* is also affected by this parameter (Fig. 4.14b), a reduction of  $\chi_0$  is accompanied by an increase in the dilatancy. The adopted parameters are listed in Table 4.9

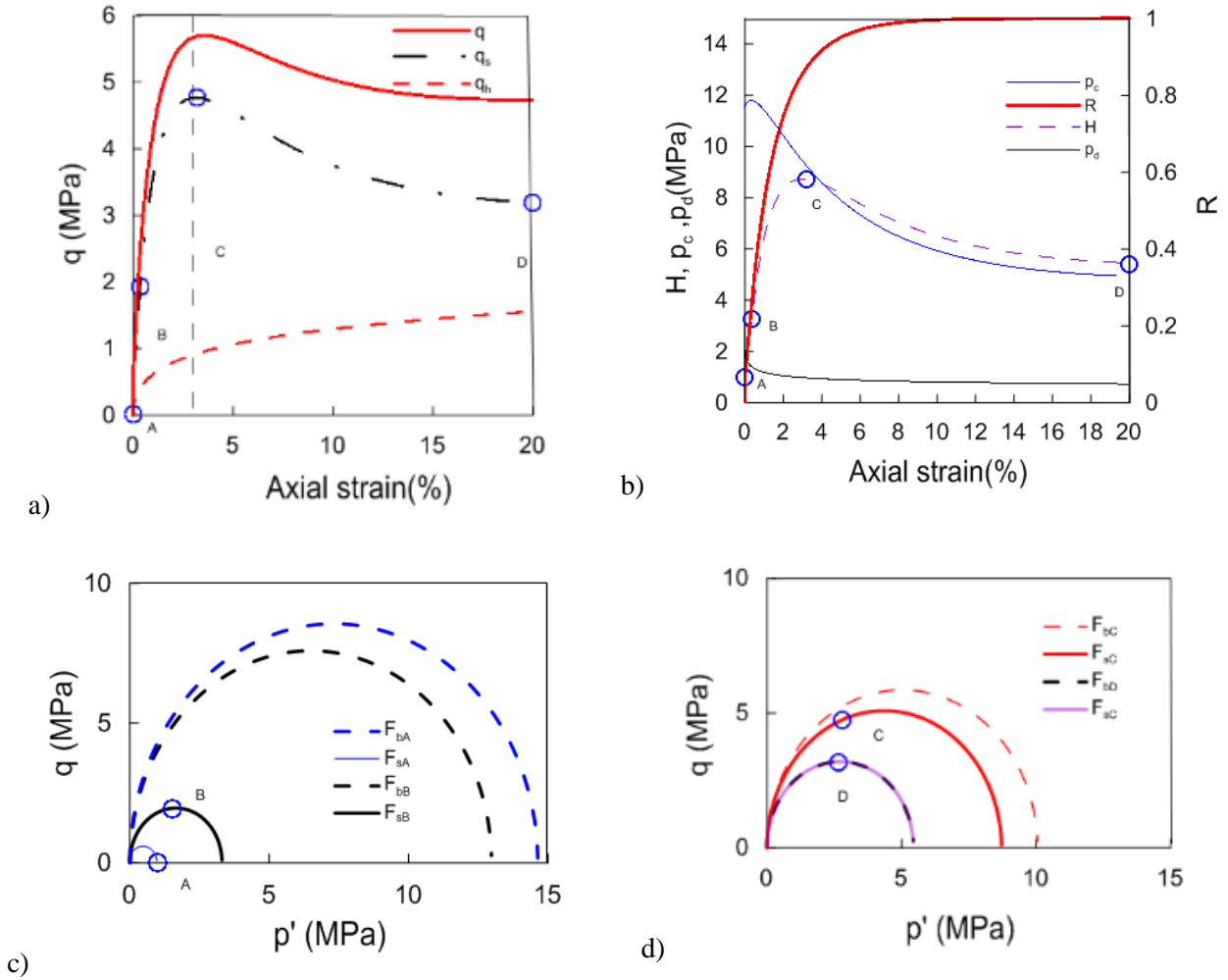


**Figure 4-13** Additional modeling information for the test in Fig 4.13 at  $\sigma'_c=1$  MPa: a) stress-strain behavior; b) hardening variables; c) yield surfaces at two initial stages of the experiment A&B; and d) yield surfaces at two final stages of shearing C&D.

**Table 4-9:** Parameters adopted in Section 4.5. Effect of parameters\*:  $\chi_0$

$\chi_0$	$r_0$	$r_1$
1	$1e^{-5}$	2.9
2	$1e^{-5}$	2.9
3	$1e^{-5}$	2.9

\*The parameters of the test in Table 4.9 with  $\sigma'_c=1$  (MPa) was used as the base case for the parameter sensitivity study.

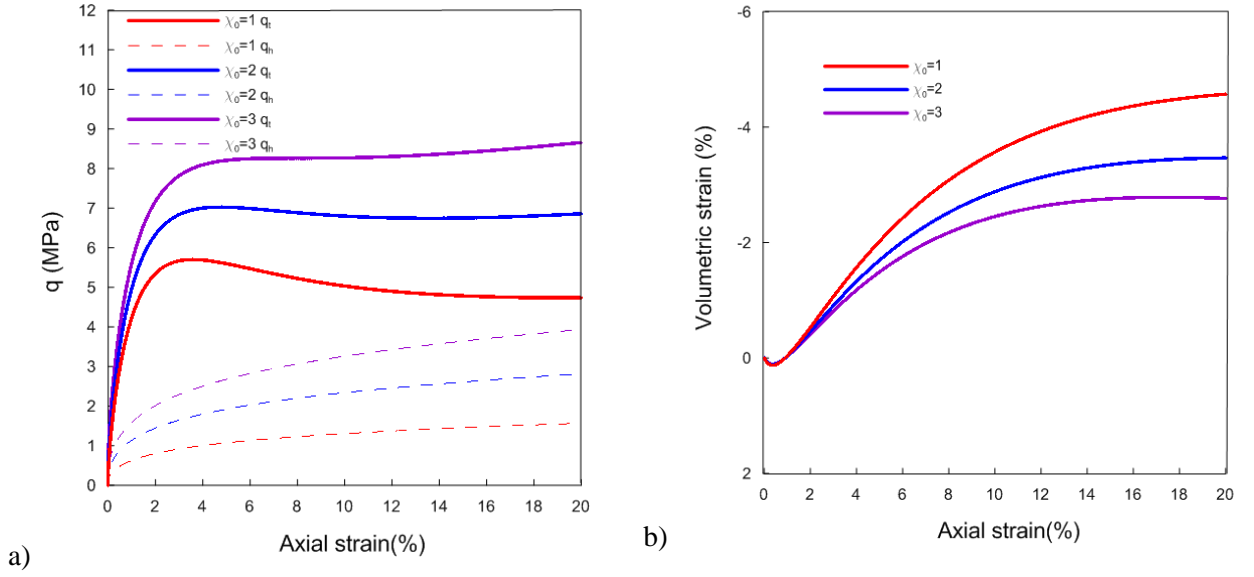


**Figure 4-14** Effect of  $\chi_0$  on HBS: a) stress-strain behavior, b) volumetric response.

*Case6. Effect of hydrate dissociation on HBS behavior under oedometric conditions.* The last set of experimental data studied in this work corresponds to two natural specimens gathered by means of the Pressure Core Characterization Tools (PCCTs) (Santamarina et al. 2012; 2015). The samples were loaded uniaxially with lateral confinement (i.e. oedometric conditions). General information about this research was presented before. The test presented in Fig. 4.3b plus another one with a lower hydrate saturation are simulated in this section. The parameters reported (Santamarina et al. 2015) for the dissociated sediment (i.e. a silty sand) were adopted in the simulations. The selected parameters are listed in Table 4.10. Tests and models outputs related to the specimen ‘core-8P’ (i.e. initial  $S_h=18\%$ ) are presented in Fig. 4.15a.

**Table 4-10:** Parameters adopted in the modeling of HBS specimens in Section 4.6

Properties	core 8P	core 10P
$M$	1.07	1.07
$\lambda$	0.605	0.12
$\kappa$	0.065	0.04
$p_c$ (MPa)	2.32	3.5
$a$	3	3
$n$	1	1
$\gamma$	-1/9	-1/9
$C_h$ (initial)	0.102	0.3605
$\alpha$	6	12.5
$\beta$	1.0	1.0
$r_l$	2.5	2.9
$r_o$	1e-6	2e-7
$\eta$	15	0.5
$\chi_0$	1	3
$K_h$ (MPa)	9600	9600
$G_h$ (MPa)	4300	4300

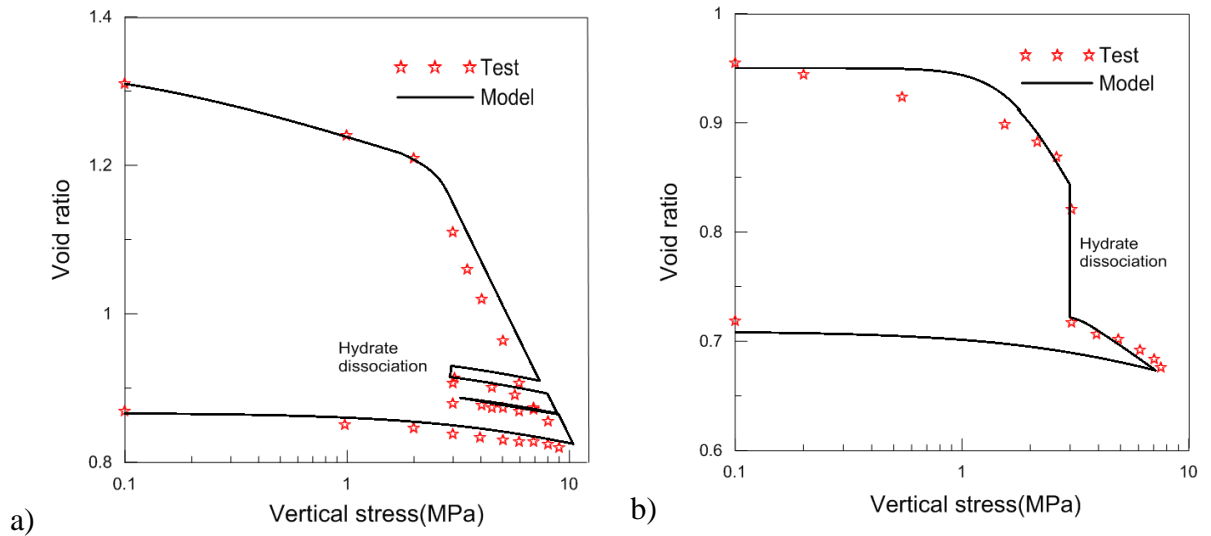


**Figure 4-15** Behavior during dissociation of natural *HBS* specimens under oedometric conditions: a) core 8P; and b) core 10P. Experimental data adapted from (Santamarina et al. 2015)

The *HBS* specimen was subjected to a monotonic increase in the vertical stress up to  $\sigma'_v=6$  MPa, followed by an unloading up to  $\sigma'_v=3$  MPa. Hydrate dissociation was induced in this over-consolidated sample followed by cycles of loading (with a maximum  $\sigma'_v=9$  MPa) and unloading of the already dissociated sediment. The experimental and numerical results associated with specimen ‘core-10P’ (i.e. initial  $S_h=74\%$ ) are presented in Figure 4.15b. In this case the effective vertical stress was increased until  $\sigma'_v=3$  MPa and hydrate dissociation was induced at this constant effective stress (under normally-consolidated conditions). Once the sample was fully dissociated, the vertical stress was increased until a maximum  $\sigma'_v=9$  MPa, followed by an unloading. Settlements were recorded in the both tests during all the loading stages.

The proposed framework was able to represent very satisfactorily the main tendencies observed in the experiments. The yield stress and unloading-reloading behavior are properly reproduced in both specimens. The model slightly over-predicts the initial stiffness of the core-10P. It is worth to highlight the model ability to reproduce the differences in volumetric strains observed during dissociation at constant stress in these two tests. The collapse compression behavior exhibited by core-8P was much less noticeable than the one observed in core-10P. This large volumetric strains can be associated with significant rearrangements of the *HBS* structure during hydrate dissociation. Some factors that can be considered to explain the differences between core-8p and core-10p in terms of the amount of the volumetric strain observed during dissociation are as follows: i) difference in hydrate saturation between the two samples (i.e. core-8P  $S_h=18\% \ll$  core-10P  $S_h=74\%$ ); ii) difference in the effective vertical stress at which hydrates dissociation was induced (i.e. core-8P  $\sigma'_v=3$  MPa  $\ll$  core-10P  $\sigma'_v=8$  MPa), therefore the effect of confinement on the re-accommodation of the sediments particles is less significant for core-8p; iii) dissociation in core-8P took place under over-consolidated conditions while in core-10p dissociation happened under normally-consolidated conditions; and iv) core-8p was previously loaded up to a very high

effective vertical stress (i.e.  $\sigma'_v=6\text{MPa}$ ) that degraded the bonding effects of the hydrate and induced important changes in the sediment structure previous to dissociation.

Figure 4.16a presents the evolution of  $\sigma'_v$  calculated by the model in the soil skeleton and hydrate, together with the external one for the case of core-8P. A significant portion of the stress increase is taken by the hydrate at the beginning of the experiment, i.e. path 'A-B'. Note that the hydrate saturation is very high in this case (i.e.,  $S_h=74\%$ ) and therefore an important bearing contribution from the hydrate can be anticipated. Upon dissociation at constant effective stress, the load is gradually transferred from the hydrate to the sediment skeleton and significant plastic volumetric strains are computed by the model, i.e. path 'B-C'. After full dissociation, the stresses are supported by the soil skeleton only, and the subsequent loading ('C-D') and unloading ('D-E') steps are controlled by the properties of the already dissociated sediment. Figure 4.16b shows the progressive reduction of the hardening enhancement effect (controlled by  $p_d$ ) during loading and it disappears during dissociation. The effective hardening parameter  $H$  increases during loading and remained unchanged upon unloading.

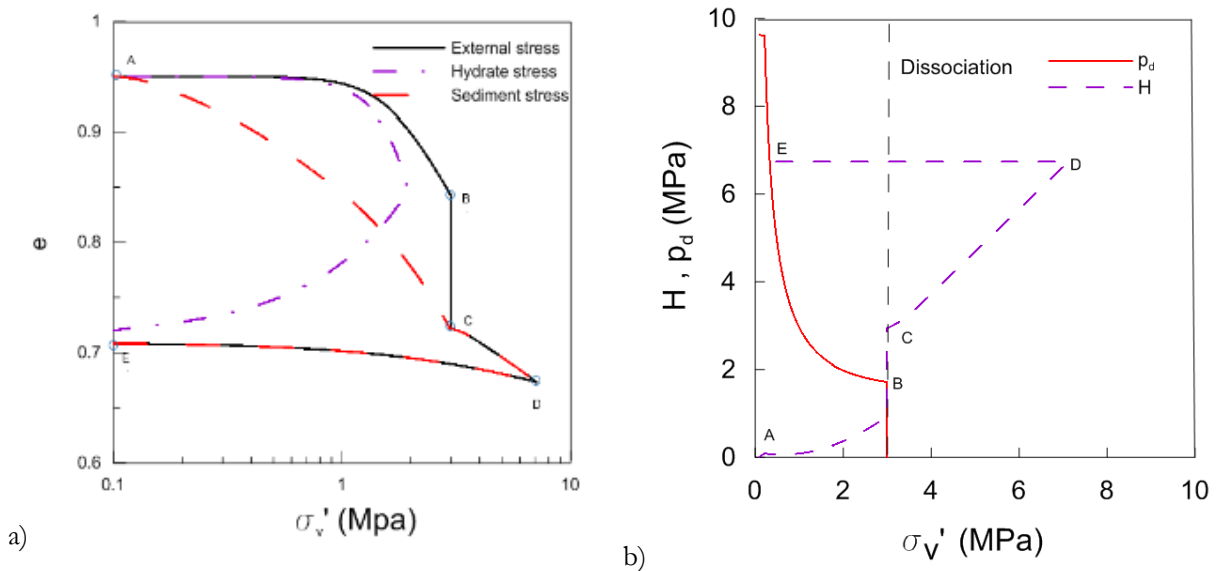


**Figure 4-16** Additional modeling information for the test related to core 10P: a) vertical stresses computed by the model during loading; b) hardening variables.

## 5. ANALYTICAL SOLUTIONS AND CODE VERIFICATION

Gas production from hydrate bearing sediments (*HBS*) is based on releasing the molecules of gas from lattice components of hydrate (which results in hydrate dissociation) with the aid of depressurization, heat and/or chemical stimulation. This is a complex phenomenon since hydrate dissociation comes with interrelated thermal, hydraulic, chemical and mechanical (*THCM*) processes. For example permeability coefficient will change as a result of the variation of temperature and hydrate saturation as well as volume variation. In addition mechanical strength of sediments depends on hydrate saturation while the effective stresses are affected by depressurization. Thus, coupled *THCM* analyses are inevitable for providing realistic simulation of gas production.

Estimates of the global accumulation vary between  $3 \times 10^{15} \text{ m}^3$  and  $10^{17} \text{ m}^3$  while the technically recoverable volume is on the order of  $3 \times 10^{14} \text{ m}^3$  (Sloan and Koh 2007; Boswell and Collett, 2011; Figure 5.1).

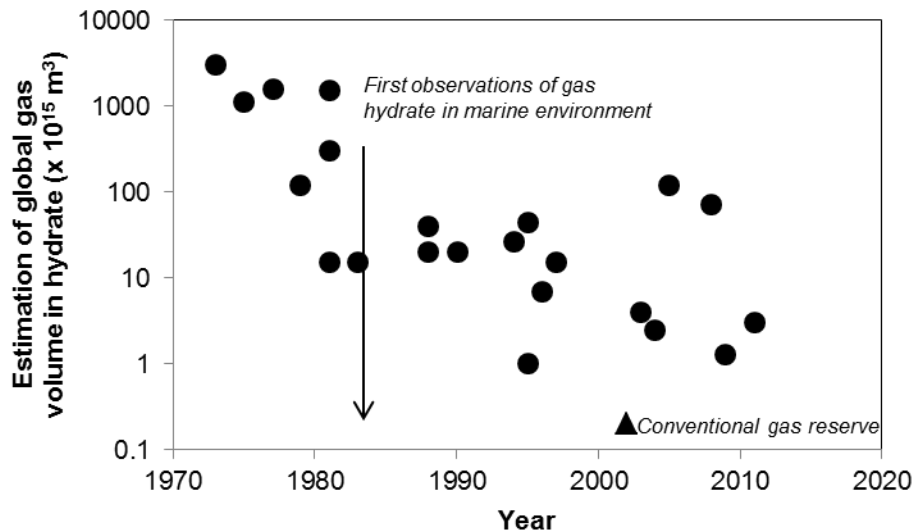


**Figure 5-1** Estimation of global gas on the state of hydrate gas. From Sloan and Koh (2007); Boswell and Collett (2011). Notice conventional gas reserves are still orders of magnitude less than the worst of hydrate gas estimations.

Gas reservoirs in hydrate bearing sediments can be classified as (Moridis and Collett 2003; Moridis et al. 2011 and Moridis and Sloan 2007):

- **Class 1:** high hydrate saturation layer on top of a layer with free gas and water (i.e. Bottom Simulating Reflector BSR).
- **Class 2:** similar to class 1 but there is no free gas beneath (only mobile water).
- **Class 3:** absence of free fluids underneath (semi confined aquifer).
- **Class 4:** low hydrate saturation (< 10%), and lack of confining stratum.

Class 1 reservoirs are most desirable because they are next to the phase boundary and a low energy input is required for dissociation. Class 4 is least desirable because they lack confinement and can lead to very low recovery efficiency.

Sandy deposits are currently preferred because of their high permeability and low compressibility. Reservoirs that are considered to be commercially feasible given today's state of the art are listed in Table 5.1.

**Table 5-1:** Selected reservoirs gas volume estimation.

<b>Location</b>	<b>Gas estimation [m<sup>3</sup>]</b>	<b>Reference</b>
Mallik (Canada)	3 10 <sup>9</sup> to 4 10 <sup>9</sup>	Moridis et al. 2002
Gulf of Mexico	6 10 <sup>14</sup>	BOEM report 2012
Mount Elbert (Alaska)	4 10 <sup>9</sup>	BOEM report 2012
Atlantic coast USA	6 10 <sup>14</sup>	BOEM report 2012
Pacific coast USA	2.3 10 <sup>14</sup>	BOEM report 2012
Ulleung Basin (Korea)	10 <sup>15</sup> to 10 <sup>18</sup>	Moridis et al. 2013
Nankai Trough(Japan)	5.6 10 <sup>11</sup>	Fujii et al 2013
ShenhuArea (China)	1.6 10 <sup>9</sup>	Wu et al. 2010
Krishna-Godavari basin (India)	9.8 10 <sup>8</sup> to 5.6 10 <sup>9</sup>	Shankar and Riedel 2011

Note: the amount of gas in place, technically and economically recoverable is still under discussion, and its values change with respect to authors and computation methods (Figure 1).

Methane gas can be produced from hydrate bearing sediments by (Moridis et al. 2008; Santamarina and Jang, 2009; Jang and Santamarina, 2011): (a) *depressurization*; (b) *thermal stimulation*; (c) *inhibitor's injection*, and (d) *CO<sub>2</sub>-CH<sub>4</sub> replacement*. Several field tests have taken place as summarized in Table 5.2.

**Table 5-2: Well tests summary in chronological order**

Name	Loc.	Year	Dur.	Type	Form.	S <sub>hyd</sub> [%]	Meas. k <sub>eff</sub> [mD]	Gas produced [m <sup>3</sup> ]	Affected radius [m]	Observ.	Reference
Mallik	Canada	2002	123.7 hrs	Thermal stim.	Sand	60 to 85	0.001 to 0.1	468	3	Formation solids were produced	Hancock et al. (2005); Moridis et al. (2011)
Mt. Elbert	Alaska	2007	Several tests up to 13 hrs each	Depress.	Sand	50 to 70	0.12 to 0.17	7 10 <sup>-4</sup>	0.05 to 0.15		Anderson et al (2008)
Mallik	Canada	2007	15hrs	Depress.	Sand	60 to 85	0.1 to 1	830	ND	Sand inflow causes operational problems	Dallimore et al. (2008)
		2008	6 days (139 hrs)	Depress.			ND	13000	ND		
Nankai Trough	Japan	2013	6 days	Depress.	Layd.	ND	ND	120000	ND	First offshore production	www.jogmec.go.jp

mD = 10<sup>-12</sup> m<sup>2</sup>

ND = No data provided

**Table 5-3:** Summary of selected parameters used in numerical simulations

Well rad. [m]	Dom. radius [m]	Hyd. thick. [m]	Initial press. [MPa]	Well press. [MPa]	Initial temp. [K]	Intrinsic Perm. [m <sup>2</sup> or mD]	Porosity [--]	Reference
0.1	10000	1	5.7	2.7	278.85	1 10 <sup>-15</sup> to 1 10 <sup>-12</sup> m <sup>2</sup>	0.30 to 0.60	Moridis and Sloan (2007)
ND	567.5	15	10	ND	286.65	1 10 <sup>-12</sup> m <sup>2</sup>	0.3	Moridis and Kowalsky (2006)
0.1	45	23	13	2.93	274.2	1 10 <sup>-15</sup> m <sup>2</sup>	0.3	Li et al (2012)
ND	ND	20, 16, 10	10.8, 9, 10.8	ND	285	2 10 <sup>-14</sup> m <sup>2</sup>	0.28	Moridis et al (2002)
0.1	450 to 1500	200	(Varies)	2.7	ND	1000 mD	0.3 to 0.64	Myshakin et al (2012)
0.1	100	10	11.5	3, 4 and 5	287.15	1 10 <sup>-14</sup> m <sup>2</sup>	0.38	Su et al (2012)
0.1	400	11.3	6.4	3	275.5	1 10 <sup>-12</sup> m <sup>2</sup>	0.4	Moridis et al (2011)
0.1	250	20	23	3	289	5 10 <sup>-13</sup> m <sup>2</sup> (**)	0.45 to 0.65	Moridis et al (2013)
ND	120	70, 100	13, 8.7, 13	3	287	1000 to 0.1 mD	0.3 to 0.4 (***)	Kurihara et al (2009)
0.1	45	22	13.8	0.2 Po	287	7.5 10 <sup>-14</sup> m <sup>2</sup>	0.41	Li et al (2010)
0.1	250	50	6.7 to 12.13	4	282 to 287	10 to 500 mD	0.4	Konno et al (2010)

(\*) computed from model proposed by Stone (1970)  $r_A = (S^*_A)^n$ ;  $S^*_A = (S_A - S_{irA})/(1-S_{irA})$ ;  $k_{rG} = (S^*_G)^n$ ;  $S^*_G = (S_G - S_{irG})/(1-S_{irG})$

(\*\*) estimated value

(\*\*\*) varies for clay, silt and sand

(\*\*\*\*) For the case of Class 3: 14° C and  $k_o = 500\text{mD}$

ND = no data provided

**Table 5.3:** Summary of selected parameters used in numerical simulations (cont.)

Hydrate saturation [--]	Relative permeability (*)			Observations	Reference
	Water	Gas	n		
	S <sub>irA</sub> [--]	S <sub>irG</sub> [--]	[--]		
0.02 to 0.1	4	0.2	0.02	Parametric study –Dissoc. pressure is computed by the software	Moridis and Sloan (2007)
0.7	3	0.25	0.02	Class 1 and 2 hydrate deposit studied	Moridis and Kowalsky (2006)
0.4	3.57	0.25	0.05	Simulating Qilian Mountain Permafrost - China	Li et al (2012)
0.8, 0.5, 0.8	4.2	0.2	0.05	Simulating different zones @ Mallik reservoir - Canada - vertical and horizontal wells	Moridis et al (2002)
0.05 to 0.80	3.16	0.18	0.02	Simulating layered sediments in Gulf of Mexico Walker Ridge 313 site	Myshakin et al (2012)
0.1, 0.2 and 0.3	5	0.3	0.03	Parametric study of Shenhu Area China	Su et al (2012)
0.65	4.2	0.2	0.02	Parametric study of Mount Albert, Alaska	Moridis et al (2011)
0.3 to 0.7	3.5	0.2	0.01	Simulating layered sediments Ulleung Basin, Korea	Moridis et al (2013)
0.1 to 0.96	ND	ND	ND	Layered system of sand, silt and clay of Nankai Trough, Japan	Kurihara et al (2009)
0.44	3.57	0.3	0.05	Sea of south of China, Shenhu	Li et al (2010)
0.6	k = k <sub>o</sub> (1-S <sub>h</sub> ) <sup>2</sup>			Class 1, 2 and 3 reservoirs	Konno et al (2010)

(\*) computed from model proposed by Stone (1970)  $k_{rA} = (S^*_{irA})^n$ ;  $S^*_{irA} = (S_A - S_{irA})/(1-S_{irA})$ ;  $k_{rG} = (S^*_{irG})^n$ ;  $S^*_{irG} = (S_G - S_{irG})/(1-S_{irG})$

(\*\*) estimated value

(\*\*\*) varies for clay, silt and sand

(\*\*\*\*) For the case of Class 3: 14° C and k<sub>o</sub> = 500mD

ND = no data provided

The analysis of gas production requires complex coupled thermo-hydro-mechanical codes such as (Moridis et al. 2014; Hong and Pooladi-Darvish 2005; Moridis et al. 2008; Walsh et al. 2009; Konno et al. 2010): TOUGH + HYDRATE (Lawrence National Lab), MH21-HYDRES (Japan Oil Engineering Company), CMG-STAR3 (Computer Modelling Group, Canada), STOMP-HYD (Pacific Northwest National Laboratory). These codes involve a large number of equations, constitutive relations and parameters. Table 5.3 shows some of the key parameters involved in these simulations.

Analytical solutions have been proposed to analyze local conditions (Kwon et al. 2008) thermal stimulation (Ullerich et al. 1987; Esmailzadeh et al. 2011; Klar et al., 2013), and depressurization (Goel et al, 2001; Ji et al., 2001; Hong et al. 2003; Tsypkin 2000). However these analyses remain complex, require iterative solution and hide explicit relations between governing parameters.

When solving engineering problems both, transient and steady state analyses are very relevant. Transient solutions are typically used, amongst others, to learn about gas production rate, to investigate optimal production strategies, and to perform sensitivity studies aimed at understanding the impact of material parameters (and other factors) on gas production. Steady state analyses are equally relevant because they inform about the limit (or final condition) of the problem under study. This section studies the analytical solution for the steady state condition involving fluid flow in a cylindrical geometry and accounting for the presence of two zones of different permeability coefficients. This solution can be very useful in problems encompassing *HBS* as it provides the physical limit to the zone around a well that can experience dissociation triggered by depressurization. From this solution it is possible to learn about the maximum amount of gas that can be produced from a given reservoir under this assumptions. A similar solution was presented before (Sánchez and Santamarina, 2015) but for the case of a spherical domain.

It was found that the analytical solution for radial flow is a function of four main factors, as follows: the radius of the wellbore area and imposed pressure at wellbore; pressure at the dissociation front (which depends on reservoir temperature through the methane-hydrate phase boundary); pressure at a distant boundary (equal to reservoir initial pressure); and the ratio between the permeability coefficients of the already dissociated hydrate sediment ' $k_{Sed}$ ' and the hydrate bearing sediments ' $k_{HBS}$ '.

The same radial flow problem was solved using the coupled *THCM* numerical code developed in this project to analyze problems involving gas *HBS*. The finite element (*FE*) computer program takes into consideration thermal and hydraulic processes in deformable sediments, and it also account for the changes in sediment properties in the presence of hydrate dissociation. It is based on a fully coupled formulation that incorporates the different phases and species existing in *HBS* (including hydrate and ice) and it has been implemented in *CODE\_BRIGHT* (Olivella et al., 1996), an existing coupled multiphysics program for geological media.

To verify the *FE* program, the results of the analytical solution discussed above, were compared against the outputs of a numerical model replicating the same conditions. The effects of critical factors were also analyzed. The comparisons between the analytical solution and the finite element model were very satisfactory.

### 5.1. Axisymmetric Cylindrical Flow between Two Impermeable Layers

At steady-state conditions, the pressure distribution in radial flow is inversely proportional to the logarithm of the radial distance to the well. Therefore there is a physical limit to the zone around a well that can experience pressure-driven dissociation. A simple yet robust set of equations to estimate limits for gas production from hydrate bearing sediments using depressurization has been proposed.

Considering radial flow conditions governed by Darcy's law in a thin and confined reservoir with impermeable layers, the following equations are derived:

$$v = k \frac{dh}{dr} \quad (5.1)$$

$$v = \frac{q}{2\pi rH} \quad (5.2)$$

where  $v$  [m/Sec] is the flow velocity at any specified points,  $k$  [m/Sec] is the hydraulic conductivity of medium,  $h$  [m] is the head pressure at any specified point of reservoir (since it is a thick reservoir, the variation of head pressure due to elevation is negligible),  $r$  [m] is the radius of any specified point from the center of wellbore area,  $q$  [m<sup>3</sup>/Sec] defines the flow at specific any point and  $H$  [m] is the thickness of sediments. By combining these two equations and solving them in cylindrical coordinates, the flow equation could be written as:

$$\int_{r_1}^{r_2} \frac{qdr}{r} = - \int_{h_1}^{h_2} (2\pi kH) dh \quad (5.3)$$

The flow between two given points can be calculated as:

$$q = - \frac{2\pi kH(h_2 - h_1)}{\ln\left(\frac{r_2}{r_1}\right)} \quad (5.4)$$

Two zones can be identified under steady state conditions when the pressure drop is kept constant and hydrates stop dissociating: the inner zone where hydrate has been depleted and the outer zone where hydrate remains stable (Figure 5.7). Let's define the size of the produced zone as  $r^*$  [m], and the total head pressure at a distant boundary as  $h_{far}$  [m]. The inner zone is characterized by the permeability of the sediment without hydrates ' $k_{Sed}$ ' and the outer zone by the permeability of the hydrate bearing sediment ' $k_{HBS}$ '. Clearly, gas was produced from the inner zone ' $r \leq r^*$ '. Therefore at steady state conditions the following equations are valid:

$$q_{Sed} = q_{HBS} \quad (5.5)$$

$$\frac{2\pi k_{Sed} H (h^* - h_w)}{\ln\left(\frac{r^*}{r_w}\right)} = \frac{2\pi k_{HBS} H (h_{far} - h^*)}{\ln\left(\frac{r_{far}}{r^*}\right)} \quad (5.6)$$

In the above equations,  $h^*$  [m] and  $h_w$  [m] are the head pressure at dissociation front and at wellbore area respectively, and  $r_w$  [m] is the radius of well. Based on the aforementioned equation, at steady state conditions, the ultimate radius ' $r^*$ ' of the dissociated area is:

$$r^* = \left( r_w r_{far} \left( \frac{k_{Sed}}{k_{HBS}} \right) \left( \frac{h^* - h_w}{h_{far} - h^*} \right) \right)^{\frac{1}{1 + \left( \frac{k_{Sed}}{k_{HBS}} \right) \left( \frac{h^* - h_w}{h_{far} - h^*} \right)}} \quad (5.7)$$

As shown above, according to this simple yet robust analytical solution, the ultimate radius of pressure induced dissociation front in a thick and confined hydrate deposit is a function of (Figure 5.2): 1) the radius of the wellbore area ' $r_w$ ' and wellbore head pressure ' $h_w$ '; 2) head pressure at the dissociation front ' $h^*$ ' (which in turns depends on reservoir temperature through the methane hydrate phase boundary); 3) head pressure at a distant boundary ' $h_{far}$ ' (equal to reservoir initial pressure); and 4) the ratio between the hydraulic conductivity of the already dissociated hydrate sediment ' $k_{Sed}$ ' and the hydrate bearing sediments ' $k_{HBS}$ '.

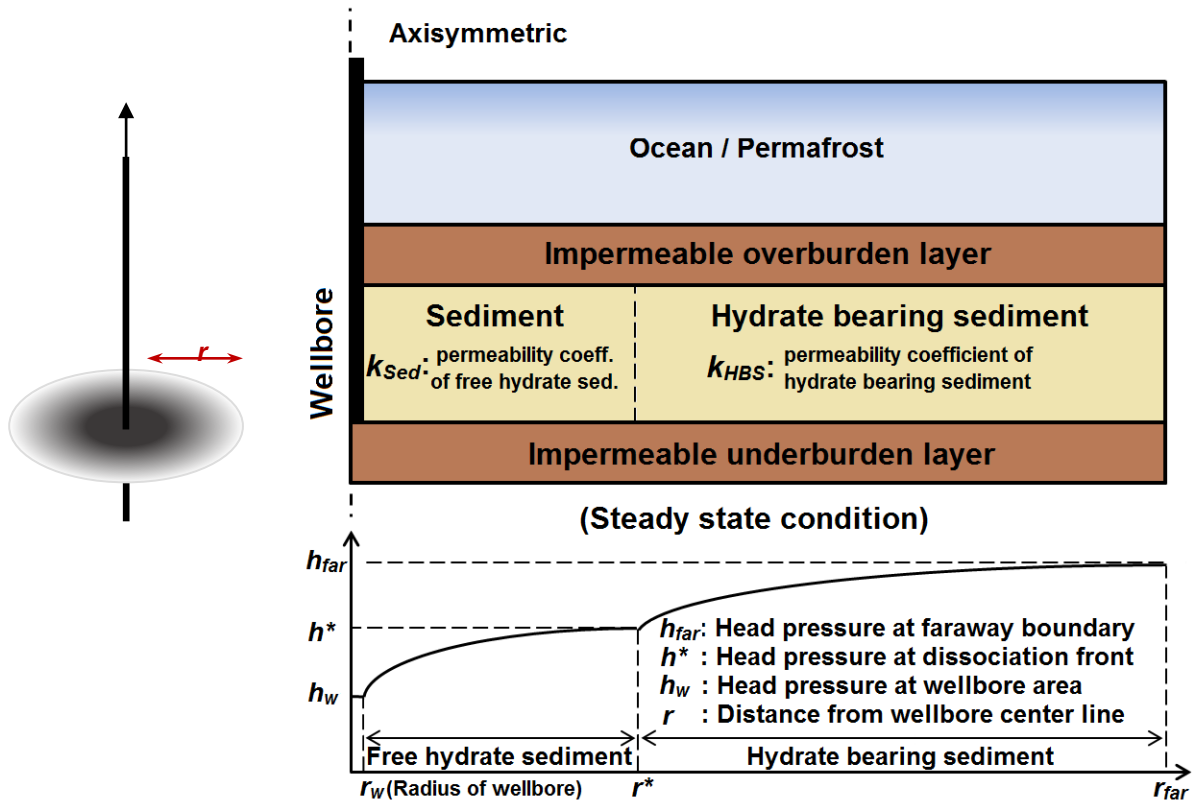


**Figure 5-2** Two zones can be identified under steady state conditions when the pressure drop is kept constant and hydrate stops dissociating: an inner zone where hydrate has been depleted and an outer zone where hydrate remains stable.

Based on the law of refraction of streamlines (Bear, 1979) at boundary of two homogeneous layers with different permeability coefficients, the refraction of flow lines is described as follow:

$$\frac{k_1}{\tan \delta_1} = \frac{k_2}{\tan \delta_2} \quad (5.8)$$

where  $k_1$  and  $k_2$  stand for hydraulic conductivity of each layers while  $\delta_1$  and  $\delta_2$  are the angles which streamlines in corresponding layer make with the normal vector of boundary surface. It follows that when  $k_1 \gg k_2$  then  $\delta_1 \gg \delta_2$  and the refracted streamline approaches the normal to the boundary surface on passing from one porous medium to another, less permeable than the first. Similarly, the refracted streamlines tend to become almost parallel to the common boundary on passing from less to higher permeable layer. Therefore if the reservoir is confined between two very low permeable layers then horizontal flow lines in reservoir and vertical flow lines in low permeable confining layers can be assumed. Hence, an approximate solution can be derived by following additional assumptions: the flow in the less permeable layers ascend or descend vertically based on the direction of the hydraulic gradient within this layer; head of pressure above/bellow the less permeable overburden/underburden layer is constant; reservoir and confining layers are homogeneous therefore corresponding coefficients of permeability are constant within each layers; the variation of head pressure due to the elevation is negligible by considering the thickness of layers; and the length of very low permeable layer is theoretically infinite, then at the steady state condition flow in the reservoir is sustained almost entirely by the leakage.

Considering radial flow conditions governed by Darcy's law in a thin reservoir, the following equations are derived:

$$v = k \frac{dh}{dr} \quad (5.9)$$

$$v = \frac{q}{2\pi rH} \quad (5.10)$$

where  $v$  [m/Sec] is the flow velocity at any specified point,  $k$  [m/Sec] is the hydraulic conductivity of medium,  $h$  [m] is the head pressure at any specified point of reservoir (since it is a thick reservoir, the variation of head pressure due to the elevation is negligible),  $r$  [m] is the radius of any specified point from the center of wellbore area,  $q$  [m<sup>3</sup>/Sec] defines the flow at any specific point and  $H$  [m] is the thickness of sediments. By combining these two equations and solving them in cylindrical coordinates, the flow at any specific radius of reservoir 'r' could be written as:

$$q_r = 2\pi rHk \frac{\partial h}{\partial r} \quad (5.11)$$

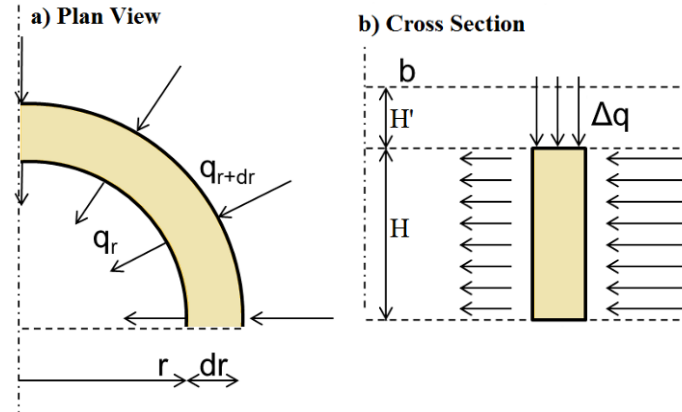


**Figure 5-3** General description for a half depth of reservoir confined by less permeable layers. If  $k' \ll k$  then horizontal streamlines within reservoir and vertical ascended/ descended flow lines into reservoir from less permeable confining layers can be assumed.

As illustrated in Fig.5.3 by considering the equilibrium at steady state condition for a tiny section of reservoir, following the equation yield:

$$2\pi r H k \frac{\partial h}{\partial r} - 2\pi (r + dr) H k \frac{\partial h}{\partial r} - \pi \left[ (r + dr)^2 - r^2 \right] k' \frac{h_0 - h_r}{H'} = 0 \quad (5.12)$$

in which, as shown in Fig.5.4,  $H$  [m] and  $H'$  [m] are the half depth of symmetric reservoir and depth of each confining layers,  $k$  [m/Sec] and  $k'$  [m/Sec] stand for hydraulic conductivity of reservoir and confining layers respectively. As it is illustrated in Fig.5.5, if the reservoir is confined by both impermeable layer from one side and less permeable layer on the other side then  $H$  should be considered as a full depth of reservoir.  $h_0$ [m] represents the initial reservoir head pressure which is equal to the head pressure at far distance " $h_{far}$ ". Modified Bessel Functions of order zero provides the general solution for Eq. (5.12) (De Glee 1951):

$$h_0 - h_r = \alpha_1 I_0 \left( \frac{r}{\beta} \right) + \alpha_2 K_0 \left( \frac{r}{\beta} \right) \quad (5.13)$$

in which  $I_0$  and  $K_0$  are the first and the second kind of Modified Bessel Function respectively and  $\beta$  stands for leakage factor which is defined as:

$$\beta = \sqrt{\frac{k H H'}{k'}} \quad (5.14)$$

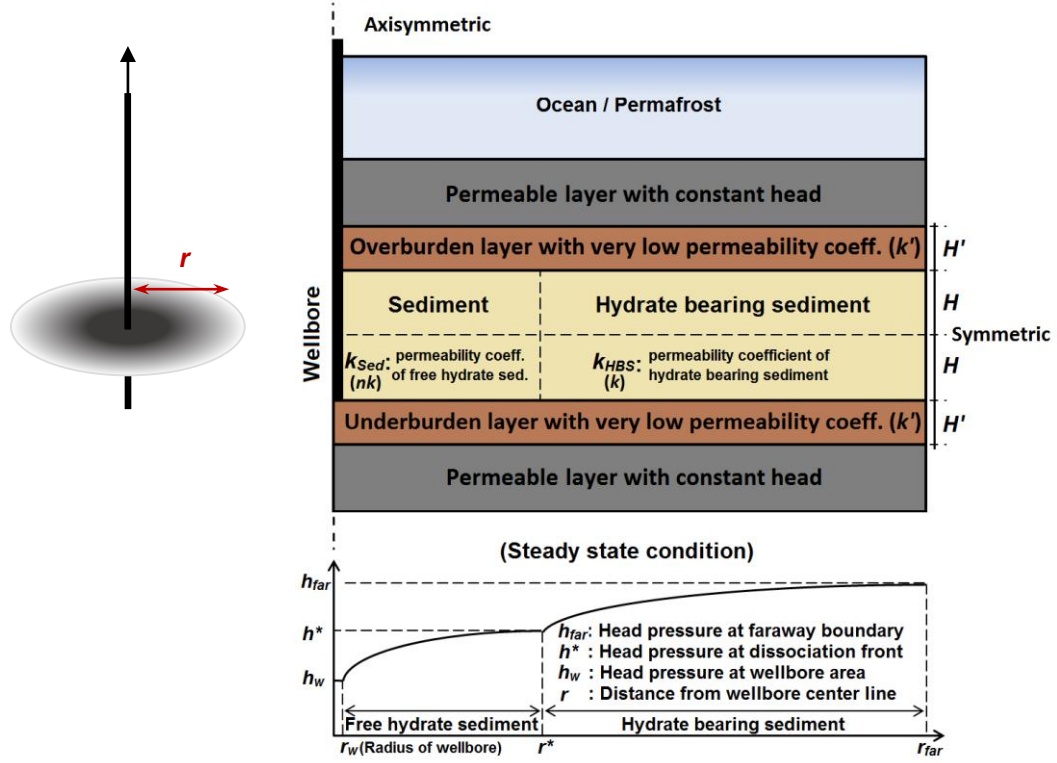


**Figure 5-4** Axisymmetric HBS reservoir confined between less permeable layers. At steady state condition, reservoir is divided in two zones of free hydrate sediments and HBS by an interface radius know as dissociation front ( $r^*$ ). The homogenous porous medium through the reservoir is assumed; therefore  $k_{Sed}=k_{HBS}=k$  and consequently  $n=1$ .

Two boundary conditions can be considered: no drawdown at far distance and constant discharge at wellbore area. Therefore,  $\alpha_1$  and  $\alpha_2$  are derived as:

$$(r = \infty) \rightarrow h_r - h_0 = 0 \rightarrow \alpha_1 = 0 \quad (5.15)$$

$$q_w = 2\pi r_w H k \left. \frac{\partial h}{\partial r} \right|_{r=r_w} \rightarrow \alpha_2 = \frac{q_w}{2\pi k H \left( \frac{r_w}{\beta} \right) K_1 \left( \frac{r_w}{\beta} \right)} \quad (5.16)$$

in which  $K_1$  is the second kind of Modified Bessel Function of first order and  $q_w$  is calculated by knowing the drawdown at wellbore area:

$$q_w = \frac{2\pi H k [h_0 - h_w] \left( \frac{r_w}{\beta} \right) K_1 \left( \frac{r_w}{\beta} \right)}{K_0 \left( \frac{r_w}{\beta} \right)} \quad (5.17)$$

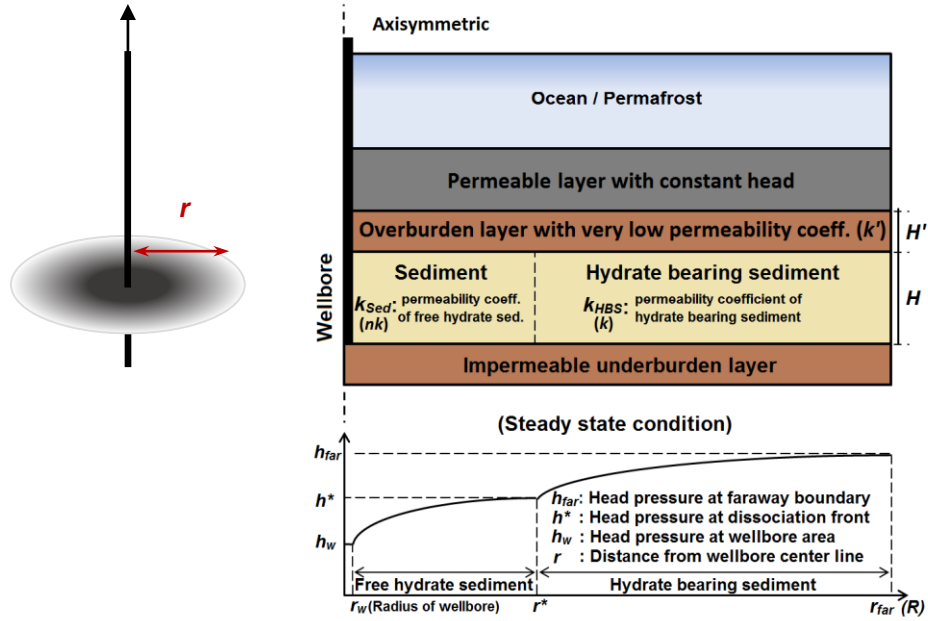


**Figure 5-5** Axisymmetric HBS reservoir confined between impermeable layer from one side and less permeable layer from another side. The homogenous porous medium through the reservoir is assumed; therefore  $k_{Sed.}=k_{HBS.}=k$  and consequently  $n=1$ .

At steady state conditions when the pressure drop is kept constant and hydrates stop dissociating, from wellbore area up to dissociation front ' $r^*$ ' hydrates have been depleted and also remain stable beyond that radius. As a result, if  $h^*$ [m] is the head of pressure at dissociation front ' $r^*$ ' based on corresponding temperature on hydrate phase stability boundary diagram then  $S^*$  is the drawdown at this radius. Therefore at steady state conditions, the ultimate radius ' $r^*$ ' of the dissociated area is calculated as:

$$S^* = h_0 - h^* = \frac{q_w}{2\pi Hk} \frac{K_0\left(\frac{r^*}{n\beta}\right)}{\left(\frac{r_w}{\beta}\right) K_1\left(\frac{r_w}{\beta}\right)} \quad (5.18)$$

$$r^* = K_0^{-1} \left[ \frac{S^* 2\pi Hk \left(\frac{r_w}{\beta}\right) K_1\left(\frac{r_w}{\beta}\right)}{q_w} \right] \times (\beta) \quad (5.19)$$

As shown in Eq. (5.18) and Eq. (5.19), the ultimate radius of pressure induced dissociation front in a thick hydrate deposit confined by infinite low permeable layers is a function of (: 1) the radius of the wellbore area ' $r_w$ ' and wellbore head pressure ' $h_w$ '; 2) head pressure at the dissociation front ' $h^*$ ' (which in turns depends on reservoir temperature through the methane hydrate phase boundary); 3) initial reservoir head pressure ' $h_0$ '; 4) and also the leakage factor which depends on the square root of ratio between permeability coefficient of reservoir sediments and that of confining layers as well as a function of their corresponding thicknesses.

## 5.2. Numerical analysis for code verification

Numerical models were developed based on the formulation introduced in Section 2 to conduct the code verification. Several models were prepared based on various reservoir initial conditions and also different production strategies by imposing a variety of possible pressures at the wellbore to verify the code performance when compared against the results from the analytical solution. These analyses also allowed studying the effect of crucial parameters and factors related to the problem of hydrate dissociation induced by depressurization. Table 5.4, presents the initial reservoir conditions and also the imposed pressure at the wellbore for the cases studied in this report.

**Table 5-4:** Cases considered in the analysis

Case	$h_{far}$ (m)	$h_w$ (m)	$T$ ( °C)	$\frac{h^* - h_w}{h_{far} - h^*}$
A	1020	306	12	7.14
B	1224	306	12	2.14
C	1224	510	12	1.44
D	1224	306	10	0.91
E	1224	306	8	0.47

An intrinsic permeability coefficient for hydrate bearing sediments  $k_{HBS}=1 \times 10^{-12} \text{ m}^2$  was considered in all the models (2.18). A hydrate saturation  $S_h=0.5$  was adopted. The different ratios between already dissociated hydrate sediment permeability coefficient ( $k_{sed}$ ) and  $k_{HBS}$  were obtained by adopting different values of the hydrate morphology coefficients  $N$ .

A long ( $L=1.20\text{km}$ ) and thin ( $h=0.40\text{m}$ ) domain was adopted in the analyses. A 2D axisymmetric geometry was modeled based on a single vertical well producing from a cylindrical section, confined by impermeable layers, with a very fine grid. Mesh discretization along the radial direction was not uniform, increasing logarithmically from 0.12m at  $r_w$  to 0.80m at  $r_{max}$ . The final discretization consists of 5008 nodes and 2503 elements. This high degree of refinement provided the level of detail required to capture crucial processes near the wellbore and the entire *HBS* layer.

**Table 5-5:** Model parameters used in numerical simulation

Parameter	Value
Initial saturation	$S_h=0.50, S_l=0.50, S_g=0.00$
Intrinsic permeability in <i>HBS</i>	$k_{HBS}=1 \times 10^{-12} \text{ m}^2$ (Isotropic)
Porosity of <i>HBS</i>	$\phi=0.40$
Capillary pressure model	$P_o=100 \text{ kPa}; \lambda=0.5$
Liquid relative permeability model	$a = 1$
Gas relative permeability model	$b = 1$

A long term depressurization was considered in the numerical analyses to reach the steady state condition. In some occasions, the steady state condition were not fully achieved (even for the very long time duration performed analyses). In these cases, the final conditions were not very far from the steady state ones. In fact, in practically all the cases analyzed, the analytical solution predicted a little bit further dissociation front than the *FE* solution. Therefore, it appears that if the models would run for longer times, both results could match even better. In all the cases, the radii of wellbore area was  $r_w=0.1\text{m}$ , and a very long length of the reservoir is modelled to have a realistic distant (fix) boundary condition. It is also assumed that the rate of heat conductivity is high enough to compensate the temperature reduction due to the endothermic behavior of hydrate dissociation by reaching the steady state condition. Therefore the head of pressure at dissociation front ' $h^*$ ' is derived from methane hydrate phase boundary diagram for a given reservoir initial temperature.

Figure 5.6 presents the results of the discussed analytical solution (dash lines) for the different cases listed in Table 5.5, showing the interplay between the relative sediment permeability coefficients ' $k_{Sed}/k_{HBS}$ ' and the relative pressure dissociation ' $(h^* - h_w)/(h_{far} - h^*)$ '. As shown, the numerical results (solid line) are very satisfactory when compared against the analytic ones for the variety range of conditions analyzed.

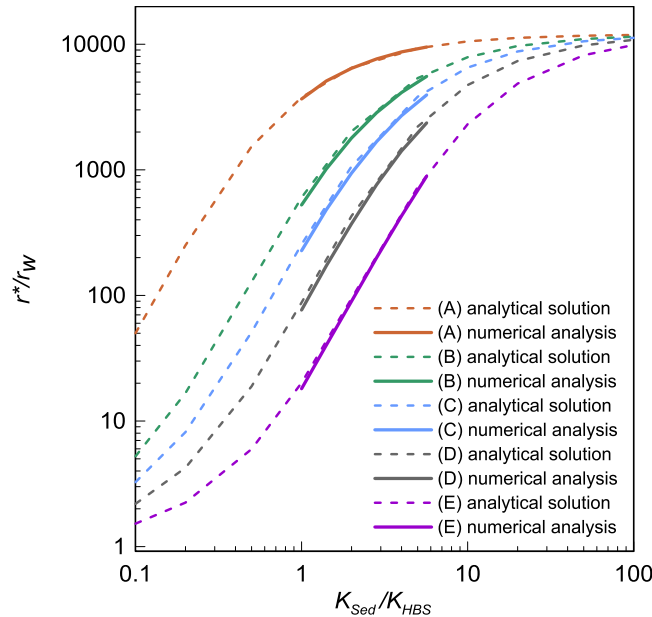


**Figure 5-6** Results obtained with the analytical solution for the case of reservoir confined between two impermeable layers and numerical models for the different cases listed in Table 5.5.

Moreover, the effect of some relevant parameters related to methane production from gas-hydrate induced by depressurization is illustrated in Fig.5.6. As expected, it is predicted that the dissociation front will be farthest from the well in those cases in which the permeability coefficient increases more with hydrate dissociation. This implies that the degree of permeability enhancement by dissociation (which depends on hydrate morphology) plays an essential role in the depressurization propagation in *HBS*.

When comparing *Cases A, B* and *C* for the same initial and wellbore pressure, it shows that the more gas hydrate is released from warmer reservoir. It is also observed that *Cases A* and *C* have the same hydraulic gradient between wellbore area and distant boundary, as well as, the same initial temperature but with different initial pressure. The lower initial pressure of reservoir, the higher amount of produced gas.

### 5.3. Recoverable Gas: Energy

The energy density of gas methane is  $E_d = 46$  MJ/kg STP, while the density for hydrate is just  $E_d = 4.8$  MJ/kg of hydrate mass (Hermann, 2005). The recoverable energy RE [J] from a hydrate bearing sediment with hydrate saturation  $S_{hyd}$  [--] when  $V$  [ $m^3$ ] is:

$$RE = V n S_{hyd} E_d \rho_{hyd} e \quad (5.20)$$

where  $n$  is the porosity, and  $e$  the gas recovery efficiency. The recovery efficiency  $e$  depends on the interaction of gas with other fluids (such as water) in the reservoir as a function of pore size distribution and connectivity (Jang and Santamarina 2011). For the case when gas is the only fluid displaced and water remains in the reservoir (represents the case with maximum gas recovery).

$$e = \frac{\beta - 1}{\beta - 0.79} \quad (5.21)$$

where  $\beta$  is the fluid expansion factor as the ratio of the combined gas and water volumes to the initial volume of hydrate. Typical values are  $\beta = 1.3$  ( $u = 30$  MPa) and  $e = 0.6$ ; and  $\beta = 6$  ( $u = 3$  MPa) and  $e = 0.96$ . Figure 5.7 shows the profit per hydrate thickness vs. radius of dissociation  $r^*$  estimated for selected reservoirs. The most profitable extraction reservoirs are the Ulleung Basin and Nankai Trough where the cost of gas is almost 4 times the price in USA (FERC: Federal Energy Regulatory Commission - [www.ferc.gov](http://www.ferc.gov)). The low costs of gas extraction in USA hinder the possibility of gas extraction in the near future. Table 5.6 summarizes values used for these computations.

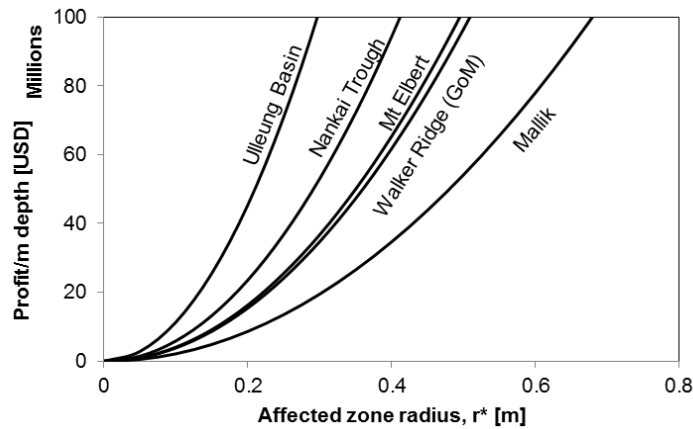


**Figure 5-7** Economical analysis. Profit per hydrate thickness with respect to dissociation front for selected potential locations.

**Table 5-6: Profit analysis**

Reservoir						
Parameter	Unit	Mallik	Walker Ridge (GoM)	Mt Elbert	Korea	Japan
$H_{hyd}$	[m]	10	200	11	20	100
$k_{sed}$	[m/s]	$10^{-7}$	$10^{-7}$	$10^{-6}$	$10^{-6}$	$10^{-7}$
$k_{hbs}$	[m/s]	$10^{-9}$	$10^{-8}$	$10^{-9}$	$10^{-9}$	$10^{-8}$
$n$	[--]	0.28	0.5	0.4	0.5	0.35
$S_{hyd}$	[--]	0.5	0.7	0.65	0.5	0.5
$E_d$	[MJ/kg]			46		
$\rho_{hyd}$	[kg/m <sup>3</sup> ]			920		
$\beta$	[--]	2.5	1.35	2.7	1.4	1.2
$e$	[--]	0.88	0.63	0.89	0.66	0.49
RE	[MJ/m <sup>3</sup> ]*	1703.7	3034.8	3210.5	2274.3	1184.3
Price (**)	[USD/MJ]		4220		16563.5	16510.75

(\*) MJ per volume of dissociated gas

(\*\*) Data from [www.ferc.gov](http://www.ferc.gov), 2013

*Comparison with literature.* Numerical simulations show the time evolution of gas production typically for several years. However, the analysis conducted here is for steady state conditions at the end of gas production. Table 5.6 shows input values and numerical simulations results. Figure 5.8 compares numerical and analytical results. The close-form analytical solutions presented here predicts ultimate radius of dissociation to be within 1 and 1.15 the numerically computed value. The difference may be due to the fact that none of the numerical simulations are run to the ultimate radius, but a radius close to the final value.

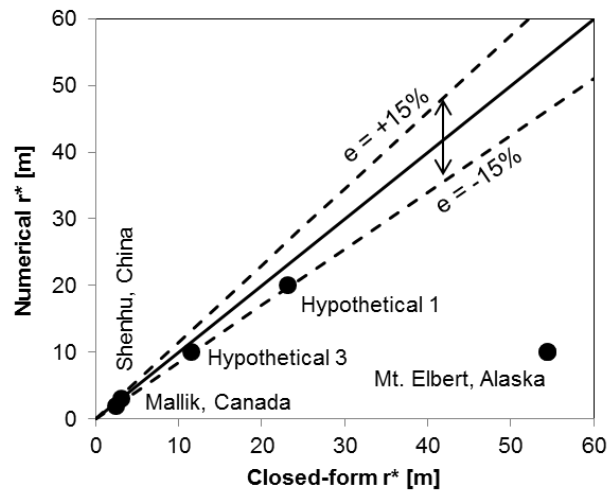


**Figure 5-8** Dissociation front computed tends to be larger than the values from the literature but contained in a 15% error area. Note that Mt. Elbert simulations were stopped after 10800 days of production (i.e. no ultimate radius of dissociation was reached)

**Table 5-7:** Data input for equations for selected cases

Case	H [m]	r <sub>w</sub> [m]	b (*) [m]	k <sub>sed</sub> [m/s]	k <sub>hbs</sub> [m/s]	k' [m/s]	S <sub>hyd</sub> [--]	h <sub>w</sub> [MPa]	h <sub>far</sub> [MPa]	h* (**) [MPa]	Data based on:	Solution	
												r* [m]	Vol gas [m3]
Hypothetical 1	1	0.1	1	6.5 10 <sup>-9</sup>	3.810 <sup>-9</sup>	1.010 <sup>-14</sup>	0.10	2.70	5.70	4.70	Moridis et al (2007)	<b>23.1</b>	1.210 <sup>4</sup>
Hypothetical 2	15	0.1	1	6.5 10 <sup>-6</sup>	1.910 <sup>-9</sup>	1.010 <sup>-14</sup>	0.70	3.00	12.00	11.20	Moridis et al (2006)	<b>3750.0</b>	2.510 <sup>10</sup>
Hypothetical 3	50	0.1	1	3.2 10 <sup>-6</sup>	5.110 <sup>-7</sup>	3.010 <sup>-6</sup>	0.60	4.00	12.00	11.80	Konno et al (2010)	<b>11.5</b>	9.110 <sup>5</sup>
Mallik, Canada	20	0.1	1	1.310 <sup>-7</sup>	2.110 <sup>-9</sup>	1.010 <sup>-7</sup>	0.50	3.00	11.00	9.40	Moridis et al (2004)	<b>2.5</b>	1.05E+04
Mt Elbert, Alaska	11.3	0.1	1	6.510 <sup>-6</sup>	5.7 10 <sup>-9</sup>	1.010 <sup>-10</sup>	0.65	3.00	6.40	3.20	Moridis et al (2011)	<b>54.4</b>	5.0 10 <sup>6</sup>
Shenhu, China	10	0.1	1	6.510 <sup>-8</sup>	3.910 <sup>-9</sup>	1.010 <sup>-7</sup>	0.30	3.00	12.00	11.84	Su et al (2012)	<b>3.2</b>	6.910 <sup>3</sup>
Ulleung Basin, Korea	70	0.1	1	3.210 <sup>-6</sup>	2.210 <sup>-9</sup>	1.010 <sup>-12</sup>	0.70	3.00	23.00	11.60	Moridis et al (2013)	<b>1600.0</b>	3.8 10 <sup>10</sup>
Nankai Trough, Japan	22	0.1	1	6.510 <sup>-7</sup>	1.310 <sup>-8</sup>	1.010 <sup>-12</sup>	0.50	3.00	13.00	11.60	Kurihara et al (2009)	<b>1700.0</b>	7.510 <sup>9</sup>

(\*) Assumed values

(\*\*) Computed from temperature following Kwon et al (2008)

(\*\*\*) Obtained from hydrate saturation front figures

H = hydrate bearing sediment layer thickness; r\* = radius of dissociation; r<sub>w</sub> = radius of the well; b = aquitard thickness; k<sub>sed</sub> = sediment hydraulic conductivity; k<sub>hbs</sub> = hydrate bearing sediment hydraulic conductivity; k' = aquitard hydraulic conductivity; S<sub>hyd</sub> = hydrate saturation; h<sub>w</sub> = well pressure; h<sub>far</sub> = far field pressure, h\* = dissociation pressure

ND = no data provided

**Table 5.7:** Data input for equations for selected cases.

**Solutions from numerical simulations**

<b>Case</b>	<b>r* (***)</b> <b>[m]</b>	<b>Vol gas</b> <b>[m3]</b>	<b>Observations</b>	<b>Reference</b>
Hypothetical 1	<b>20.0</b>	5 10 <sup>3</sup>	Confined aquifer	Moridis et al (2007)
Hypothetical 2	<b>ND</b>	1 10 <sup>8</sup>	Class 1 reservoir: free gas zone - Confined aquifer	Moridis et al (2006)
Hypothetical 3	<b>10.0</b>	1 10 <sup>8</sup>	Class 3 reservoir - non confined aquifer	Konno et al (2010)
Mallik, Canada	<b>2.0</b>	ND		Moridis et al (2004)
Mt Elbert, Alaska	<b>10.0</b>	5.5 10 <sup>6</sup>	Simulation stopped after 10800 production days (not ultimate radius)	Moridis et al (2011)
Shenhu, China	<b>4.0</b>	9 10 <sup>3</sup>		Su et al (2012)
Ulleung Basin, Korea	<b>250.0</b>	9 10 <sup>7</sup>	r* reaches the boundary of the simulations - Confined aquifer	Moridis et al (2013)
Nankai Trough, Japan	<b>120.0</b>	3 10 <sup>7</sup>	r* reaches the boundary of the simulations - Confined aquifer	Kurihara et al (2009)

(\*) Assumed values

(\*\*) Computed from temperature following Kwon et al (2008)

(\*\*\*) Obtained from hydrate saturation front figures

ND = no data provided

*Discussion: real case scenario.* The decrease in pore water pressure causes an increase in effective stress, volume compaction and the decreased sediment permeability  $k_{sed}$ . This is demonstrated next for the case of radial flow. Water pressure distribution is (Muskat 1946):

$$u(r) = \frac{h_{far} - h_w}{\log\left(\frac{r_{far}}{r_w}\right)} \log\left(\frac{r}{r_w}\right) + h_w \quad (5.22)$$

Effective stress is a function of the initial total stress  $\sigma_0$  at the depth of the reservoir. The change in void ratio for large stress is estimated as ( $e_{1kPa}$  is the void ratio at  $\sigma'=1$  kPa and  $\beta$  a soil parameter):

$$e(\sigma') = e_{1MPa} \left(\frac{\sigma'}{1MPa}\right)^{-\beta} \quad (5.23)$$

Where  $e_{1kPa}$  is an arbitrary reference value of void ratio;  $\beta$  a soil parameter.

Permeability can be found from (Ren and Santamarina;  $k_{1kPa}$  is the reference permeability at  $\sigma' = 1$  kPa and  $b$  is a soil parameter which depends on specific surface – for the case of coarse grained soils  $b = 3.5$ ):

$$k(e) = k_{1MPa} \left(\frac{e}{e_{1MPa}}\right)^b \quad (5.24)$$

With this new change in permeabilities, the pore water pressure distribution will be modified again. Note that the new pore water pressure distribution will lead a change in effective stress, void ratio and permeability. Figure 5.16 shows an example for the data from Nankai Trough (summarized in Table 5.8). Figure 5.16-a represents the initial pore pressure and effective stress distribution on the well and its impact on the void ratio, hydraulic conductivity and flow rate for a steady state condition (Figure 5.9-b, -c and -d). The permeability and flow rate fall several orders of magnitude.

**Table 5-8:** Summary of parameters for the example in Figure 5.9

Parameter	Symbol	Units	Value
Total stress in the reservoir	$\sigma$	[kPa]	16000
Initial water pressure	$h_{far}$	[kPa]	13000
Well water pressure	$h_w$	[kPa]	3000
Radius of influence	$r_{far}$	[m]	100
Radius of the well	$r_w$	[m]	0.1
Reservoir thickness	$H$	[m]	1
Permeability exponent	$b$	[--]	3.5
Void ratio exponent	$\beta$	[--]	0.5
Reference void ratio	$e_{1MPa}$	[--]	1
Reference permeability	$k_{1MPa}$	[cm/s]	$10^{-2}$

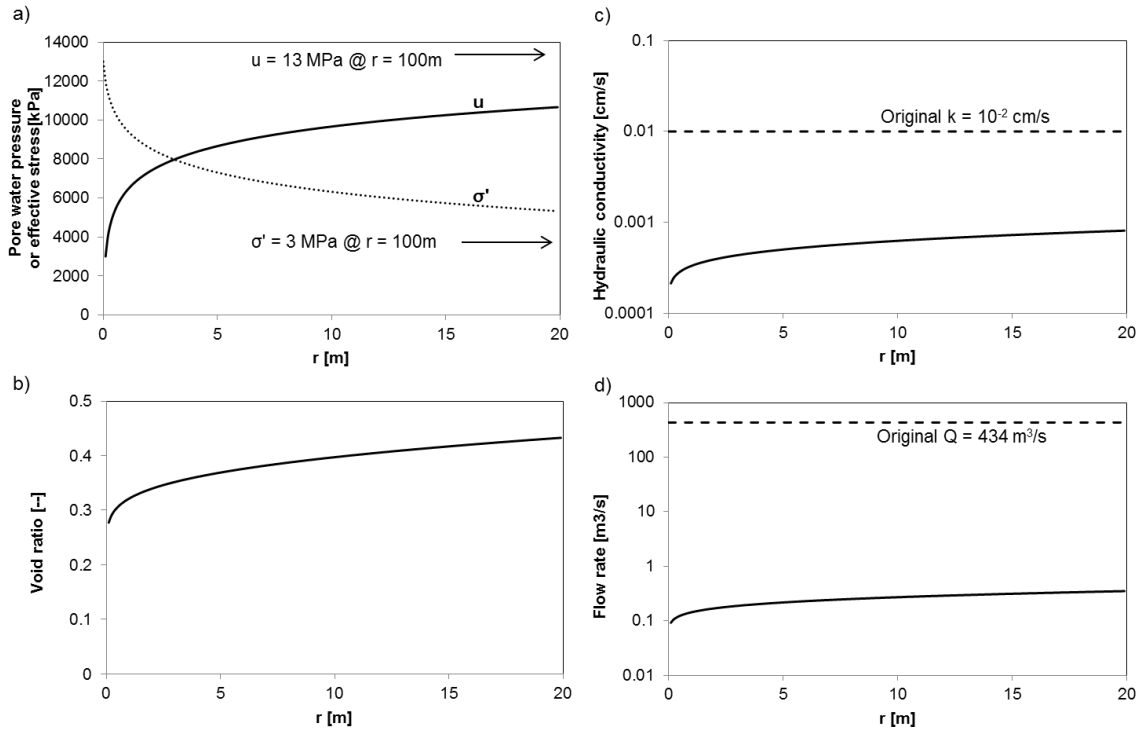


**Figure 5-9** Example of gas hydrate production from a marine environment under depressurization strategy (Summary of parameters used can be found in Table 5.8).

## 6. NUMERICAL ANALYSIS – CODE VALIDATION

In this section the validation of the code against experimental data gathered in the lab from a ventilation test and also two benchmarks prepared in the context of “The National Methane Hydrates R&D Program: Methane hydrate Reservoir Simulator Code Comparison Study” ([http://www.netl.doe.gov/technologies/oil-gas/FutureSupply/MethaneHydrates/MH\\_CodeCompare/MH\\_CodeCompare.html](http://www.netl.doe.gov/technologies/oil-gas/FutureSupply/MethaneHydrates/MH_CodeCompare/MH_CodeCompare.html)) is presented.

### 6.1. Code validation against experimental data

A pressure core recovered from hydrate bearing sediments in the Krishna-Godavari Basin was depressurized while measuring the internal temperature in the sediment at the center of the core (Yun et al., 2010). The main goal of this exercise is to check if the mathematical formulation (presented in Section 2) is able to capture the main features observed in the depressurization test.

The samples used in the experiment were part of the first Indian National Gas Hydrate Program expedition (*NGHP* expedition 01) which took place in the spring and summer of 2006 across the Indian Ocean shoreline. The samples were recovered in water depths ranging between 907 and 2674 m. It included 6 geophysical studies, drilling at 21 sites, logging while drilling of 12 boreholes, and the recovery of both standard and pressure cores. Five pressure cores were recovered at site NGHP-01-21, transferred into storage chambers under hydrostatic pressure, and kept at 4 °C and 13 MPa fluid pressure for subsequent characterization and analysis.

The test program included the measurement of elastic wave velocity, shear strength, and electrical conductivity, followed by fast depressurization of the sub-sampled core round. A specially designed “instrumented pressure testing chamber” (*IPTC*) was used to characterize the cores. The *IPTC* chamber was filled with chilled water (~4 °C) and 13 MPa of fluid pressure was maintained. After conducting initial X-ray imaging, controlled depressurization tests were conducted on the samples. The instrumentation of the sample during the test was conducted at intervals along the length of the samples based on the points of interest ascertained through the X-ray images. The location of the instrumentation for one such sample is shown in Figure 6.1. The total length of the sample used in the depressurization was 380 mm. The fluid pressure of the *IPTC* chamber was slowly reduced until the fluid pressure dropped to 0. Figure 6.2 shows the path in the P-T plane followed during the depressurization experiment.

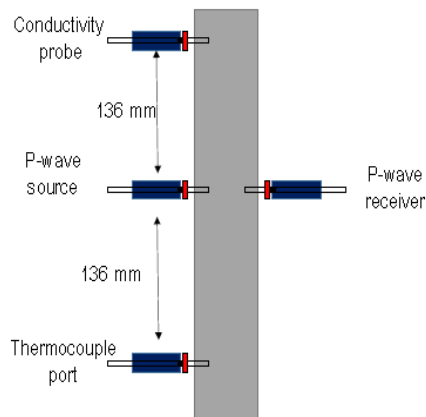


**Figure 6-1** Test instrumentation, sample 21C-02E (modified after Yun et al., 2010)

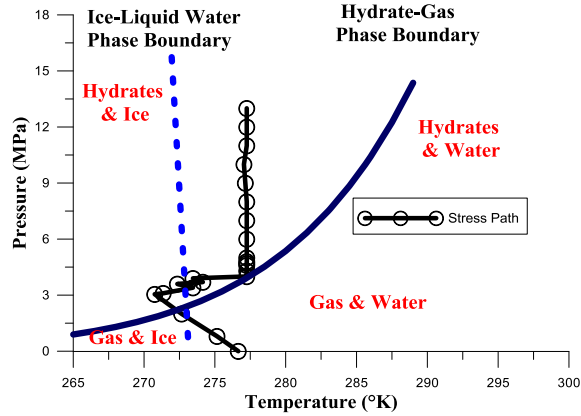


**Figure 6-2** Path in the P-T plane followed during of a pressure core gathered from the Krishna-Godavari Basin (reported by Yun et al., 2009).

It can be observed that the decrease of pressure in the stability zone was almost vertical. Once the P-T path reached the phase boundary dissociation started. Because of the endothermic character of the hydrate dissociation, the sample cooled down during depressurization (as recorded by thermocouples, Fig. 6.2). This induced that the P-T path moved towards the water-to-ice transformation line, reaching freezing temperatures and leading to ice formation.

The change in the temperature, p-wave velocity, electrical conductivity and the amount of gas generated was recorded during the experiment. The relevant results of these tests are shown in Figures 6.3a) and 6.3b). As expected, no gas was produced during the depressurization in the stability zone. However, as soon as the P-T path reached the phase boundary (i.e. for a fluid pressure around 4 MPa), the production of gas started, and it continued until all the hydrate dissociated.

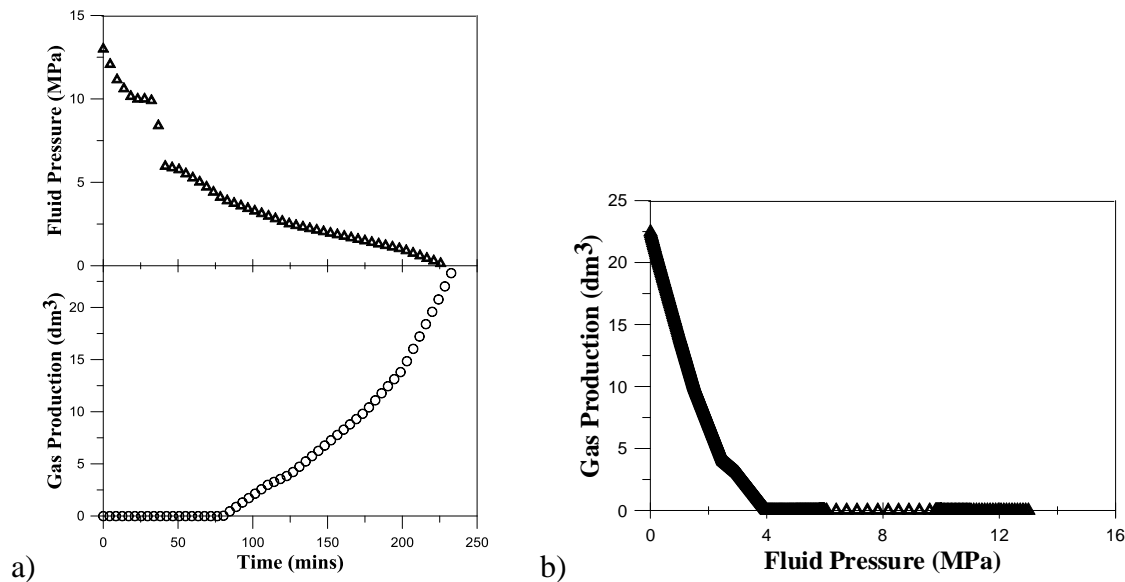


**Figure 6-3** Evolution of the main variables recorded during the experiment: a) time evolution of pressure and gas production; and b) gas production versus fluid pressure (data gathered from the Krishna-Godavari Basin, Yun et al., 2009).

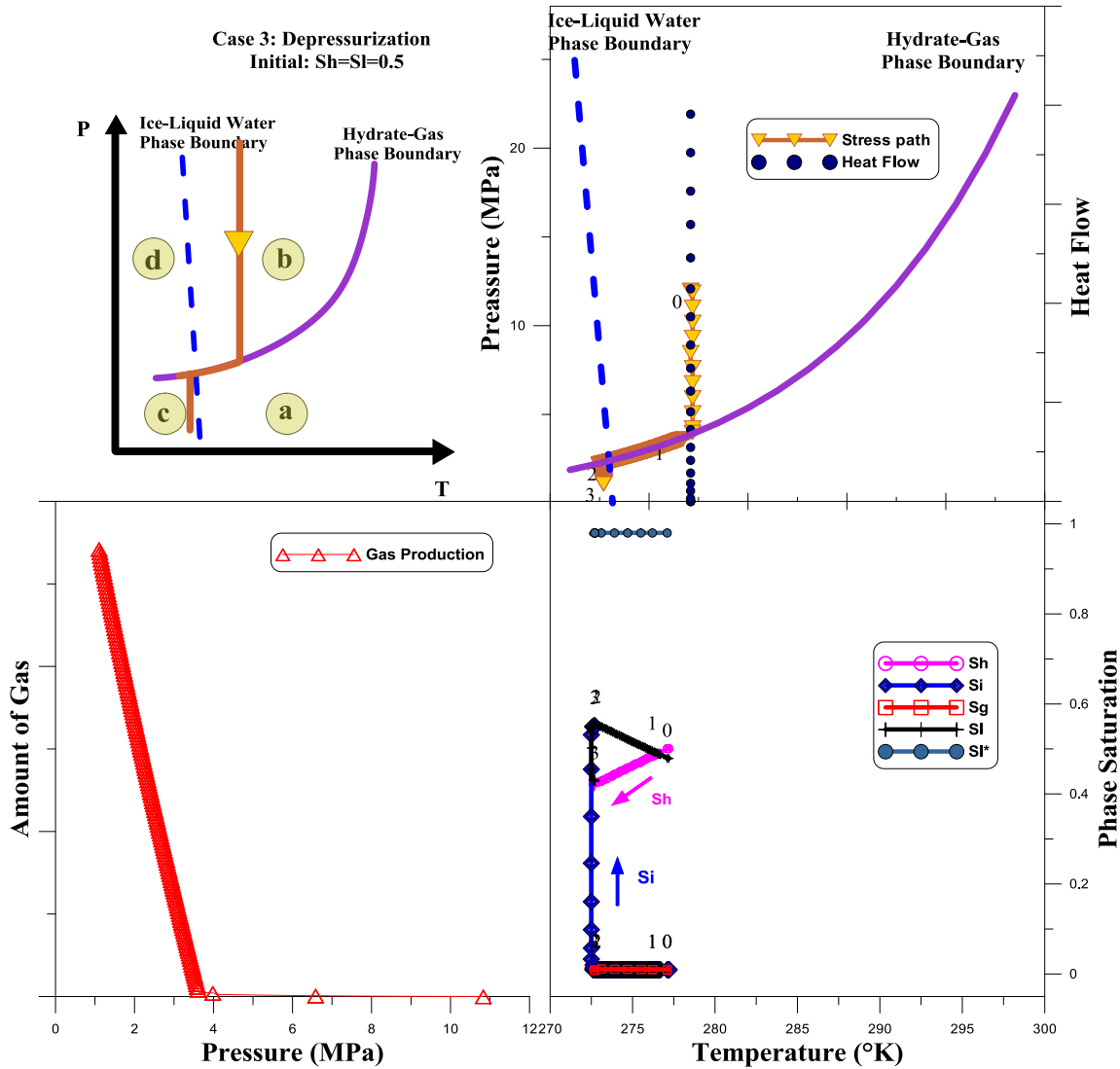


**Figure 6-4** Results of hydrate formation by heating a) Schematic of P-T path b) P-T path plotted in the P-T plane c) Gas produced d) Phase saturation of hydrates, water (liquid), gas and ice.

## 6.2. Benchmark Test 1

The code was also validated using the benchmarks prepared in the context of “The National Methane Hydrates R&D Program: Methane Hydrate Reservoir Simulator Code Comparison Study”. The benchmark Test#1 is related to the analysis of “Non-isothermal Multifluid Transition to Equilibrium”. The main components of this case are briefly mentioned below.

*Processes of interest to the simulation of CH<sub>4</sub> production from gas hydrates in porous media include multifluid flow and heat transport along with complex phase transitions, including hydrate dissociation and formation. A base case problem was designed to examine the numerical simulation of multifluid flow and heat transport processes with a single phase transition from aqueous saturated to unsaturated conditions for a water-CH<sub>4</sub> system outside the stability region for gas hydrate formation. The problem involves a horizontal one-dimensional closed domain (no flow boundary conditions), initialized with gradients in aqueous pressure, gas pressure, and temperature that yield aqueous saturated conditions on half of the domain and aqueous*

unsaturated conditions on the other half of the domain. The simulation then proceeds to an equilibrium condition in pressure and temperature. The results of numerical simulations of CH<sub>4</sub> hydrate formations in geologic media largely depend on the computation of thermodynamic and transport properties. Therefore, a portion of this problem involves reporting property data for selected temperatures and pressures.

**Base Case Problem Description.** Gradients in aqueous pressure, gas pressure, and temperature are imposed across a 20-m one-dimensional horizontal domain, discretized using uniformly spaced 1-m grid cells. A horizontal domain is used to eliminate gravitational body forces from the problem, as an additional simplification. The pressure and temperature gradients are specified to yield aqueous saturation conditions in the first 10 grid cells and aqueous unsaturated conditions in the remaining 10 grid cells. The simulation then proceeds to equilibrium conditions in pressure, phase saturations, and temperature. Variable time stepping should be used to capture the flow and transport processes at early and late times during simulation. Figure 6.5 shows the problems schematic.

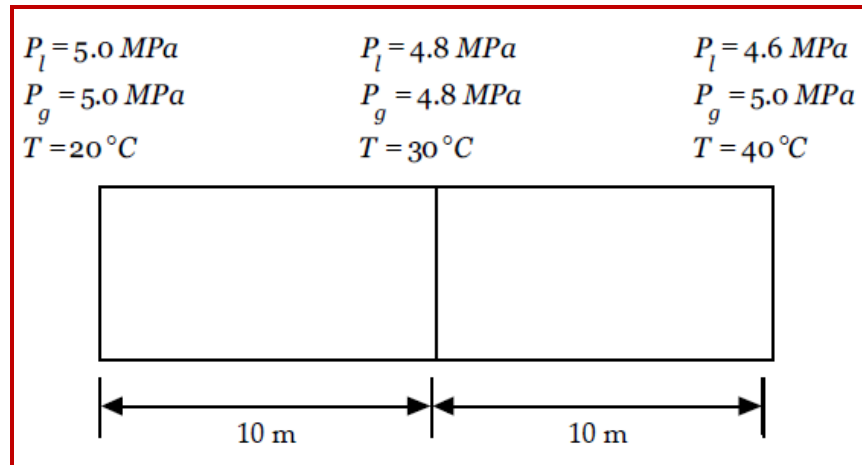


Figure 6-5 Problems Schematic

The list of processes simulated in this problem include: i) Aqueous-gas multifluid flow subject to relative permeability, capillary effects, and phase transition from aqueous saturated to unsaturated; ii) heat transport across multifluid porous media with phase advection and component diffusion; iii) change in CH<sub>4</sub> solubility in water with pressure and temperature; and iv) change in thermodynamic and transport properties with pressure and temperature.

**Simulation Results Comparison.** The results using THCM-hydrate code (i.e. the program developed in this project) are compared against the outputs from the other seven codes (i.e. HydrateResSim, MH-21, stars-Mehran, STARS, STOMP-HYD, TOUGH-FX, Univ-Houston). The main comparisons are presented below in Figure 6.6 to 6.7 for the following time of analyses: day 1, day 10, day 100, day 1000, and day 10000. The comparisons are very satisfactory. Just some slight differences in terms of gas pressure are observed at the earliest stages of the analyses.

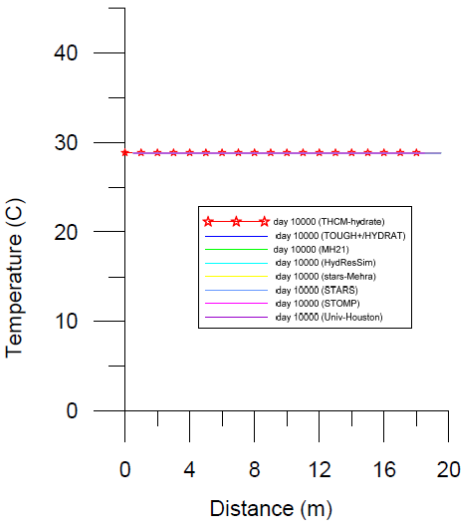
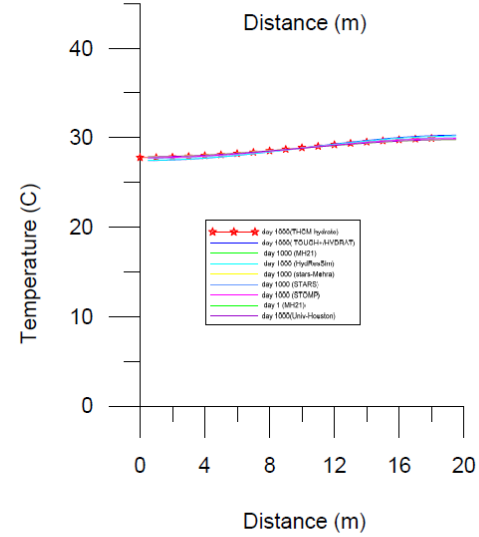
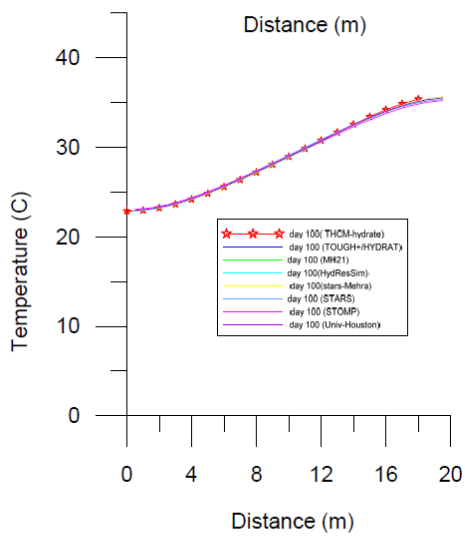
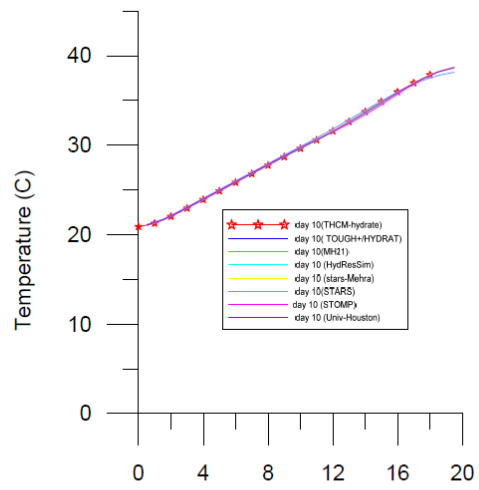
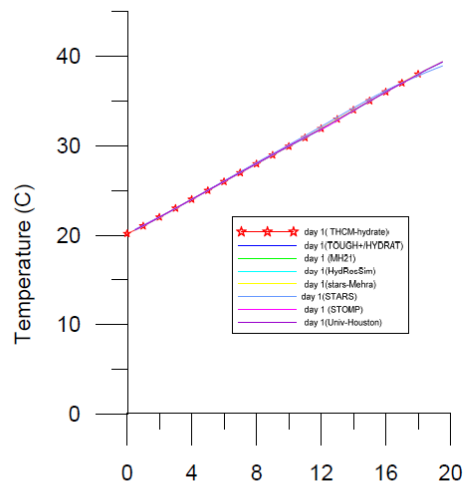


Figure 6-6 Temperature comparisons

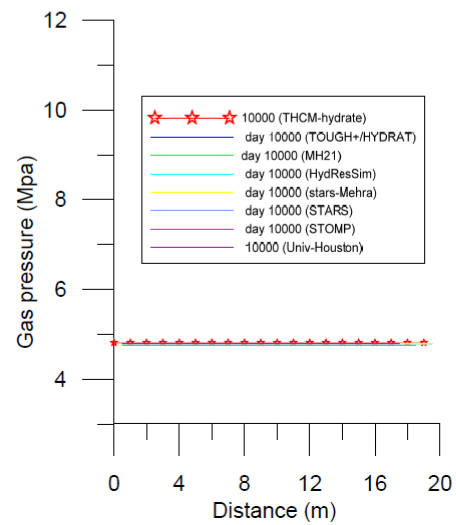
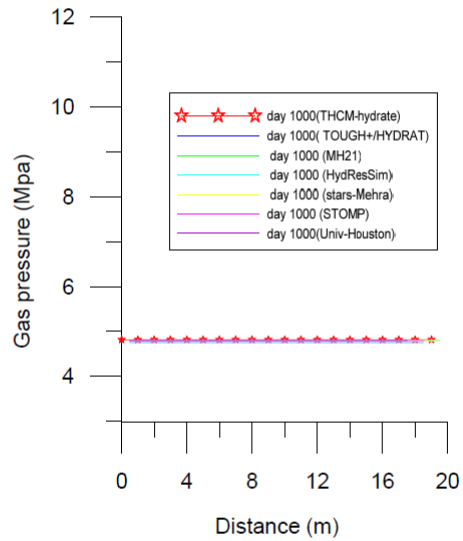
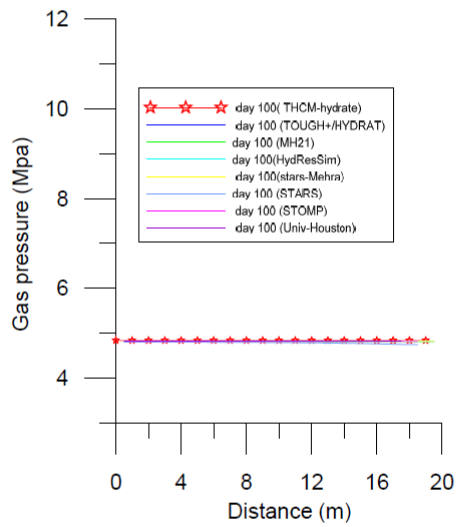
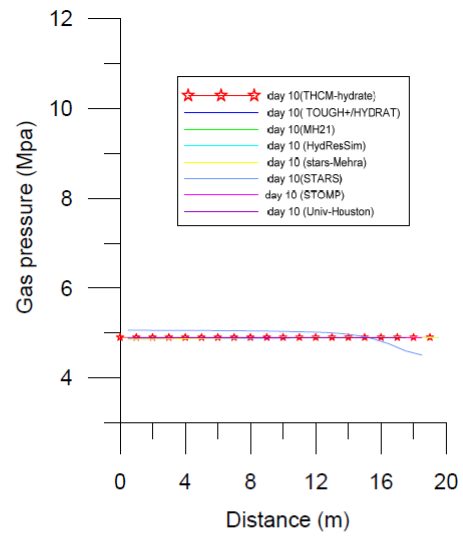
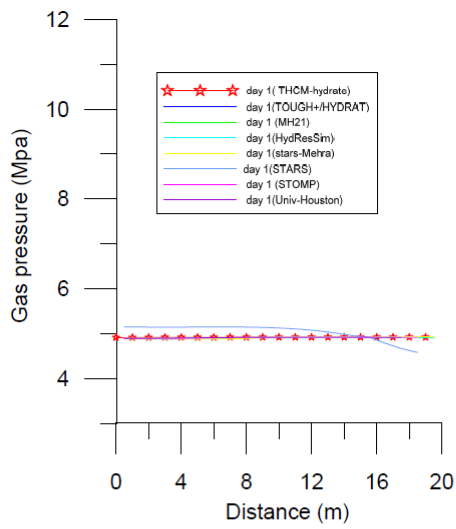


Figure 6-7 Gas pressure comparisons

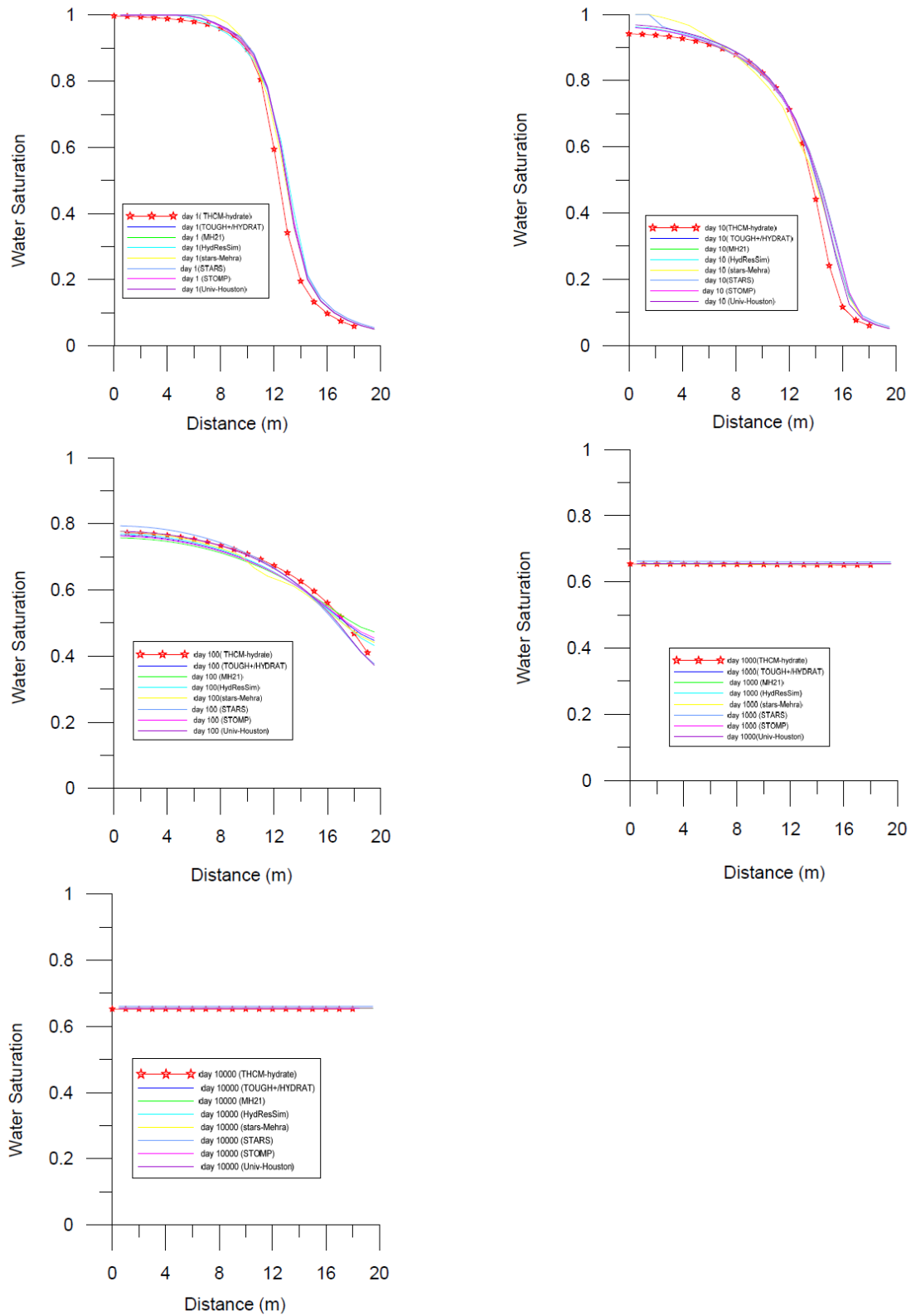
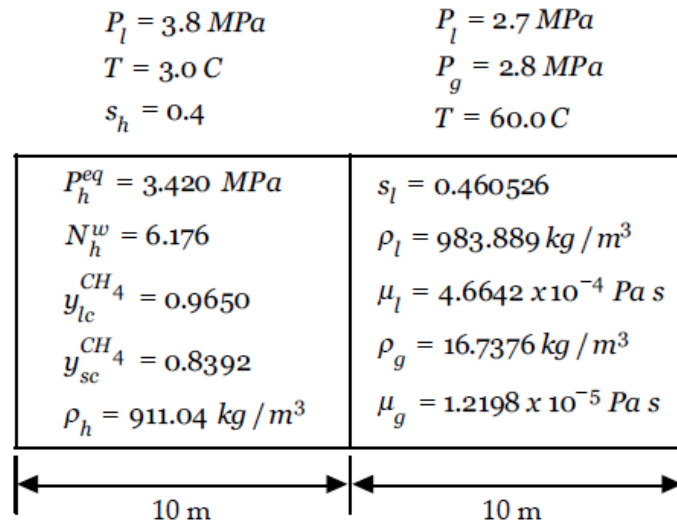


Figure 6-8 Water saturation comparisons

### 6.3. Benchmark Test 2

This case is related to the analysis of “Closed-Domain Hydrate Dissociation (Base Case w/ Hydrate)”. Below a short description of this case is introduced.

*One half is initialized with aqueous-hydrate conditions; whereas, the other half of the domain is initialized with gas-aqueous conditions. As with the ‘Base Case problem’, a closed horizontal domain is used to eliminate gravitational body forces and boundary condition effects. To initialize the aqueous-hydrate half of the domain, temperature, pressure, and hydrate saturation are specified. To initialize the gas aqueous half of the domain temperature, aqueous pressure and gas pressure are specified. All active phases are assumed to comprise water and CH<sub>4</sub>, and capillarity is assumed between the active phases. Hydrate dissociation is assumed to occur using equilibrium kinetics (i.e., infinitely fast dissociation rates). From the specified initial conditions, the simulations proceeds to equilibrium conditions in temperature and pressure, dissociating the hydrate during the transition process and leaving gas-aqueous conditions. A schematic of the initial conditions for the problem are shown in Figure 6.9. The list of processes simulated in this problem include: i) multifluid flow for an aqueous-gas-hydrate system in geological media, subject to relative permeability and capillarity effects and phase transitions; ii) dissociation of CH<sub>4</sub> hydrate in response to thermal stimulation and depressurization; iii) heat transport across multifluid geological media with phase advection and component diffusion; iv) change in CH<sub>4</sub> solubility in water with pressure and temperature; and v) change in thermodynamic and transport properties with pressure and temperature.*



**Figure 6-9** Schematic representation as reported in Benchmark #2

Figure 6.10, 6.11 and 6.12 present the comparisons between the simulators that took part of the benchmark (i.e. HydrateResSim, MH-21, stars-Mehran, STARS, STOMP-HYD, TOUGH-FX, Univ-Houston) and ‘*THCM-hydrate*’ in terms of temperature, gas pressure and hydrate saturation, respectively. The results with symbols correspond to *THCM-hydrate*. The performance of *THCM-hydrate*’ can be considered very satisfactory, there are some slight differences, but the main patterns of the system behavior are well captured by the model. More details about this case can be found in the webpage with the benchmarks results (<http://www.netl.doe.gov/research/oil-and-gas/methane-hydrates/mh-codecompare>).

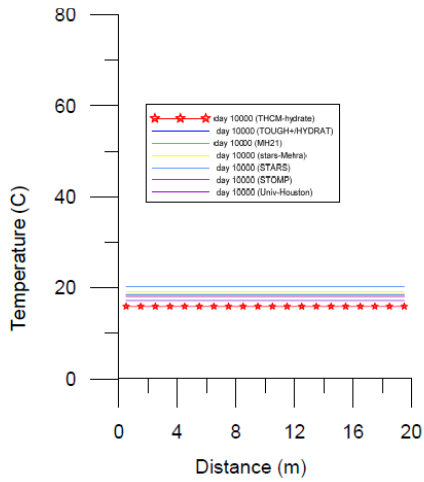
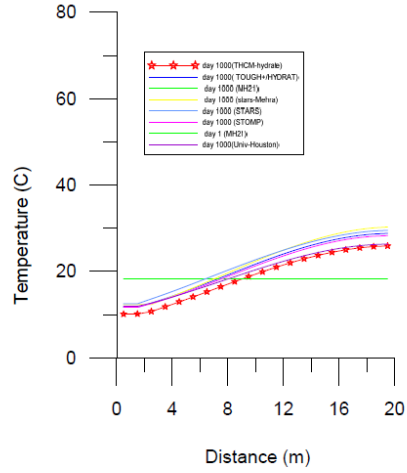
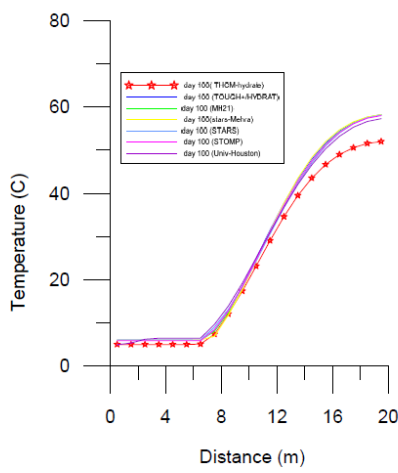
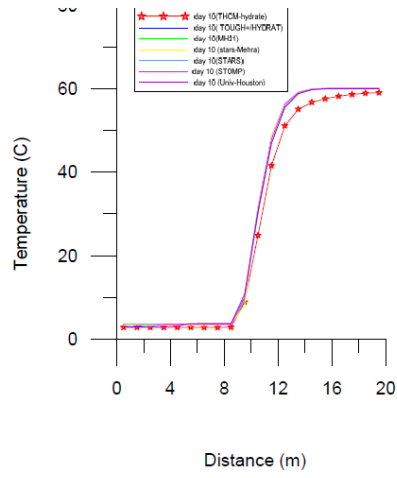
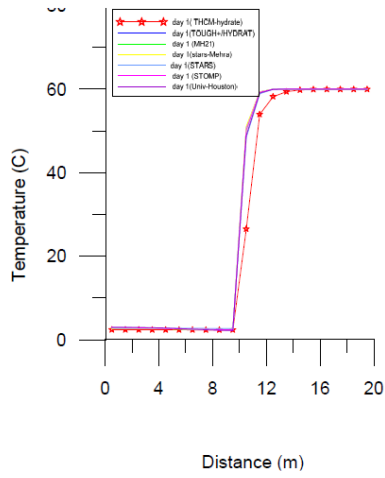


Figure 6-10 Simulators results comparisons in terms of temperature

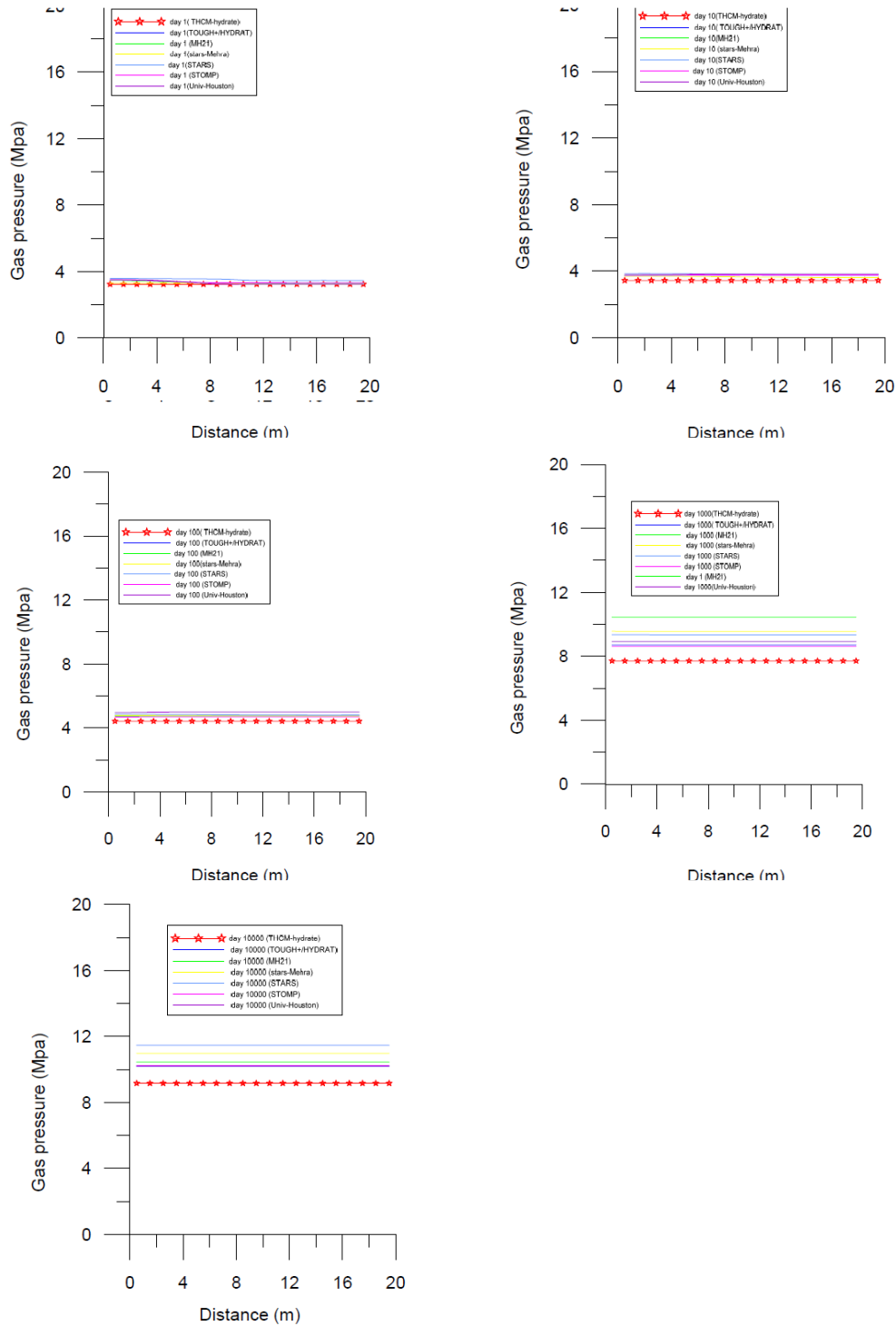


Figure 6-11 Simulators results comparisons in terms of gas pressure

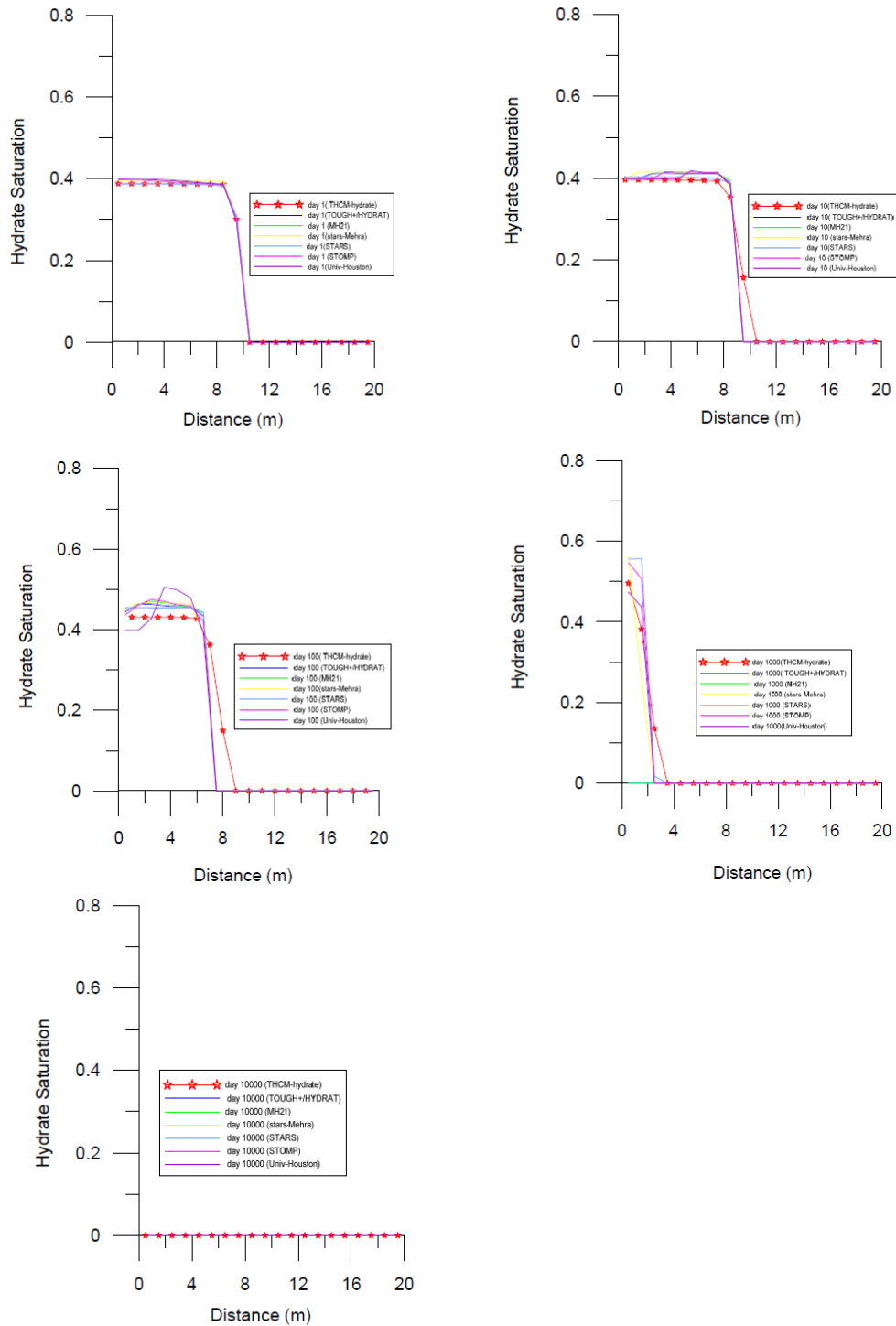


Figure 6-12 Simulators results comparisons in terms of  $S_H$

## 7. SUMMARY AND CONCLUSIONS

In this project a general mathematical formulation has been developed further to analyze coupled THCM problems involving gas hydrate bearing sediments. It is a truly coupled formulation that incorporates the different phases (including solid, liquid, gas, hydrate and ice) and species (i.e., water, methane, solutes and minerals) with the associated phases physical properties and evolutions laws. It also takes into consideration thermal processes (i.e., conduction, phase transformation), hydraulic processes (i.e., multiphase multicomponent flow), effective-stress dependent sediment response, and presence of solutes (e.g. salts), as well as changes in sediment properties in the presence of hydrates. The formulation has been implemented in CODE\_BRIGHT, an existing fully coupled multiphysics 3-D finite element program for geological media. The constitutive models for hydrate bearing sediments are key components of the proposed approach. Tailored constitutive laws for HBS associated with the hydraulic, thermal and mechanical problems that consider the multicomponent structure of hydrate bearing soils have been implemented in the upgraded numerical code THCM-hydrate.

Particular emphasis has been placed in the development of a new geomechanical model able to simulate the complex behavior of HBS during loading and hydrate dissociation. Experimental observations have shown that the presence of hydrates impacts on different aspects of sediment behavior, amongst others: stiffness, peak stress, softening behavior and dilation. It has been observed that these features of soil behavior depend on hydrate saturation as well. Hydrates also contribute to the mechanical stability of the sediment. Furthermore, during dissociation important changes in the mechanical behavior of HBS and soil structure have been observed. The model proposed in this research encompasses different inelastic mechanisms to describe these complex features of HBS behavior. The concept of stress partition was incorporated into the model to estimate the mechanical contribution associated with hydrates and soil skeleton at different stages of loading and hydrate dissociation. A damage model was adopted to describe the behavior of hydrate during loading, while the HISS elastoplastic model was selected for the sediment skeleton. The HISS model is a versatile mechanical constitutive law based on critical state soil mechanics. The proposed framework also incorporates sub-loading and hydrate enhancement mechanisms. Information from several mechanical tests recently published was selected to study the model capabilities. The experiments were chosen to cover the most relevant conditions related to HBS behavior. The effect of hydrate morphology and confinement on the mechanical behavior of HBS was also investigated in this project. Particularly attention was paid to the study of the mechanical behavior of HBS during hydrate dissociation under loading. In the cases in which there was enough experimental data, some tests were used for determining the parameters and the other ones were left apart for model validation.

A database compiling the main published data related to hydrate bearing sediments was developed in this project using the Math-cad software. This IT tool compiles the main constitutive equations proposed for the thermo, hydraulic and mechanical problems; including their dependences on temperature, fluids pressures, stresses and water chemistry. The database also incorporates the phase laws and phase boundaries (including mixed gases) associated with *HBS*. The main model parameters and their typical range of variation are key components of the database as well.

Another significant component of this research was the proposal of analytical solutions associated with steady state analyses involving gas production from HBS. The proposed solutions considered different type of reservoirs and material properties, as well as different

initial and boundary conditions. These types of solutions are very relevant because they correspond to limit conditions of the problems under consideration. For example, analytical solutions related to gas production from HBS will inform about the extent of the dissociated region in the reservoir and the associated maximum amount of gas that can be produced from it. These types of solutions are also instrumental to validate numerical codes.

The proposed numerical framework was verified against both: already published analytical solutions and also new ones developed in this project. The numerical code was also validated against: i) published experimental data; ii) simple, yet rigorous, benchmarks in the pressure-temperature ( $P$ - $T$ ) plane suggested in this research; and iii) some of the benchmark cases proposed in the DOE ‘Methane hydrate Reservoir Simulator Code Comparison Study’.

Some highlights from this research are listed as follows:

- THCM-hydrate: a robust fully coupled and efficient formulation for HBS incorporating the fundamental physical and chemical phenomena that control the behavior of gas hydrates bearing sediments has been developed and validated.
- THCM-hydrate: properly captures the complex interaction between water and gas, and kinetic differences between ice and hydrate formation. Therefore, it permits exploring the development of phases along the various  $P$ - $T$  trajectories that may take place in field situations.
- Results show the pronounced effect of hydrate dissociation on pore fluid pressure generation, and the consequences on effective stress and sediment response. Conversely, the model shows that changes in effective stress can cause hydrate instability.
- The proposed new geomechanical model was capable of capturing not only the main trends and features of sediment observed in the different tests, but also to reproduce very closely the experimental observations in most of the analyzed cases.
- The enhancement of sediment strength, stiffness and dilation induced by the presence of the hydrates were well reproduced by the model.
- The ability of the proposed mechanical model to simulate the volumetric soil collapse compression observed during hydrate dissociation at constant stresses is particularly remarkable. This is a key contribution of this research in relation to the geomechanical modeling of HBS during dissociation.
- The mechanical model has also assisted to interpret how sediment and hydrates contribute to the mechanical behavior of HBS and how these contributions evolve during loading and hydrates dissociation.
- The analytical solutions show the interplay between the variables: relative sediment permeabilities  $k_{sed}/k_{hbs}$ , the leakage in the aquifer  $k'/k_{sed}$ , relative pressure dissociation  $(h^* - h_w)/(h_{far} - h^*)$  and a geometrical ratio  $H b/r_w^2$ .
- At steady-state conditions, the pressure distribution in radial flow is inversely proportional to the logarithm of the radial distance to the well. Therefore there is a physical limit to the zone around a well that can experience pressure-driven dissociation.
- The results reflect the complexity of gas recovery from deep sediments included limited affected zone, large changes in effective stress and associated reductions in permeability.

- THCM-hydrate simulation results compare favorably with published results with well-defined boundary conditions; this corroborates the validity of the implementation.
- THCM-hydrate relevance: resource recovery, environmental implications, seafloor instability

## 8. RELATED ACTIVITIES

### Training of Highly Qualified Personnel:

- Dr. Ajay Shastri (2014). Thesis: “Advanced Coupled THM Analysis in Geomechanics” (TAMU)
- Mr. Xuerui (Gary) Gai (current). Thesis: “Geomechanical modeling of HBS” (TAMU)
- Dr. Marco Terzariol (2014). Theme: “Hydrates Bearing Sediments–Field and Laboratory Characterization”. Current Position: Post-Doctoral Fellow, KAUST
- Mr. Mehdi Teymouri (current). Thesis: “Gas production from HBS” (TAMU)
- Mr. Zhonghao Sun (current). Thesis “Analytical solution for HBS” (GT – KAUST)’
- Mr. Bohan Zhou (current). Thesis: “Permafrost behavior”. (TAMU)

### Special Events

The following events were co-organized in the context of the conducted research.

- HBS Sessions Organized at American Geophysical Union (AGU) Events
  - “Session ID 12884: Hydrate bearing sediments: characterization, modeling, and thermal, hydrological, and geomechanical behavior”. AGU Fall 2016 Meeting, Dec. 2016, San Francisco. Conveners: Jeen-Shang Lin (Univ. of Pittsburgh), Yongkoo Seol (NETL, DOE), Marcelo Sánchez (TAMU) and Steve Phillips (The Univ. of Texas, Austin).
  - “Session ID 7432: Hydrate bearing sediments: characterization, modeling and implications on geohazard and gas production”. AGU Fall 2015 Meeting, Dec. 2015, San Francisco. Conveners: Jeen-Shang Lin (Univ. of Pittsburgh), Yongkoo Seol (NETL, DOE), Timothy Kneafsey (Berkeley National Lab), and Marcelo Sánchez (TAMU).
  - “Session ID 1457: Hydrate bearing soils: characterization, modeling and geomechanical implications”. AGU Fall 2014 Meeting, Dec. 2014, San Francisco. Conveners: Jeen-Shang Lin (University of Pittsburgh), Yongkoo Seol (NETL, DOE), Timothy Kneafsey (Berkeley National Lab), and Marcelo Sánchez (TAMU)
- HBS Sessions Organized at International Events
  - Mini-Symposium: “Geomechanical characterization and modeling of hydrate bearing sediments”. 1st International Conference on Energy Geotechnics. Kiel, Germany. 29-31 Aug. 2016. Organizers: Marcelo Sánchez (TAMU) and Christian Deusner (GEOMAR).
- Sessions Organized at National and International Events (involving HBS)
  - Technical Session B21: “Energy Geotechnics”. 2016 Geo-Chicago: Sustainability, Energy, and the Geoenvironment. August 14-18 2016. Organizers: Marcelo Sánchez (TAMU) and Xinbao Yu (Univ. of Texas at Arlington).
  - Technical Track: “Geo-Engineering for Energy and Sustainability”. XV Pan-American Conference on Soil Mechanics and Geotechnical Engineering. Buenos Aires, Argentina. 15-18 Nov. 2015. Track consists of three components: a Keynote

Lecture, a Panel Session and two Technical Sessions. Organizers: Marcelo Sánchez (TAMU), Guillermo Narsilio (The Univ. of Melbourne, Australia), Jose Alvarellos (Repsol Oil Company, Spain) and Leonardo Guimarães (Univ. Federal de Pernambuco, Brazil).

#### **Conference Proceeding Books and Journal Themed Issues - Invited Editor**

- Journal ‘Energy Geotechnics’. Proceedings of the 1<sup>st</sup> International Conference on Energy Geotechnics. Kiel, Germany. 29-31 Aug. 2016. CRC Press/Balkema. ISBN 978-1-138-03299-6. Editors: Wuttke F, Bauer S. and Sánchez M. (2016).
- Journal ‘Environmental Geotechnics’. Special Issue ‘Selected Papers XV Pan-American Conference on Soil Mechanics and Geotechnical Engineering’. ICE Thomas Telford (in print). Guest Editors: Narsilio G., Sánchez M., and Guimarães, L. (7 papers)
- ‘Journal of Geomechanics for Energy and the Environment’. Themed Issue on Selected Papers SEG2015 - Part I, Volume 6, June 2016 (8 papers). Guest Editors: Marcelo Sánchez & Enrique Romero.
- ‘Journal of Geomechanics for Energy and the Environment’. Themed Issue on Selected Papers SEG2015 - Part II’, Volume 8, December 2016 (7 papers). Guest Editors: Enrique Romero & Marcelo Sánchez.

#### **Articles in Refereed Archival Journals (published and in-print)**

- McCartney J., Sánchez M., Tomac I. (2016). ‘Energy Geotechnics: Advances in Subsurface Energy Recovery, Storage, Exchange, and Waste Management’. *Computers and Geotechnics*. doi:10.1016/j.compgeo.2016.01.002.
- Shin, H. and Santamarina J.C. (2016). ‘Sediment–well interaction during depressurization’. *Acta Geotechnica*. doi:10.1007/s11440-016-0493-.
- Sánchez M., Gai X., Santamarina J.C. ‘A Constitutive Mechanical Model for Gas Hydrate Bearing Sediments Incorporating Inelastic Mechanisms’. *Computers and Geotechnics* 84 (2017) 28–46. Doi: /10.1016/j.compgeo.2016.11.012
- Chong, S.H. and Santamarina J.C. (2016). ‘Soil Compressibility Models for Wide Stress Range’. *Journal of Geotechnical and Geoenvironmental Engineering*, ASCE vol. 142(6), doi: 10.1061/(ASCE)GT.1943-5606.0001482, 06016003.
- Gai X., Sánchez M. (2016). ‘A Geomechanical Model for Gas Hydrate Bearing Sediments’. *Environmental Geotechnics* (in print), doi: 10.1680/jenge. 15-00050.
- Sánchez M., Flacao F., Mack M., Pereira J-M., Narsilio G., Guimarães L. (2016). “Salient Comments and Discussions from a Geo-Energy Panel”. *Environment Geotechnics*. doi: 10.1680/jenge.16.00008.

#### **Articles in Refereed Archival Journals (under review and under preparation)**

- Terzariol, M., Goldsztein, G. and Santamarina J.C., ‘Maximum Recoverable Gas from Hydrate Bearing Sediments by Depressurization’. Submitted for publication.

- Ren, X-W. and Santamarina, J.C., ‘Hydraulic Conductivity in Sediments’. Submitted for publication.
- Shastri, A., Sánchez, M., Moo, L., Thomas Dewers, T. Mechanical behavior of frozen soils: experimental investigation and constitutive modeling/ Submitted for publication.
- Four more articles are being prepared to be submitted soon for publication in refereed archival journals

### Conference and Workshop Contributions

- Sánchez M, Gai X. Geomechanical and numerical modeling of gas hydrate sediments. In: Wuttke, Bauer, Sanchez, editors. *1<sup>st</sup> International Conference on Energy Geotechnics*, Kiel, Germany. Energy Geotechnics. CRC Press/Balkema; 2016. 19–24
- Gai X., Sánchez M. Geomechanical Modeling of Gas Hydrate Bearing Sediments (Poster). *2015 AGU Fall Meeting*, San Francisco, USA, 14<sup>th</sup> to 18<sup>th</sup> Dec 2015.
- Gai X, Sánchez M. (2015). “Mechanical Modeling of Gas Hydrate Bearing Sediments Using an Elasto-Plastic Framework”. *XV Panamerican Conference on Soil Mechanics and Geotechnical Engineering*, Buenos Aires, Argentina 15<sup>th</sup> to 18<sup>th</sup> Nov. 2015.
- Sánchez M., Santamarina J.C., Shastri A., and Gai X, (2015). Numerical Modeling of Gas Hydrate Bearing Sediments. *XVI ECSMGE European Conference on Soil Mechanics and Geotechnical Engineering*, Edinburgh, UK, 13<sup>th</sup> to 17<sup>th</sup> Sep. 2015.
- Sánchez M., Shastri A., Santamarina J.C. and Gai X. (2014). Coupled Modeling of Gas Hydrate Bearing Sediments. *14<sup>th</sup> International Conference of the International Association for Computer Methods and Advances in Geomechanics, 14<sup>th</sup> IACMAG*. Kyoto, Japan. 22<sup>nd</sup> to 25<sup>th</sup> Sep 2014.
- Sánchez M., Gai X, Shastri A.,and Santamarina J.C. Coupled THCM Modeling of Gas Hydrate Bearing Sediments (Poster). *2014 AGU Fall Meeting*, San Francisco, USA, 15<sup>th</sup> to 19<sup>th</sup> Dec 2014.
- Sánchez M., Santamarina J.C., Shastri A., and Gai X. Numerical THCM Modeling of HBS Using a Truly Coupled Approach (Poster). *Gordon Research Conference on Natural Gas Hydrate Systems*. Galveston, US. 23<sup>rd</sup> to 28<sup>th</sup> Mar 2014.

### Newsletter Contributions

- Sánchez M., Santamarina J.C., Gai X, Teymouri M., and Shastri A. (2016). “Coupled Thermo-Hydro-Chemo-Mechanical (THCM) Models for Hydrate-Bearing Sediments”. *Fire in the Ice*, a DOE quarterly publication highlighting the latest developments in international gas hydrates R&D. Vol 16(1) 12-17. <http://www.netl.doe.gov/research/oil-and-gas/methane-hydrates/fire-in-the-ice>

### Presentations

- Numerical Modeling of Gas Hydrate Bearing Sediments, L. "Corky" Frank '58 Graduate Seminar Series, Petroleum Eng. Texas A&M Univ., Set. 2016 (M. Sánchez).

- The Energy Tera Problem: Needed Geo-centered Solutions. Keynote lecture, 1<sup>st</sup> International Conference on Energy Geotechnics - ICEG 2016, Kiel, Aug 2016. (J.C. Santamarina).
- Geomechanical and Numerical Modeling of Gas Hydrate Bearing Sediments. Keynote lecture, 1<sup>st</sup> International Conference on Energy Geotechnics - ICEG 2016, Kiel, Aug 2016. (M. Sánchez).
- Geomechanical and Coupled THMC Numerical Modeling of Complex Geo-Energy Problems. Pontifical University of Chile, Santiago, Chile, Aug. 2016 (M. Sánchez).
- Mechanical and Numerical Modeling of Gas Hydrate Bearing Sediments. IV International Workshop on Modern Trends in Geomechanics. G. Viggiani, D. Salciarini, F. Silvestri, C. Tamagnini, G.M.B. Viggiani (Eds) Assisi, Italy. May 2016. (M. Sánchez).
- Energy Resources, Use, Conservation & Efficiency – Pending questions. Emirates Energy Efficiency Summit, Dubai, Feb 2016. (J.C. Santamarina).
- Coupled THMG Analysis in Geomechanics Incorporating Solid Phase Transformations. KAUST Athenaeum on Dissolution and Precipitation: Implications for Energy Geo-Engineering. King Abdullah University of Science and Technology, Saudi Arabia, Feb 2016 (M. Sánchez).
- THMC Coupled Modeling in Geo-Energy. The University of Texas at Austin, Austin, USA, Oct. 2015 (M Sánchez )
- Coupled THMC Modeling of Hydrate Bearing Sediments. École Polytechnique Fédérale de Lausanne (EPFL), Switzerland, Aug. 2015 (M. Sánchez).
- Methane hydrates, International Symposium on Energy Geotechnics Barcelona, Spain. Jun 2015, (J.C. Santamarina).
- Coupled THMC model of complex soils. Northwestern University, Evanston, USA, Dec 2014 (M. Sánchez)).
- Pressure Core Technology, AGU San Francisco, USA. Dec 2014 (J.C. Santamarina).
- Coupled THMC Modeling of gas Hydrates Sediments.: SES Annual Technical Meeting. Purdue University, US. Oct 2014 (M. Sánchez).
- Pressure Core Characterization, KIGAM, S. Korea, Jul 2014 (J.C. Santamarina).
- THMC Coupled Analysis involving Gas Hydrates Sediment. University of Pittsburgh, Pittsburgh, USA, Jan. 2014 Pittsburgh (M. Sánchez).
- Energy: A Geo-Centered Perspective, University of Texas, Austin. Oct 2013 (J.C. Santamarina).

## 9. REFERENCES

- Aman, Z. M., Leith, W. J., Grasso, G. A., Sloan, E. D., Sum, A. K., & Koh, C. A. (2013). Adhesion force between cyclopentane hydrate and mineral surfaces. *Langmuir*, 29(50), 15551-15557.
- Anderson, B. J., Wilder, J. W., Kurihara, M., White, M. D., Moridis, G. J., Wilson, S. J., Pooladi-Darvish, M., Masuda, Y., Collett, T. S., and Hunter, R. (2008). Analysis of modular dynamic formation test results from the Mount Elbert 01 stratigraphic test well, Milne Point Unit, North Slope, Alaska. *6<sup>th</sup> International Conference on Gas Hydrates (ICGH 2008) Vancouver, British Columbia, Canada*.
- Bear J. (1979). *Hydraulics of groundwater McGraw-Hill Inc.* ISBN 0-07-004170-9.
- Berge LI, Jacobsen KA, Solstad A. (1999). Measured acoustic wave velocities of R11 (CC13F) hydrate samples with and without sand as a function of hydrate concentration. *Journal of Geophysical Research: Solid Earth* (1978–2012); 104(B7):15415-15424.
- Boswell, R., and Collett, T. S. (2011). Current perspectives on gas hydrate resources. *Energy & Environmental Science*, 4(4), 1206-1215.
- Briaud, J. L., and Chaouch, A. (1997). Hydrate melting in soil around hot conductor. *Journal of geotechnical and geoenvironmental engineering*, 123(7), 645-653.
- Carol I, Rizzi E, Willam K. (2001). On the formulation of anisotropic elastic degradation. I. Theory based on a pseudo-logarithmic damage tensor rate. *Int. Journal of Solids and Structures*;38(4):491-518.
- Chaouachi M, Falenty A, Sell K, Enzmann F, Kersten M, Haberthür D, et al. (2015). Microstructural evolution of gas hydrates in sedimentary matrices observed with synchrotron X - ray computed tomographic microscopy. *Geochemistry, Geophysics, Geosystems*;16(6):1711-1722.
- Chatti I, Delahaye A, Fournaison L, Petitot J-P (2005). Benefits and drawbacks of clathrate hydrates: a review of their areas of interest. *Energy conversion and management*; 46:1333–1343.
- Clayton, C., Priest, J., & Rees, E. (2010). The effects of hydrate cement on the stiffness of some sands. *Geotechnique*, 60(6), 435-445.
- Cortes, D. D., Martin, A. I., Yun, T. S., Francisca, F. M., Santamarina, J. C., and Ruppel, C. (2009). Thermal conductivity of hydrate-bearing sediments. *J. Geophys. Res*, 114, B11103.
- Dai, S., & Santamarina, J. C. (2013). Water retention curve for hydrate-bearing sediments. *Geophysical Research Letters*, 40(21), 5637-5641.
- Dai J, Xu H, Snyder F, Dutta N. (2004). Detection and estimation of gas hydrates using rock physics and seismic inversion: Exam. from the northern deepwater Gulf of Mexico. *The Leading Edge*;23(1):60-66.
- Dallimore, S. R., Wright, J. F., Nixon, F. M., Kurihara, M., Yamamoto, K., Fujii, T., Fujii, K., Numasawa, M., Yasuda, M., Imasato, Y. Geologic and porous media factors affecting the 2007 production response characteristics of the JOGMEC/NRCAN/AURORA Mallik Gas Hydrate Production Research Well. *Proc., Proceedings of the Int. Conference on Gas Hydrates (ICGH 2008)*, 10.
- De Glee, G. (1951). Berekeningsmethoden voor de winning van grondwater. *Drinkwatervoorziening, 3e Vacantiecursus*, 38-80.
- Desai CS. (2000). *Mechanics of materials and interfaces: The disturbed state concept: CRC press*, 2000.
- Desai C. (1989). Letter to editor single surface yield and potential function plasticity models: A review. *Computers and Geotechnics*;7(4):319-333.
- Desai C, Somasundaram S, Frantziskonis G. (1986). A hierarchical approach for constitutive modelling of geologic materials. *Int. Jnl. for Numerical and Analytical Methods in Geomechanics*. 10(3):225-257.
- Dickens, G. R., Paull, C. K., and Wallace, P. (1997). Direct measurement of in situ methane quantities in a large gas-hydrate reservoir. *Nature*, 385, 426-428.
- Duncan JM, Chang C-Y. (1970). Nonlinear analysis of stress and strain in soils. *Journal of Soil Mechanics & Foundations Div.* 1970.
- Dvorkin J, Uden R. (2004). Seismic wave attenuation in a methane hydrate reservoir. *The Leading Edge*;23(8):730-732.
- Esmailzadeh F., Zeighami M., Kaljahi J. (2011). 1D Mathematical Modeling of Hydrate Decomposition in Porous Media by Depressurization and Thermal Stimulation. *Jnl. of Porous Media*, 14(1).

- Fernandez A, Santamarina J. (2001). Effect of cementation on the small-strain parameters of sands. *Canadian Geotechnical Journal*. 38(1):191-199.
- Gai, X., and Sánchez, M. (2016.). Mechanical Modeling of Gas Hydrate Bearing Sediments Using an Elasto-Plastic Framework. Paper presented at the XV Panamerican Conference on Soil Mechanics and Geotechnical Engineering, Buenos Aires, Argentina
- Garg S, Pritchett J, Katoh A, Baba K. & Fujii T (2008). A mathematical model for the formation/dissociation of methane hydrates in the marine environment. *Journal of Geophysical Research*; 113:B01201.
- Gens A., and Olivella S. (2001). THM phenomena in saturated and unsaturated porous media. *Revue française de génie civil*, 5(6), 693-717.
- Goel, N., Wiggins, M., and Shah, S. (2001). Analytical modeling of gas recovery from in situ hydrates dissociation. *Journal of Petroleum Science and Engineering*, 29(2), 115-127.
- Guimarães, L. do N., Gens, A. Olivella, S. (2007). Coupled thermo-hydro-mechanical and chemical analysis of expansive clay subjected to heating and hydration. *Transport in porous media*, 66, 341-372.
- Gupta, A., Kneafsey, T. J., Moridis, G. J., Seol, Y., Kowalsky, M. B., and Sloan Jr, E. (2006). "Composite thermal conductivity in a large heterogeneous porous methane hydrate sample." *The Journal of Physical Chemistry B*, 110(33), 16384-16392.
- Hancock, S., Collett, T., Dallimore, S., Satoh, T., Inoue, T., Huenges, E., Hennings, J., and Weatherill, B. (2005). Overview of thermal-stimulation production-test results for the JAPEx/JNOC/GSC
- Hashiguchi K. (1977). Elasto-plastic constitutive laws of granular materials, Constitutive Equations of Soils. *Proc Spec Session 9 of 9<sup>th</sup> Int ICSMFE*. 1977:73-82.
- Helgerud M, Dvorkin J, Nur A, Sakai A, Collett T. (1999). Elastic - wave velocity in marine sediments with gas hydrates: Effective medium modeling. *Geophysical Research Letters*. 1999;26(13):2021-2024.
- Hong, H., and Pooladi-Darvish, M. (2005). Simulation of depressurization for gas production from gas hydrate reservoirs. *Journal of Canadian Petroleum Technology*, 44(11), 39-46.
- Hong, H., Pooladi-Darvish, M., and Bishnoi, P. (2003). Analytical modelling of gas production from hydrates in porous media. *Journal of Canadian Petroleum Technology*, 42(11), 45-56.
- Hyodo M, Li Y, Yoneda J, Nakata Y, Yoshimoto N, Nishimura A. (2014). Effects of dissociation on the shear strength and deformation behavior of methane hydrate-bearing sediments. *Marine and Petroleum Geology*; 51:52-62.
- Hyodo M, Nakata Y, Yoshimoto N, Ebinuma T. (2005). Basic research on the mechanical behavior of methane hydrate-sediments mixture. *Soils and foundations*. 2005;45(1):75-85.
- Hyodo M, Yoneda J, Yoshimoto N, Nakata Y. (2013). Mechanical and dissociation properties of methane hydrate-bearing sand in deep seabed. *Soils and foundations*. 2013;53(2):299-314.
- Jamaluddin A, Kalogerakis N & Bishnoi P (1991). Hydrate plugging problems in undersea natural gas pipelines under shutdown conditions. *J. Petroleum Science and Engineering*; 5:323-335
- Jang, J., and Santamarina, J. C. (2011). Recoverable gas from hydrate- bearing sediments: Pore network model simulation and macroscale analyses. *Journal of Geophysical Research: Solid Earth*, 116(B8).
- Ji, C., Ahmadi, G., and Smith, D. H. (2001). Natural gas production from hydrate decomposition by depressurization. *Chemical Engineering Science*, 56(20), 5801-5814.
- Jiang, M., Chen, H., Tapias, M., Arroyo, M., & Fang, R. (2014). Study of mechanical behavior and strain localization of methane hydrate bearing sediments with different saturations by a new DEM model. *Computers and Geotechnics*, 57, 122-138.
- Jiang, M., Zhu, F., & Utili, S. (2015). Investigation into the effect of backpressure on the mechanical behavior of methane-hydrate-bearing sediments via DEM analyses. *Computers and Geotechnics*, 69, 551-563.
- Kachanov L, Krajcinovic D. (1987). Introduction to continuum damage mechanics.. *Springer Science & Business Media*, 2013.
- Kamath, V., and Godbole, S. (1987). Evaluation of hot-brine stimulation technique for gas production from natural gas hydrates. *Journal of petroleum technology*, 39(11), 1379-1388.

- Kayen, R. E., and Lee, H. J. (1991). Pleistocene slope instability of gas hydrate-laden sediment on the Beaufort sea margin. *Marine Georesources & Geotechnology*, 10(1-2), 125-141.
- Kim, H., Bishnoi, P., Heidemann, R., and Rizvi, S. (1987). Kinetics of methane hydrate decomposition. *Chemical engineering science*, 42(7), 1645-1653.
- Kimoto S, Oka F, Fushita T, Fujiwaki M. (2007). A chemo-thermo-mechanically coupled numerical simulation of the subsurface ground deformations due to methane hydrate dissociation. *Computers and Geotechnics*;34(4):216-228.
- Klar, A., Soga, K., & Ng, M. Y. A. (2010). Coupled deformation–flow analysis for methane hydrate extraction. *Geotechnique*, 60(10), 765-776
- Klar, A., Uchida, S., Soga, K., and Yamamoto, K. (2013). Explicitly coupled thermal flow mechanical formulation for gas-hydrate sediments. *SPE Journal*, 18(02), 196-206.
- Konno, Y., Masuda, Y., Hariguchi, Y., Kurihara, M., Ouchi, H. (2010). Key factors for depressurization-induced gas production from oceanic methane hydrates. *Energy & Fuels*, 24(3), 1736-1744.
- Kueper, B. H., & Frind, E. O. (1991). Two- phase flow in heterogeneous porous media: 1. Model development. *Water Resources Research*, 27(6), 1049-1057.
- Kwon, T. H., Cho, G. C., and Santamarina, J. C. (2008). "Gas hydrate dissociation in sediments: Pressure- temperature evolution." *Geochemistry, Geophysics, Geosystems*, 9(3).
- Lasaga, A. C. (1998). *Kinetic theory in the earth sciences*, Princeton Univ Pr.
- Lin JS, Seol Y, Choi JH. (2015). An SMP critical state model for methane hydrate - bearing sands. *International Journal for Numerical and Analytical Methods in Geomechanics*;39(9):969-987.
- Liu, F., Jiang, M., & Zhu, F. (2014). Discrete element analysis of uplift and lateral capacity of a single pile in methane hydrate bearing sediments. *Computers and Geotechnics*, 62, 61-76.
- Masui A, Haneda H, Ogata Y, Aoki K. (2005). Effects of methane hydrate formation on shear strength of synthetic methane hydrate sediments. *The Fifteenth International Offshore and Polar Engineering Conference: International Society of Offshore and Polar Engineers*, 2005.
- Masui A, Miyazaki K, Haneda H, Ogata Y, Aoki K. (2008). Mechanical characteristics of natural and artificial gas hydrate bearing sediments. *Proceedings of the 6th International Conference on Gas Hydrates: Vancouver, Canada: ICGH*, 2008. p. 6-10.
- Minagawa, H., Nishikawa, Y., Ikeda, I., Sakamoto, Y., Miyazaki, K., Takahara, N., Komai, T., and Narita, H. (2008). Relation between permeability and pore-size distribution of methane-hydrate-bearing sediments. *Proceedings from the Offshore Technology Conference*; Houston, Texas; USA
- Miranda CR, Matsuoka T. First-principles study on mechanical properties of CH<sub>4</sub> hydrate. In *Proceedings of the 6th International Conference on Gas Hydrates. Vancouver, Canada*, 2008.
- Miyazaki K, Masui A, Sakamoto Y, Aoki K, Tenma N, Yamaguchi T. (2011). Triaxial compressive properties of artificial methane - hydrate - bearing sediment. *Journal of Geophysical Research: Solid Earth* (1978–2012);116(B6).
- Miyazaki, K., Masui, A., Tenma, N., Ogata, Y., Aoki, K., Yamaguchi, T., & Sakamoto, Y. (2010). Study on mechanical behavior for methane hydrate sediment based on constant strain-rate test and unloading-reloading test under triaxial compression. *Int. Journal of Offshore and Polar Engineering*, 20(01).
- Miyazaki K, Tenma N, Aoki K, Yamaguchi T. (2012). A nonlinear elastic model for triaxial compressive properties of artificial methane-hydrate-bearing sediment samples. *Energies*;5(10):4057-4075.
- Moridis, G., and Collett, T. (2003). Strategies for gas production from hydrate accumulations under various geologic conditions. *Lawrence Berkeley National Laboratory, Berkeley, CA*.
- Moridis, G. J. (2014). TOUGH+ HYDRATE v1. 2 User's Manual: A Code for the Simulation of System Behavior in Hydrate-Bearing Geologic Media. R. LBNL-3185. Lawrence Berkeley Nat. Lab. CA, USA.
- Moridis, G. J., Collett, T., Boswell, R., Kurihara, M., Reagan, M. T., Koh, C., and Sloan Jr, E. D. (2008). Toward production from gas hydrates: current status, assessment of resources, and simulation-based evaluation of technology and potential. *SPE 114163, Keystone, Colo*.
- Moridis, G. J., Collett, T., Pooladi-Darvish, M., Hancock, S., Santamarina, J. C., Boswell, R., Kneafsey, T. J., Rutqvist, J., Kowalsky, M. B., Reagan, M. T., Sloan Jr, E. D., Sum, A. K., and Koh, C. (2011).

- Challenges, uncertainties and issues facing gas production from gas hydrate deposits. *SPE Reservoir Evaluation & Engineering*, 14(1), 76-112.
- Moridis, G. J., and Sloan, E. D. (2007). Gas production potential of disperse low-saturation hydrate accumulations in oceanic sediments. *Energy Conversion and Management*, 48(6), 1834-1849.
- Olivella, S., Carrera, J., Gens, A., and Alonso E.E. (1994). Non-isothermal multiphase flow of brine and gas through saline media. *Transport in porous media*, 15, 271-293.
- Olivella S., Gens A., Carrera J. and Alonso, E.E. (1996). Numerical formulation for a simulator (CODE-BRIGHT) for the coupled analysis of saline media. *Engineering Computations*; 13/7:87-112.
- Pinkert S, Grozic J. (2014). Prediction of the mechanical response of hydrate - bearing sands. *Journal of Geophysical Research: Solid Earth*;119(6):4695-4707.
- Pinkert S, Grozic J, Priest J. (2015). Strain-softening model for hydrate-bearing sands. *International Journal of Geomechanics*;15(6):04015007.
- Pinkert S. (2016). Rowe's Stress-Dilatancy Theory for Hydrate-Bearing Sand. *International Journal of Geomechanics*:06016008.
- Pinyol NM, Vaunat J, Alonso Pérez de Agreda E. (2007). A constitutive model for soft clayey rocks that includes weathering effects. *Geotechnique* 57,(2):137-151.
- Priest, J. A., Rees, E. V., & Clayton, C. R. (2009). Influence of gas hydrate morphology on the seismic velocities of sands. *Journal of Geophysical Research: Solid Earth*, 114(B11).
- Rowe PW. (1962). The stress-dilatancy relation for static equilibrium of an assembly of particles in contact. *Proc. of the Royal Soc. of London. The Royal Society*, 1962. p. 500-527.
- Rutqvist J., Moridis G (2007). Numerical studies of geomechanical stability of hydrate-bearing sediments. *Offshore Technological Conference, Houston, U.S.A.*; 30/04-3/05. OTC 18860.
- Sánchez, M., and Gai, X. (2016). Geomechanical and numerical modeling of gas hydrate sediments. Paper presented at the 1st International Conference on Energy Geotechnics, Kiel, Germany.
- Sánchez, M., Gai, X., & Santamarina, J.C. (2017). A constitutive mechanical model for gas hydrate bearing sediments incorporating inelastic mechanisms. *Computers and Geotechnics*, 84, 28-46.
- Sánchez M., Santamarina JC. (2015). THCM Coupled Model For Hydrate-Bearing Sediments: Data Analysis and Design of New Field Experiments (Marine and Permafrost Settings). *DOE Quarterly Research Performance Progress Report* (Period ending 12/31/2014).
- Sánchez, M., & Shastri, A., Santamarina, J. C. (2013). Modeling gas hydrate bearing sediments using a coupled approach. In *1<sup>st</sup> Pan-American Conference on Unsaturated Soils*.
- Sander, G., Glidewell, O., Norbury, J. (2008). Dynamic capillary pressure, hysteresis and gravity-driven fingering in porous media. *Int. Jnl of Physics: Conference Series*, 138;(1):012023. IOP Publishing.
- Santamarina, J., and Jang, J. (2009). Gas production from hydrate bearing sediments: geomechanical implications. *DOE-NETL Fire in the Ice*, 9(4), 18-22.
- Santamarina JC, Dai S, Jang J, Terzariol M. (2012). Pressure core characterization tools for hydrate-bearing sediments. *Sci Drill*. 2012;14(4).
- Santamarina JC, Dai S, Terzariol M, Jang J, Waite WF, Winters WJ, et al. (2015). Hydro-bio-geomechanical properties of hydrate-bearing sediments from Nankai Trough. *Marine and Petroleum Geology*;66:434-450.
- Santamarina, J.C. and Ruppel, C. (2010). The Impact of Hydrate Saturation on the Mechanical, Electrical and Thermal Properties of Hydrate-Bearing Sands, Silts and Clay, in *Geophysical Characterization of Gas Hydrates, SEG Geophysical Develop. Series*, No. 14, Ed. Riedel, Willoughby, Chopra: 373-384
- Shen, J., Chiu, C., Ng, C. W., Lei, G., Xu, J. (2016). A state-dependent critical state model for methane hydrate-bearing sand. *Computers and Geotechnics*, 75, 1-11.
- Shen, Z., & Jiang, M. (2016). DEM simulation of bonded granular material. Part II: Extension to grain-coating type methane hydrate bearing sand. *Computers and Geotechnics*, 75, 225-243.
- Shen, Z., Jiang, M., & Thornton, C. (2016). DEM simulation of bonded granular material. Part I: Contact model and application to cemented sand. *Computers and Geotechnics*, 75, 192-209.
- Sloan E. D. and Koh C. A. (2008). *Clathrate hydrates of natural gases*, CRC

- Sloan SW. (1987). Substepping schemes for the numerical integration of elastoplastic stress–strain relations. *International Journal for Numerical Methods in Engineering*. 1987;24(5):893-911.
- Soga K, Lee S, Ng M, Klar A. (2006). Characterisation and engineering properties of methane hydrate soils. *Characterisation and engineering properties of natural soils*;2591-2642.
- Sultan N, Garziglia S. (2011). Geomechanical constitutive modelling of gas-hydrate-bearing sediments. *The 7th International Conference on Gas Hydrates (ICGH 2011)*2011.
- Sun, R., and Duan, Z. (2007). An accurate model to predict the thermodynamic stability of methane hydrate and methane solubility in marine environments. *Chemical geology*, 244(1-2), 248-262.
- Tsympkin, G. G. (2000). Mathematical models of gas hydrates dissociation in porous media. *Annals of the New York Academy of Sciences*, 912(1), 428-436.
- Uchida S, Soga K, Yamamoto K. (2012). Critical state soil constitutive model for methane hydrate soil. *Journal of Geophysical Research: Solid Earth (1978–2012)*;117(B3).
- Uchida S, Xie XG, Leung YF. (2016). Role of critical state framework in understanding geomechanical behavior of methane hydrate - bearing sediments. *Journal of Geophysical Research: Solid Earth*.
- Ullerich, J., Selim, M., and Sloan, E. (1987). "Theory and measurement of hydrate dissociation." *AICHE Journal*, 33(5), 747-752.
- van Genuchten R. (1978). "Calculating the unsaturated hydraulic permeability conductivity with a new closed-form analytical model". *Water Resource Researc*, 37(11): 21-28
- Vaunat J, Gens A. (2003). Bond degradation and irreversible strains in soft argillaceous rock. *Proceedings of the 12<sup>th</sup> Panamerican conference on soil mechanics and geotechnical engineering*.
- Waite WF, Santamarina JC, Cortes DD, Dugan B, Espinoza D, Germaine J, et al. (2009). Physical properties of hydrate - bearing sediments. *Reviews of Geophysics*;47(4).
- Walsh, M. R., Hancock, S. H., Wilson, S. J., Patil, S. L., Moridis, G. J., Boswell, R., Collett, T. S., Koh, C. A., and Sloan, E. D. (2009). Preliminary report on the commercial viability of gas production from natural gas hydrates. *Energy Economics*, 31(5), 815-823.
- Wagner W., Kretzschmar, H. (2008) Int. Steam Tables, 2<sup>nd</sup> Ed, Springer Verlag, Berlin, Heidelberg, 2008
- Yamamoto, K., and Dallimore, S. (2008). Aurora-JOGMEC-NRCan Mallik 2006-2008 gas hydrate research project progress. *Natural Gas & Oil*, 304, 285-4541.
- Yoneda J, Masui A, Konno Y, Jin Y, Egawa K, Kida M, et al. (2015). Mechanical properties of hydrate-bearing turbidite reservoir in the first gas production test site of the Eastern Nankai Trough. *Marine and Petroleum Geology*. 2015;66:471-486
- Younglove B., and Ely J. (1987). Thermophysical Properties of Fluids II Methane, Ethane, Propane, Isobutane, and Normal Butane. *Journal of Physical and Chemical Reference Data* 16 (4): 577
- Yu, Y., Cheng, Y. P., Xu, X., & Soga, K. (2016). Discrete element modelling of methane hydrate soil sediments using elongated soil particles. *Computers and Geotechnics*.
- Yun T, Francisca F, Santamarina J, Ruppel C. (2005). Compressional and shear wave velocities in uncemented sediment containing gas hydrate. *Geophysical Research Letters*;32(10).
- Yun, T. S., Fratta, D., Santamarina, J. C. (2010). Hydrate-Bearing Sediments from the Krishna– Godavari Basin: Physical Characterization, PCT, and Scaled Production Monitoring. *Energy & Fuels*.
- Yun TS, Narsilio GA, Santamarina JC. (2006). Physical characterization of core samples recovered from Gulf of Mexico. *Marine and Petroleum Geology*;23(9):893-900.
- Yun, T. S., Santamarina, J. C., & Ruppel, C. (2007). Mechanical properties of sand, silt, and clay containing tetrahydrofuran hydrate. *Jnl. of Geophysical Research: Solid Earth (1978–2012)*, 112(B4).
- Zhang, X.-H., Lu, X.-B., Zhang, L.-M., Wang, S.-Y., & Li, Q.-P. (2012). Experimental study on mechanical properties of methane-hydrate-bearing sediments. *Acta Mechanica Sinica*, 28(5): 1356-1366.

## National Energy Technology Laboratory

626 Cochrans Mill Road  
P.O. Box 10940  
Pittsburgh, PA 15236-0940

3610 Collins Ferry Road  
P.O. Box 880  
Morgantown, WV 26507-0880

13131 Dairy Ashford Road, Suite 225  
Sugar Land, TX 77478

1450 Queen Avenue SW  
Albany, OR 97321-2198

Arctic Energy Office  
420 L Street, Suite 305  
Anchorage, AK 99501

Visit the NETL website at:  
[www.netl.doe.gov](http://www.netl.doe.gov)

Customer Service Line:  
1-800-553-7681



U.S. DEPARTMENT OF  
**ENERGY**

**NATIONAL ENERGY  
TECHNOLOGY LABORATORY**